atmosphere

MDPI

Review

A Tutorial Review of Cyclotron Resonance Interactions Between Magnetospheric Energetic Electrons and Electromagnetic Waves (Whistlers, Hiss, Chorus and VLF Transmitter Signals) Causing Electron Precipitation and Perturbations to the Upper Atmosphere

Michael J. Rycroft

Cambridge Atmospheric, Environmental and Space Activities and Research (CAESAR) Consultancy, 35 Millington Road, Cambridge CB3 9HW, UK; michaelrycroft@btinternet.com

Abstract

The concept of cyclotron resonance near the equatorial plane of the Earth's magnetosphere between whistlers and energetic electrons originated in the 1960s. Since then, the subject has advanced substantially, with experimental, theoretical and computer modelling studies. A chronological review is undertaken not only of the basic physics of gyro resonance but also of very-low-frequency (VLF) radio observations made on the ground and measurements made by various rocket and satellite instruments of the fluxes of precipitating energetic electrons and whistler-mode waves. Lightning-induced electron precipitation (LEP) contributes appreciably to the dynamics (i.e., the acceleration, transport and loss) of trapped Van Allen radiation belt electrons. However, plasmaspheric hiss (at $L < 4.5$, for quiet to moderate activity conditions) and chorus (generally at $L > 4.5$, beyond or outside the plasmasphere and often associated with auroral phenomena) are believed to be more important overall than LEP in causing the precipitation of energetic electrons from the magnetosphere at $L > 3.8$. The gyro resonant interaction between the VLF radio transmitter signals near the equatorial plane and energetic electrons also contributes appreciably to their loss. With LEP being the major cause, each plays a role in the formation of the slot in the radiation belts at $L \sim 2.5$. The mechanisms whereby precipitating energetic electrons perturb the physics and chemistry of the mesosphere and D-region ionosphere are also briefly reviewed.

Keywords: wave-particle interactions; whistler-mode waves; lightning-induced electron precipitation; hiss; chorus; VLF radio transmitters; slot in radiation belts; plasmapause; geomagnetic field; changes to upper atmosphere

Academic Editor: Masashi Hayakawa

Received: 4 August 2026
Revised: 19 October 2026
Accepted: 23 October 2026
Published: 3 November 2026

Copyright: © 2026 by the author. Licensee MDPI, Basel, Switzerland. This article is an open access article distributed under the terms and conditions of the Creative Commons Attribution (CC BY) license.

1. Introduction

This fascinating topic was initiated by Dungey [1], Cornwall [2], Brice [3] and Liemohn [4], who considered the energetics of the interaction between a whistler-mode wave and energetic electrons trapped in the Earth's magnetosphere. Lightning-generated whistlers are VLF (3 to 30 kHz) radio waves radiated by a lightning discharge that have propagated up through the ionosphere and into the magnetosphere. Whistlers are right-

hand circularly polarised extraordinary-mode (X-mode) radio waves propagating through a plasma, a charged particle gas. In the geomagnetic field, energetic electrons (>100 keV) exhibit three motions: (a) gyrating about the magnetic field line (time scale ~ ms), bouncing from one hemisphere to the other (time scale ~ s), and drifting in longitude (time scale ~ hours). There is an adiabatic invariant of motion associated with each type of motion; the first adiabatic invariant of motion is broken in wave–particle interactions. Dungey [1] showed that in such a whistler wave–electron interaction, the electron's pitch angle, i.e., the angle between the electron's velocity vector and the geomagnetic field vector, α, is reduced. This lowers the bouncing electron's mirror point and can put it into the loss cone so that it precipitates into the upper atmosphere. For this Doppler-shifted cyclotron interaction between whistlers and energetic electrons moving in the opposite direction, Tsurutani and Lakhina [5] thoroughly reviewed the basic concepts, showing that the fundamental (n = 1) cyclotron (or gyro) resonance condition is given by

$$\omega - \mathbf{k}.\mathbf{v} = n\,\omega_{B,e} \quad (1)$$

where ω is the angular wave frequency, **k** is the wave vector, **v** is the electron velocity, $\omega_{B,e}$ is the angular electron cyclotron frequency (or gyro frequency) eB/m_e, e is the electron charge and m_e is the electron mass, and n is an integer. For n = 1, this can be rearranged as

$$\omega - \omega_{B,e} = \mathbf{k}.\mathbf{v} \quad (2)$$

Since $\omega_{B,e}$ is >> ω, the left-hand side of this equation is a negative number which indicates that **k** and **v** are in opposite directions, i.e., the whistler-mode wave and the gyro resonant electrons are counter-streaming.

For relativistic electrons (>0.5 MeV), the right-hand side of Equation (1) has to be divided by γ, the Lorentz factor, $1/(1 - v^2/c^2)^{1/2}$, with c being the velocity of light (Tsurutani et al. [6]).

The n = 0 resonance is termed the Landau resonance. This occurs when an electron travels at the phase velocity of an electrostatic wave in a plasma, $v_\varphi = \omega/k$.

For the n = 1 resonance, Brice [3] showed that, when the whistler wave energy increases, the electron energy W decreases, with its longitudinal energy $W_\parallel$ increasing and its transverse energy $W_\perp$ decreasing. Therefore, its pitch angle α decreases so that it may be precipitated into the upper atmosphere and lost from the magnetospheric population. For frequencies much less than $\omega_{B,e}$, "a relatively small change in the energy of a whistler may cause a large change of energy from the longitudinal to the transverse energy of the particles and hence significant changes in the pitch angles of the particles" [3].

The angle between **k** and **B** is known as the wave normal angle. The phase velocity of the whistler-mode wave is $v_\varphi = c/\mu = \omega/k$, where the refractive index μ(N,B) is a function of the plasma density N and geomagnetic field strength B, given by the Appleton–Hartree equation for a cold plasma. The group velocity of a whistler-mode wave, $d\omega/dk$, is locally proportional to $(\omega\,\omega_{B,e}/N)^{1/2}$, where N is the electron density of the plasma.

Whistlers for which $\omega < 0.5\,\omega_{B,e}$ propagate along geomagnetic field-aligned ducts of enhanced plasma density N, which act like optical fibres, from one hemisphere to the other; L-values specify geomagnetic field lines. Whistler-mode waves may also propagate unducted, or non-ducted, through the magnetospheric plasma. In both cases, the dispersed whistler signal is an audio frequency tone of falling frequency, f(t), where t is the propagation time (~a few s) and $f = \omega/2\pi$. When analysing whistler-mode waves, the error in measuring the frequency, or the analysis bandwidth, Δf, is related to the imprecision in knowing the time when the wave has that frequency, Δt, by the relation $\Delta f.\Delta t \sim 1$.

Kennel and Petschek [7] discussed the plasma physics of this gyro resonant situation involving the distribution function of electrons in terms of their velocity, f(v). The

instability generating these waves in the magnetosphere, the "loss cone instability", happens when the electron distribution function is anisotropic, i.e., when the energetic electron temperature (or energy, $W_{\parallel}$) parallel to the geomagnetic field exceeds the energetic electron temperature (or energy, $W_{\perp}$) perpendicular to the field. They showed [7] that whistler-mode noise leads to the diffusion of trapped energetic electrons in pitch angle. This diffusion results in energetic electron precipitation into the ionosphere and creates a pitch angle distribution of trapped >40 keV electrons that is unstable to further wave growth via a transverse (cyclotron resonance) plasma instability.

Here I discuss the ideas and results presented in significant papers on the physics of cyclotron resonance wave–particle interactions, both experimental and theoretical, on different topics and in chronological order, so that the reader can gain an appreciation of how the subject has developed in the last 63 years. That is the rationale for this paper. The conclusions of the paper are expressed as 24 numbered points, together with two tables which summarise the main wave–particle interactions and consequent energetic electron precipitation events into the upper atmosphere for different L-shell ranges.

2. First Observation and Interpretation of a Whistler–Energetic Electron Interaction

The first experimental result in this subject area, a serendipitous one, was obtained by Rycroft [8]. During the flight of a Petrel rocket, instrumented by the SRC Radio and Space Research Station with Geiger counters and launched westwards from South Uist, Outer Hebrides, Scotland (L = 3.38), a transient increase was observed in the intensity of energetic electrons with pitch angles between 60° and 120°. Most of these magnetospheric electrons were therefore precipitating into the atmosphere. The sudden intensity increase, by a factor of 20 above the quasi-steady intensity observed throughout the remainder of the flight, occurred in 0.8 s and was simultaneous for both > 45 keV and > 110 keV electrons. Recorded on the ground, ~0.5 s later, was a two-hop whistler, originating from a lightning discharge in the northern hemisphere. During the enhanced electron intensity event, the entire duration of which was ~7 s, four-, six- and eight-hop whistlers were also received; Figure 1 shows this event. From an analysis of the two-hop whistler's spectrogram, it was deduced that the whistlers were ducted through the magnetosphere along the $L = 3.3 \pm 0.1$ field line. Theoretical considerations [8] led to the electron density in the equatorial plane being found to be 330 ± 10 cm^{-3}, a value characteristic of conditions within the plasmapause.

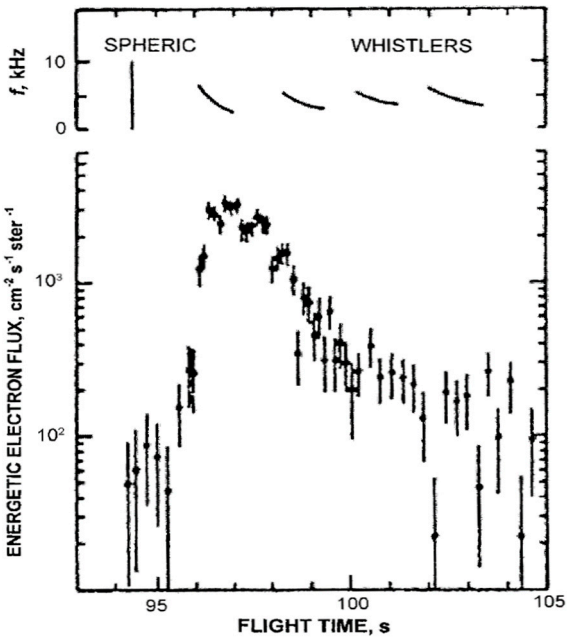


Figure 1. The spectrogram of multi-hop whistlers recorded on the ground on South Uist and the flux of >45 keV electrons observed aboard a rocket at an altitude of ~100 km over a 12 s time interval at 22.42:30 UT on 30 September 1969, when the Kp index was 3- [8]. The time of the lightning discharge causing this whistler is shown by the atmospheric (shortened to spheric, or sferic). The most energetic electrons arrived 1.0 s after this; then, in 0.8 s, the energetic electron flux increased rapidly to a peak lasting ~1 s, and then fell to the background level over the next ~5 s. The maximum flux of electrons (>45 keV) was 3.10^3 $cm^{-2}s^{-1}sr^{-1}$ [8].

It was proposed [8] that these temporally and spatially associated phenomena, rather than arising by chance, were the result of an n = 1 gyro resonant interaction between energetic electrons and ducted whistler-mode waves moving in opposite directions through the magnetosphere, as illustrated in Figure 2. For gyro resonance on an $L = 3.3 \pm 0.1$ field line at the equator, where the plasma density was shown to be ~330 ± 10 cm^{-3}, within the plasmasphere, the parallel component of energy of the electrons, $W_{\parallel}$, was found to be 25 keV at 3 kHz in the whistler band, or 100 keV at 1 kHz below it. It was suggested that a magnetospheric event occurred, causing both sudden enhanced electron precipitation and favourable conditions for the propagation and/or amplification of whistlers. A possible explanation is that energetic electrons, having a sufficiently anisotropic distribution function and being associated with those injected during an earlier auroral substorm, became unstable via the transverse resonance instability when they drifted into the plasmasphere. Rycroft [8] also noted that the energetic electron flux exhibited fine structure with a periodicity of ~0.6 ± 0.1 s that could be ascribed to the bouncing of a bunch of energetic electrons from the northern hemisphere to the geomagnetic conjugate region and back again. For an equatorial pitch angle of ~7°, at L = 3.3, the bounce period for 100 keV electrons is 0.6 s.

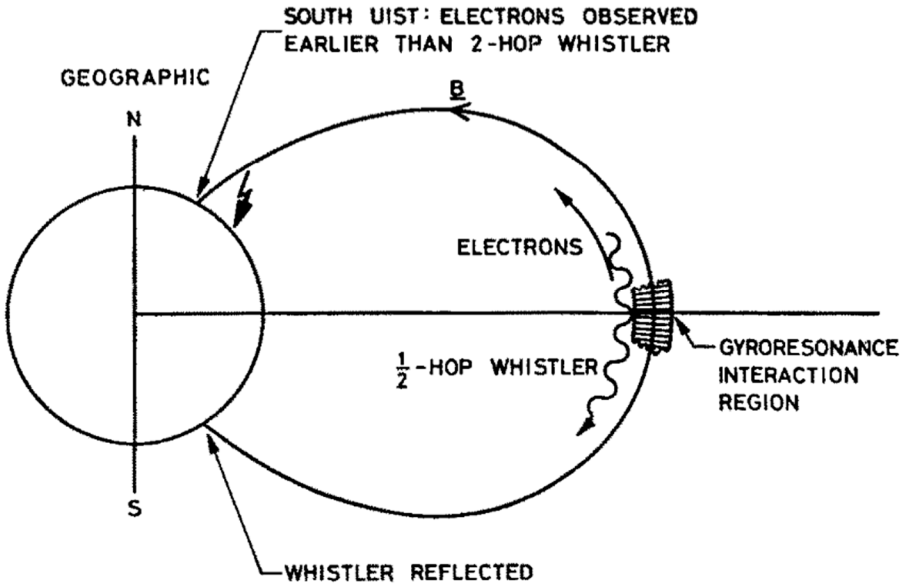


Figure 2. Diagram of the gyro resonant interaction near the equatorial plane of the magnetosphere (L ~ 3.3) between a southward-propagating half-hop whistler and northward-moving >45 keV electrons [8]. This mechanism causes lightning-induced electron precipitation (LEP), in this case into the northern hemisphere.

For the n = 1 gyro resonance between whistler-mode waves and counter-streaming energetic electrons, the first adiabatic invariant of motion of the (non-relativistic) energetic electrons, the magnetic moment, $\mu_B = W_\perp/B$, where $W_\perp$ is the energetic electron energy perpendicular to the geomagnetic field, is broken. Rycroft [9] focused attention on this wave–particle interaction in the equatorial plane of the magnetosphere. The component of the energy of non-relativistic n = 1 gyro resonant electrons parallel to the geomagnetic field, $W_\parallel$, is calculated in the equatorial plane, using Equation (2) (also see [9]).

The refractive index of the plasma, μ, for the longitudinal propagation of whistler-mode waves depends on the plasma density N and the geomagnetic field strength B. In the equatorial plane, where $N = N_{eq}$ and $B = B_{eq}$, μ is given by

$$\mu^2 = (N_{eq}e^2/\varepsilon_0 m_e)/\omega(\omega_{B,e\ eq} - \omega) \quad (3)$$

With ε_0 being the permittivity of free space. μ is largest in the equatorial plane where, on a particular L-shell, $\omega_{B,e\,eq}$ is smallest. For a whistler with $\omega < \omega_{B,e\,eq}$ and for typical values of the parameters at L ~ 3 at the equator, μ_{eq} ~ 10.

Furthermore, inserting Equation (3) into the square of Equation (2), and rearranging, it is evident that

$$W_\parallel N_{eq} = \{B_{eq}^2/2\mu_0\}.\{f_{B,e\,eq}/f\,(1 - f/f_{B,e\,eq})^3\} \quad (4)$$

where N_{eq} is plasma density at the equator on a particular dipolar geomagnetic field line specified by its L-value, μ_0 is the permeability of free space, f is the resonant wave frequency and $f_{B,e\ eq}$ is the electron gyro frequency at the equator for this L-shell [9]. Numerically, with $W_\parallel$ in keV, N_{eq} in cm^{-3} and frequencies in kHz,

$$W_\parallel N_{eq} = 3.16\ (f_{B,e\ eq} - f)^3/f\ \text{keV cm}^{-3} \quad (5)$$

Rycroft [9] presented a graph of the product of $W_\parallel$ and N_{eq} against L for different frequencies. For L = 3.3 at 3 kHz, in the whistler band, with the whistler being amplified [3], $W_\parallel$ = 25 keV and, at 1 kHz, a frequency less than that observed in the whistler, $W_\parallel$ = 100 keV [8]. For precipitating electrons, most of their energy is longitudinal, $W_\parallel$, not

transverse to the geomagnetic field, $W_{\perp}$. The pitch angles of the gyro resonant electrons are reduced so that these energetic electrons are precipitated out of the radiation belts [1,3].

The same information as given in [9] can be more conveniently shown as a plot of $W_{\parallel}N_{eq}$ against f for different L-values between L = 3 and 6 (see Figure 1 in [10]). As L increases, and hence as the equatorial electron gyrofrequency decreases, the interaction tends to occur at lower frequencies and at a lower value of $W_{\parallel}N_{eq}$. On a particular L-value, for interaction in the equatorial plane at a certain value of N_{eq}, $W_{\parallel}$ is higher at the lower frequencies. This is important in relation to the generation of chorus (Section 6); the anisotropy of the electron distribution function was also investigated in [7,10]. Useful graphs showing the variation of $W_{\parallel}$ with f for different L-values for a typical modelled profile of the equatorial plane plasma density, N_{eq}, within the plasmasphere and across the plasmapause at L = 4 were also presented (see Figure 3 in [10]). For example, at L = 3, with N_{eq} equal to ~ 700 cm^{-3}, at 0.3 kHz $W_{\parallel}$ is ~ 600 keV, at 1 kHz it is ~ 200 keV, at 3 kHz ~ 60 keV, and at 10 kHz ~ 6 keV; log $W_{\parallel}$ is almost inversely linearly related to log f. At L = 5, at 0.1 kHz $W_{\parallel}$ is ~ 300 keV, at 0.3 kHz ~ 100 keV, at 1 kHz ~ 30 keV, and 3 kHz only ~3 keV [10].

3. Stanford University Research up to 1986

Helliwell et al. [11] showed that sudden changes in the amplitude of long-distance sub-ionospheric VLF transmissions found at night were associated with whistlers. Both increases and decreases in signal strength were observed. Observations made at Eights Station, Antarctica, of station NSS (Annapolis, Maryland, used for communicating with submarines) on 22.3 kHz showed increases in signal strength of ~3 dB, with rise times of ~2 s and durations of ~30 s. Coincident with every rise was a midlatitude (L ~ 2.5) whistler originating in the northern hemisphere. To explain this association, they suggested that the whistler precipitates energetic (30–300 keV) electrons into the D region. The mechanism of precipitation was thought to be the pitch angle scattering of trapped electrons that resonate with the whistler wave near the magnetic equator [9]. The resulting enhancement in D-region ionisation alters the properties of the Earth–ionosphere waveguide. This effect was named the Trimpi effect after its discoverer [11]; such changes of VLF propagation parameters are termed Trimpis.

Carpenter and LaBelle [12] reported further on the Trimpi effect, which involves the observation of amplitude perturbations in sub-ionospherically propagating VLF transmitter signals. The perturbations which coincided in time with whistlers propagating through the plasmasphere were interpreted as the whistlers causing energetic electron (>100 keV) precipitation, resulting in a localised increase in ionisation near 80 km altitude in the nighttime Earth–ionosphere waveguide. VLF broadband and direction-finding data from Palmer Station, Antarctica (L ~ 2.3), were used to investigate additional features of the Trimpi process. Attention was concentrated on 10–30% amplitude perturbations of the signals NSS (21.4 kHz) and NLK (18.6 kHz); a large equinoctial peak in activity was found. It was concluded that the southern hemisphere region within which perturbations occurred was within a few hundred km of Palmer Station.

Doolittle and Carpenter [13] reported the first observations of 4278 Å optical emissions made near Roberval, Quebec, Canada, which is the geomagnetic conjugate of Siple Station, Antarctica. Associated with two-hop whistler-mode waves, but ~0.7 s ahead of these, the optical emissions were interpreted as being caused by energetic electron precipitation due to the first-order cyclotron resonance interaction [8].

Vampola [14] reported that spikes in electron precipitation, in which the energy spread of the peak is narrow (less than 50 keV) and the peak energy is a strong function of the location in L, were observed in the region 1.5 < L < 2.0 and ascribed to interactions between waves from high-power VLF transmitters on the ground and energetic electrons

[14]. "On numerous occasions when these spikes were observed at low altitude by instrumentation on the S3-2 satellite, a significant depletion of electrons at the same energies was observed high on the field line. These depletions indicated that the loss rate of electrons due to VLF transmitters is significant and usually exceeds the rate at which the radial diffusion of electrons is refilling those field lines. Electrons with energies between 36 keV and 317 keV at $1.6 < L < 1.9$ were observed to have lifetimes limited to a few days by interactions with waves from VLF transmitters. The outer edge of the inner zone is defined by this wave-particle process" [14].

Radiation belt electron precipitation by the controlled injection of VLF signals from a ground-based transmitter was directly observed on satellites for the first time by Imhof et al. [15]. These observations were part of the SEEP (Stimulated Emission of Energetic Particles) experiment conducted in 1982. An outstanding example of time-correlated wave and particle data occurred on 17 August 1982, when the satellite passed nearly above NAA. During each of twelve consecutive pulses from the transmitter, the electron counting rate increased significantly after the start of the "on" period and reached a maximum about 2 s later. The measured energy spectra revealed that approximately 15–50% of the enhanced electron flux was concentrated near the resonant energies for first-order cyclotron resonance interactions occurring close to the magnetic equator with the nearly monochromatic waves emitted by the transmitter.

Voss et al. [16] reported the first measurements made aboard the Stimulated Emission of Energetic Particles (SEEP) satellite (at about 230 km altitude) of lightning-induced electron precipitation (LEP) at $2.1 < L < 2.4$, using data from solid-state electron detectors of > 45 keV and > 100 keV electrons. The electron bursts were ~ 100 times greater than the background levels. The electron precipitation energy fluxes were estimated to be about 10^2 to 10^5 times the whistler energy flux in the equatorial plane. This indicates that only a small amount of wave energy is needed to perturb the electrons near the edge of the loss cone enough to cause their precipitation. The energy deposition associated with such LEP bursts was found to be ~10^{-3} erg cm^{-2} [14]. In a Nature News and Views item, Rycroft [17] emphasised that, for cyclotron resonance in the equatorial plane of the $L = 2.2 \pm 0.1$ flux tube, the electron density is estimated to be 3200 cm^{-3}; waves with a frequency of 4 kHz resonate with 150 keV electrons. Such energetic electrons can penetrate the atmosphere down to a height of 80 km, where they cause a significant amount of secondary ionisation (see Section 12). This can affect the amplitude and phase characteristics of VLF radio waves propagating in the Earth–ionosphere waveguide.

Carpenter et al. [18] reported the first evidence of a correlation between whistlers and amplitude perturbations on low-frequency (LF) signals at 37.2 kHz and medium-frequency (MF) signals at 780 kHz. Whistler-correlated amplitude perturbations were observed on the MF signal propagating on an approximately 1800 km path from South America to Palmer Station, Antarctica. The observed MF perturbations were of the order of 50% in amplitude and developed much more quickly than other changes of comparable magnitude on the signal. Inan et al. [19] reported new evidence of phase perturbations of sub-ionospheric VLF/LF radio signals, produced by lightning (whistler)-induced precipitation of bursts of radiation belt electrons. Phase changes of up to 1 μs on a 12.9 kHz signal arriving at Palmer ($L \sim 2.4$) over a ~2400 km path were regularly observed. The occurrence of these events reached a maximum during equinoctial periods, with typical rates of 1 to 40 events at nighttime. The observed phase perturbations can be interpreted as a rapid reduction by up to 1 km in the ionospheric reflection height (~85 km) for the sub-ionospheric VLF signals. The fluxes of energetic electrons required to produce the extra ionisation were estimated to be ~10^{-3} to 10^{-2} erg cm^{-2} s^{-1}. Such flux levels are generally consistent with those estimated using theoretical models of whistler–

electron resonant scattering, as well as with direct satellite-based observations of whistler-induced precipitation [19].

Chang and Inan [20] considered the precipitation of radiation belt particles induced by whistlers that are generated by atmospheric lightning discharges and propagate at 2.0 < L < 4.5. "Using a test particle model of the whistler-particle interaction, the energy spectra and temporal profile of whistler-induced fluxes as a function of *L*-shell were quantitatively determined for a representative plasmaspheric cold plasma distribution. Their results indicated that for higher energy electron precipitation (>40 keV) there exists an inner magnetospheric region (2 < *L* < 3) where the level of whistler-induced precipitation can be expected to be comparatively high".

Imhof et al. [21] discussed the precipitation of energetic electrons from the slot region between the inner and outer Van Allen radiation belts (L ~ 2.5) by a variety of mechanisms, including short-duration (~few s) wave bursts associated with lightning or chorus and with more slowly varying plasmaspheric hiss (see Section 5). Chorus, which sounds like birds chirping at dawn, consists of rapidly rising audio frequency tones lasting a fraction of a second (see Section 6), whereas hiss is a broadband signal, unstructured in the frequency–time domain. The characteristics of the night-side short-duration precipitation events, including their favoured occurrence at certain longitudes in the northern hemisphere, indicated that they were predominantly associated with lightning, whereas the dayside events seemed to be related primarily to VLF chorus.

The total rates of loss of electrons from the radiation belts were obtained from the measured energy spectra and pitch angle distributions [21]. The slowly varying electron fluxes observed in the drift loss cone frequently displayed peaks in the energy spectra, indicating that they are precipitated by plasmaspheric hiss and that this process therefore represents a major loss mechanism. "Well-defined bursts, which appear to be associated with lightning at nighttime and perhaps chorus in the daytime, were observed on only about 2% of the satellite passes, suggesting that such bursts are not the dominant loss mechanism" [21].

4. Research on LEP Around the World in the Last Forty Years

Goldberg et al. [22] reported electron precipitation bursts stimulated by observed lightning flashes using rocket techniques under nighttime conditions at Wallops Island, Virginia, in August 1984. In one case, the rocket-observed lightning flash was geolocated by a ground-based network to be off the coast of Virginia, approximately 200 km southeast of the rocket. Electron precipitation (>40 keV) caused by simultaneous 21.4 kHz coded transmissions from a VLF radio transmitter at Annapolis, Maryland, was found to be negligible compared with the observed fluxes and energies of precipitating electrons stimulated by lightning.

Inan et al. [23] investigated the characteristics of lightning-induced electron precipitation (LEP) events at longitudes of the western (110° W) versus eastern (70° W) United States considered from the point of view of the available trapped electron flux at the edge of the loss cone. Using published data on nighttime fluxes of >68 keV electrons observed at L ~ 2.5, and for "direct" precipitation into the northern hemisphere induced by northern hemisphere lightning, the occurrence rate and flux levels were expected to be 20 to 200 times higher in the west than in the east, assuming that there was no significant variation in lightning source activity with longitude. For lightning sources in the north, it was predicted that, at 70° W, "mirrored" precipitation into the southern hemisphere would involve precipitation fluxes 30 to 300 times higher than "direct" precipitation into the northern hemisphere.

Rycroft [24] reviewed "the physical mechanism of a cyclotron resonance interaction between trapped energetic electrons and whistler-mode waves in the magnetosphere. Not

only do the electrons have their pitch angles reduced in this interaction so that they may be precipitated into the upper atmosphere, but also the waves can be amplified. Such a flux of precipitating electrons can, either by direct ionisation or via bremsstrahlung radiation, cause a pimple to be produced on the bottom of the ionosphere (~85 km altitude). That can significantly modify the amplitude and/or phase of VLF radio signals propagating in the Earth–ionosphere waveguide. Various experimental observations that demonstrate the reality of such effects were reviewed".

Dowden et al. [25] discussed lightning-induced ionisation enhancements (LIEs) produced by short (~1 s) bursts of energetic electrons precipitated from the radiation belts in the process of amplifying whistlers. During their short life (~30 s), LIEs diffract or otherwise modify stable transmissions of VLF waves propagating in the two-dimensional Earth–ionosphere waveguide. This causes perturbations (Trimpis) on the same time scale in the phase and amplitude of these transmitted VLF waves.

Arguably the most significant source of charged particle precipitation into the ionosphere at mid-latitudes (L ~ 2 to 3), at least for electrons in an energy range of up to several hundred keV, is that which arises from the interaction between trapped electrons and whistler-mode waves in the magnetosphere [26]. Quasi-steady plasmaspheric hiss has long been postulated as contributing to the loss of radiation belt particles, but impulsive precipitation caused by interactions with lightning-generated whistlers [8] may be equally important. Such lightning-induced electron precipitation and its ionospheric signature were the subject of this paper by Smith [26]. "Although LEP may be detected and studied by a variety of ground-based, balloon-borne and satellite-borne sensors, through optical emissions, X-ray production, enhanced ionospheric conductivity, or the direct measurement of the precipitating electrons themselves, a technique using ground-based narrow-band VLF receivers to measure the Trimpi effect (the transient perturbations in amplitude and/or phase of received narrow-band VLF transmissions) caused by LEP-associated ionisation enhancements has become increasingly popular due to its simple instrumentation and wide field of view. Most work has been concentrated on the $2 < L < 3$ region where typical whistler spectra, trapped electron energy distributions and magnetospheric plasma densities and magnetic field strengths are most favourable for the Trimpi effect. To use the technique to study in detail the characteristics and distribution of LEP (and its importance as a trapped-particle loss mechanism), using a network of intersecting transmitter-receiver great-circle paths (TRGCPs), a consensus on how to interpret the observational data is crucial. Whilst most studies suggest that only LEP within ~200 km of the TRGCP gives rise to an observable Trimpi event, some authors have suggested that perturbations well off the TRGCP can be important. The current state of LEP research was summarised and some recent results presented using data from a network of both widely and closely spaced observing sites in Antarctica" [26].

Voss et al. [27] investigated lightning-induced electron precipitation using SEEP satellite observations. LEP events were correlated on a one-to-one basis with one-hop whistlers observed at Palmer Station, Antarctica. The temporal profile within a LEP burst was shown to be associated with bunches of magnetically guided and focused 100–200 keV electrons that were repeatedly scattered by the atmosphere and bounced between the northern and southern hemispheres. The delay time between the lightning sferic and the arrival of the first electron bunch increased with increasing L value, as predicted by the first-order gyro resonance theory [8]. The global distribution of strong LEP events correlated with lightning activity and showed a preferred distribution at $2 < L < 3$, the slot region in the electron radiation belt. A single LEP burst (of ~10^{-3} erg s^{-1} cm^{-2}) was estimated to deplete only ~0.001% of the energetic electrons by a ducted (rather than non-ducted) whistler [27]. It was concluded that ducted whistlers can be an important pitch angle diffusion mechanism for 100–250 keV electrons at $2 < L < 3$.

Using SAMPEX data at ~600 km altitude, Blake et al. [28] revealed enhanced energetic (>150 keV) electron fluxes at L < 3 when the satellite was located such that any eastward drifting electrons that were observed were in the drift loss cone; they were destined to be precipitated when they reached the longitude of the South Atlantic Geomagnetic Anomaly. Data from the UARS satellite, passing through the same region within the same hour, confirmed the presence of L-dependent structures. The electron energy spectra and the spectral characteristics of lightning-induced electron precipitation events in the bounce loss cone were found to be similar [28]. This similarity lends support to the argument that the observed drift loss cone features are produced by the LEP process. It was concluded that globally distributed thunderstorms may continually precipitate energetic electrons from the radiation belts, producing transient enhancements in the drift loss cone that can be detected as they drift around the Earth and precipitate into the upper atmosphere in the South Atlantic Geomagnetic Anomaly.

Rodger and Clilverd [29] investigated whistler-induced electron precipitation (WEP), which determines inner belt electron lifetimes. Long-term WEP-driven losses at L = 2.23 were found to be more significant than all other inner radiation belt loss processes for electrons of 40–350 keV, suggesting a faster depletion rate and thus lower lifetimes than previously calculated. Thunderstorm-generated whistlers were shown to be an important factor in determining the lifetimes of medium-energy electrons in the inner belt. The modelling of Rodger et al. [30] suggested that long-term WEP-driven losses were more significant than all other inner radiation belt loss processes for electrons with energies between 50 and 150 keV at 2.0 < L < 2.4. The upper energy limit of the WEP process increases as L decreases, to ~225 keV at L = 2. For electron energies above this, manmade VLF transmitter signals (see Section 7) and plasmaspheric hiss (see Section 5) are believed to dominate over all other loss processes. Since these lifetimes were based on rather conservative parameter estimates, these values represent the lower bounds for the energy ranges over which WEP losses are significant. For lower L-shells, the coupling of lightning to the production of WEP events rapidly decreases, such that by L ~ 1.7, WEP is unimportant in the overall loss processes. These are very significant conclusions [30].

Clilverd et al. [31] considered the dependence of precipitation fluxes arising from whistler-induced radiation belt losses on the strength of the associated lightning's return stroke current. During these WEP events, pitch angle diffusion conditions occur near the precipitating radiation belt particles' loss cone due to the strong whistler wave fields, which are probably ducted signals. The range of observed Trimpi scatter amplitudes of -10 to -35 dB was produced by precipitation bursts with energy fluxes estimated to range from 0.4 to 6.5 10 erg cm^{-2} s^{-1}. These can produce a D-region electron density enhancement of up to ~ 1.5 10^{7} m^{-3}. Revised estimates of typical electron precipitation bursts at L ~ 2.3 to a mean precipitation energy flux of ~10^{-3} erg cm^{-2} s^{-1} were published by Rodger et al. [32]. The precipitation of energetic electrons by these bursts in the L-shell range 1.9 < L < 3.5 leads to a mean rate of energy deposited into the atmosphere of 3 10^{-4} ergcm^{-2} min^{-1}, spatially varying from essentially zero above some ocean regions to values of up to 6 10^{-3} erg cm^{-2} min^{-1} above the thunderstorms of North America and its geomagnetically conjugate region [32,33].

The occurrence rate of lightning-induced electron precipitation (LEP) events, as recorded on several VLF/LF transmitter signal propagation paths, was found by Peter and Chevalier [34] to be highly variable with geomagnetic activity. A comparison of LEP event occurrence rates with measurements of energetic electron flux levels from the NOAA-POES satellite supported the idea that this variability was due largely to geomagnetic storm-associated increases in the energetic electron population in the slot region. Following this up, Peter et al. [35] showed that quantitative modelling of sub-ionospheric VLF wave propagation incorporating energetic electron flux measurements (and the

associated altitude profiles of secondary ionisation) yielded results consistent with the variations in the VLF signal amplitude observed.

Ray tracing of whistlers and a first-order treatment of the wave frequency and electron energy dependence of gyro resonant pitch angle scattering [8] by Bortnik et al. [36] revealed the *L*-shell dependence of the time-integrated energetic electron (>150 keV) precipitation flux in the drift loss cone as being due to a single cloud-to-ground lightning stroke. The main features of the *L* dependence were determined by the ray paths of magnetospherically reflecting (MR) non-ducted whistler waves, as well as the refraction of the wave normal vectors due to ionospheric horizontal electron density gradients at low latitudes, which resulted in a spatially narrow precipitation signature at low *L*-shells ($1.4 < L < 1.65$). Subsequent magnetospheric reflections resulted in a broad precipitation peak at higher *L*-shells ($1.8 < L < 4.2$). The calculated *L* dependencies were found to be in excellent agreement with drift loss cone electron fluxes measured aboard the SAMPEX satellite. Bortnik et al. [37] showed significant MR whistler precipitation at $2 < L < 5$, with precipitating energy fluxes ranging from 10^{-5} to 10^{-2} erg $cm^{-2}s^{-1}$.

Using data from the French micro-satellite DEMETER, Inan et al. [38] studied short bursts of lightning-induced electron precipitation simultaneously with newly injected upgoing whistlers, and sometimes also with once-reflected (from the conjugate hemisphere) whistlers. The LEP bursts occurred within < 1 s of the causative lightning and consisted of 100–300 keV electrons; their flux was ~10^2 cm^{-2} s^{-1} sr^{-1} at L ~ 2 over central Europe (their Figure 3) [38]. The regions of enhanced precipitation were ~3° latitude by ~5° longitude in size, being produced and maintained by a high rate of lightning occurrence within a localised thunderstorm [38].

Considering that energetic electrons (>100 keV) in the Earth's radiation belts undergo Doppler-shifted cyclotron-resonant interactions with a variety of whistler-mode waves, leading to pitch angle scattering and their subsequent loss to the atmosphere, Meredith et al. [39] assessed the relative importance of plasmaspheric hiss and lightning-generated whistlers in the slot region. They found that plasmaspheric hiss was more important. During magnetically active periods, losses due to plasmaspheric hiss could occur on a time scale of a day or less for a wide range of energies, 200 keV < W < 1 MeV, in the region $3.5 < L < 4.0$.

Parrot et al. [40] found that the most intense whistlers recorded on DEMETER were caused by the strongest lightning discharges below the satellite, at night. These were generally associated with Transient Luminous Events such as sprites [41]. The electron density at the satellite was perturbed by up to 133%, which indicates the presence of a whistler duct that may be related to the energetic electron precipitation induced by strong whistlers emitted during long-duration thunderstorm activity. This confirms the work of Pasko et al. [42], who showed that the thunderstorm electromagnetic activity causing LEPs can locally change the conductivity of the lower ionosphere. This is likely to favour the conditions necessary to produce sprites. An increase in D-region ionisation can lead to a feedback mechanism and to the occurrence of even more sprites. It would be interesting not only to investigate experimentally whether LEPs can initiate sprite-producing lightning discharges, but also to perform a statistical study to see if sprite-generating lightning strokes produced more LEPs than comparable lightning strokes that do not cause sprites.

Using energetic electron data from DEMETER, Gemelos et al. [43] showed that "energetic electron precipitation exhibits a seasonal dependence consistent with lighting-induced electron precipitation (LEP). Over the USA, energetic electron fluxes in the slot region ($2 < L < 3$) were significantly higher in the northern summer than in the winter, consistent with the seasonal variation of lightning activity in the northern hemisphere. The association of precipitating fluxes with lightning was explored using lightning

location data from the National Lightning Detection Network (NLDN) and VLF wave data from DEMETER. The increased precipitation of electrons into the drift loss cone over the northern hemisphere in summer was shown to be consistent with the expected pitch angle scattering by lightning-generated whistler waves". With there being, on average, ~ 44 lightning flashes s^{-1} around the world [44], lightning is a significant contributor to the loss of energetic electrons in the slot region.

Rycroft [45] reviewed our "understanding of the Doppler-shifted cyclotron resonance interactions between ducted whistler-mode radio signals travelling in one direction along a dipolar geomagnetic flux tube (1.5 < L < ~6) and Van Allen radiation belt electrons travelling in the other direction. These signals ranged from natural whistlers generated by lightning discharges and sweeping in frequency to (apparently) spontaneously generated hiss and chorus, and to single frequency signals from ground-based VLF radio transmitters. In these interactions, whistler-mode waves of audio frequency grew in amplitude and the electrons' pitch angles were reduced, some being pushed into the loss cone to perturb the lower ionosphere at the foot of the flux tube where the interaction has taken place. The responsible plasma instability acts at or close to the equatorial plane of the magnetosphere. With feedback mechanisms, cyclotron maser action [46] takes place. In many cases, this action produces signals of rising frequency (and occasionally of nearly constant or falling frequency). Observations have been made of aspects of these interactions on rockets and on Earth-orbiting satellites, complemented by radio observations made on the ground. Such observations were reviewed for naturally occurring whistlers, chorus and man-made signals, e.g., from the Siple transmitter in Antarctica and the NWC transmitter in Australia. Self-consistent nonlinear theoretical analyses of these interactions, involving broad electron distribution functions, have been undertaken and numerical simulations performed".

Colman and Starks [47] used Optical Transient Detector/Lightning Imaging Sensor (OTD/LIS) lightning data from 1995 to 2005 to construct a climatology of lightning strokes with 1° latitude by 1° longitude spatial resolution, averaged into two hourly bins for each month of the year. Assuming a linear relationship between the optical flash rate and VLF power flux and considering that the VLF amplitude drops off as the reciprocal of distance, a proxy for VLF power was developed. Using a typical lightning spectrum, these values were mapped along geomagnetic field lines to compare them with electric field spectral densities measured by the DEMETER satellite. The electric field spectral densities were converted to Poynting flux, mapped into the plasmasphere, and converted to magnetic field spectral densities; typical values were 10^{-3} pT^2/Hz at ~4 kHz at 1.5 < L < 3 [47].

Agapitov et al. [48] published the statistics of the RMS amplitude distribution of hiss, lightning-generated whistlers, and other whistler-mode waves at 1.4 < L < 3.0 from 10 years of Akebono satellite data. While VLF waves probably propagated mainly in a ducted mode for Kp < 3, they seemed to become more non-ducted during disturbed periods (Kp > 3). Hiss waves (see Section 5) were generally the most intense in the inner electron belt, and lightning-generated whistlers as well as hiss became more intense with increasing geomagnetic activity, albeit less so at L > 2. Cyclotron resonance scattering by hiss (~1 kHz) waves of rms amplitude ~25 pT near the equatorial plane was found to prevail at 1.8 < L < 2 while lightning-generated waves (~1.3 to 7.5 kHz, ~4 pT) contributed significantly at 1.6 < L < 1.8. Ducted lightning-generated whistlers recorded during moderate geomagnetic activity account for the observed lifetimes of energetic electrons. They concluded that the acceleration of trapped electrons by whistlers could play a role in shaping the inner radiation belt (at L ~ 1.5) together with pitch angle scattering of electrons towards the loss cone [48].

Simultaneous burst-mode waveform data from the Van Allen Probes (Radiation Belt Storm Probes, RBSP) and global lightning data from the World Wide Lightning Location

Network (WWLLN) were analysed by Zheng et al. [49]. Data were obtained between July and September 2013 and between March and April 2014 on days when each of the two RBSP satellites was predicted to be magnetically conjugate to lightning-producing regions. The prediction method used WWLLN lightning stroke data for that day obtained during the three previous years. Whistlers were observed on the satellites in more than 80% of the data. About 23% of the whistlers observed by RBSP were one-to-one coincident with lightning strokes detected by WWLLN. About 40% more of the whistlers were found to be one-to-one coincident with lightning if source regions were extended out 2000 km from the satellites' foot points. Lightning strokes with far-field radiated VLF energy larger than about 100 J generated a detectable whistler wave. One-to-one coincidences between whistlers observed by RBSP and lightning strokes detected by WWLLN were clearly shown at $1 < L < 3$ [49].

Green et al. [50] considered that lightning-generated whistlers (LGWs) play an important role in precipitating energetic electrons in the Earth's inner radiation belt and beyond. They used wave burst data from the Van Allen Probes to unambiguously identify LGWs ($0.3 < f < 10$ kHz) and analyse their properties at $1 < L < 4$. Their wave amplitudes were typically found to be strong, up to some tens of pT, at $L < 3$ on the nightside. Their lifetime calculations indicated that both ducted and non-ducted LGWs play an important role in scattering electrons from tens of keV to several MeV at $L < 2.5$ [50].

A different topic was introduced by Xu et al. [51], namely chemical changes produced in the stratosphere and mesosphere by LEPs. They combined a well-validated LEP model and a first-principles atmospheric chemical simulation to investigate the effects of intense geomagnetic storms to show that LEP events can drive significant changes in the ozone concentration in the mesosphere, at 75 to 85 km altitude, through the catalytic cycles of odd nitrogen ($[NO_x] = [N] + [NO] + [NO_2]$) and odd hydrogen ($[HO_x] = [H] + [OH] + [HO_2]$). They concluded that, considering the high occurrence rate of thunderstorms around the globe, the long-term global chemical effects produced by LEP events need to be properly quantified [46]. This issue is covered in Section 12. Figure 3, from [51], shows the modelled electron density profiles at altitudes from 60 to 120 km produced by LEP electrons at different times during the 10 s of a typical LEP event at L = 2. Also shown is the mean LEP ionisation production profile of Rodger et al. [52].

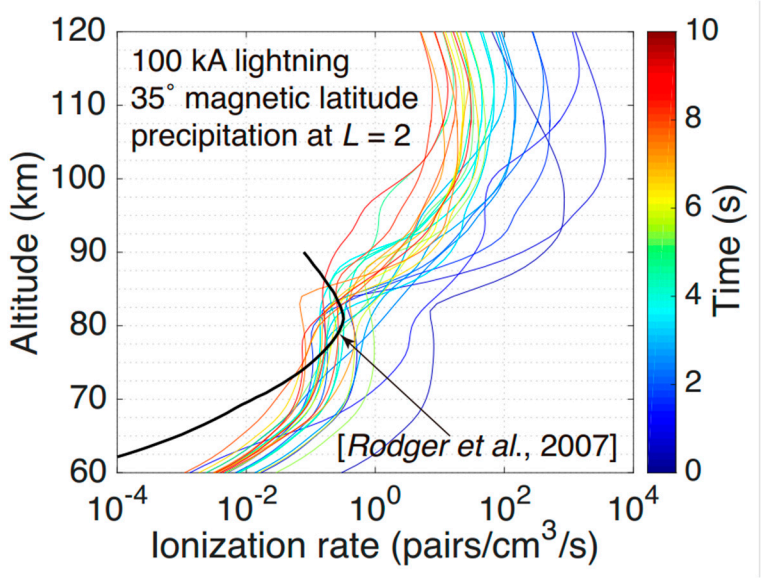


Figure 3. Computed ionospheric electron density profiles during a lightning-induced energetic electron precipitation event at L = 2 lasting for 10 s, together with the mean LEP ionisation production profile of Rodger et al. [52]. From Xu et al. [51].

Rodger et al. [52] discussed lightning-generated whistlers that couple the troposphere, the Van Allen radiation belts and the lower ionosphere through whistler-induced electron precipitation (WEP) at 1.9 < L < 3.5. Lightning-produced whistlers interact with n = 1 cyclotron-resonant radiation belt electron, leading to pitch angle scattering into the bounce loss cone and precipitation into the atmosphere. Figure 4 shows a map of the modelled mean precipitation energy flux due to WEP deposited into the upper atmosphere at 100 km altitude [52]. "The plot includes both "primary" WEP (from lightning in the same hemisphere) and "secondary" WEP (from conjugate lightning), producing high WEP rates in both hemispheres at American longitudes due to North American lightning. However, there is no symmetry between the northern and southern hemispheres in Figure 4 as more electrons precipitate into the lightning-source hemisphere than into the conjugate hemisphere. In addition, lightning activity is more common in the northern hemisphere where there is more land, such that the rate of energy deposited by WEP into the atmosphere is higher for the northern hemisphere than the southern" [52].

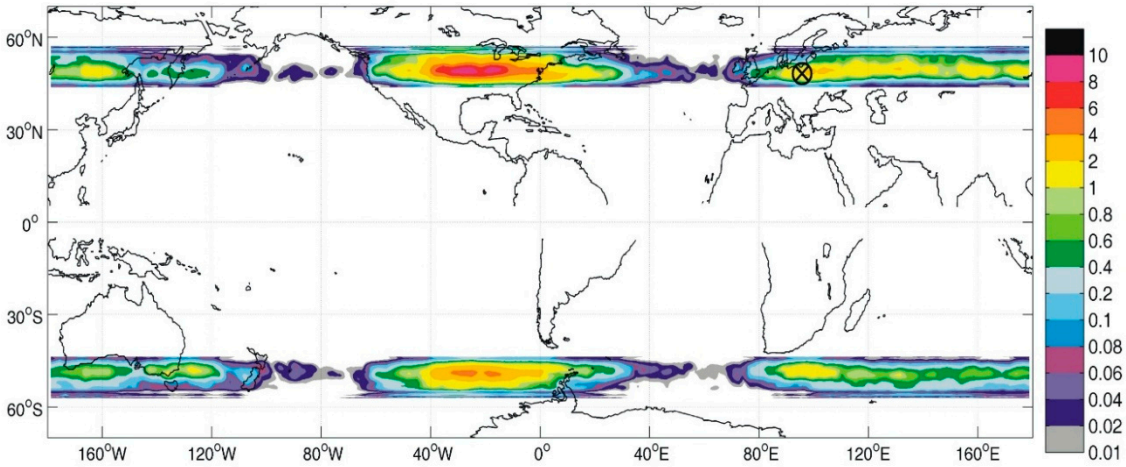


Figure 4. Map showing the expected global distribution of energy flux deposited by WEP into the upper atmosphere, in corrected geomagnetic coordinates for the IGRF of 2003, in units of 10^{-5} erg cm^{-2} s^{-1} [52]. The ringed cross in Poland is for a region of high WEP-driven ionisation rates where chemical model calculations were carried out.

Rodger et al. [52] compared the WEP-produced ionisation rate changes with those caused by Galactic Cosmic Radiation (GCR) and solar photo ionisation. They found that, during the day, "WEP is never a significant source of ionisation in the lower ionosphere for any location or altitude. At nighttime, GCR is more significant than WEP for all locations at altitudes <68 km, above which WEP starts to dominate in North America and Central Europe. Between 75 and 80 km altitude WEP becomes more significant than GCR for most locations at which WEP deposits energy. The regions in which WEP is the most important nighttime ionisation source are at ~80 km, depending on the relative contributions of WEP and nighttime solar Lyman α radiation flux". Although energetic electron precipitation can lead to changes in the neutral atmosphere by enhancing minor chemical species that play a key role in the ozone balance of the middle atmosphere [51], changes to the neutral atmosphere driven by WEP were found to be insignificant overall due to the short timescale of the WEP bursts.

Artemyev et al. [53] reported that "resonant interactions of energetic electrons with whistler-mode waves contribute significantly to the dynamics of electron fluxes in Earth's outer radiation belt. At low geomagnetic latitudes, these waves are very effective in the

pitch angle scattering and precipitation into the ionosphere of low equatorial pitch angle, tens of keV electrons and in the acceleration of high equatorial pitch angle electrons to relativistic energies". Electrons of up to 700 keV may also be precipitated by resonant interaction with whistlers, but this requires waves propagating quasi-parallel to the geomagnetic field [53]. They presented evidence that ducted whistlers efficiently precipitate relativistic electrons, showing simultaneous near-equatorial and ground-based measurements of whistlers and low-altitude electron precipitation measurements made by the ELFIN CubeSat [53]. Ducted waves (appearing on the ground) efficiently scatter relativistic electrons into the loss cone, contrary to non-ducted waves (absent on the ground) precipitating only <150 keV electrons. Their results indicated that ducted whistlers may be quite significant for relativistic electron losses; they further concluded that they should be studied statistically and possibly incorporated into radiation belt models.

Pailoor et al. [54] built a massive database of LEP events observed within the continental US (CONUS) by a network of VLF receivers. For each observed LEP event, based on the characteristics of the ionospheric disturbance, they applied a suite of models to estimate the total number of precipitating electrons, which were summed over all LEP events to quantify lightning's contribution within CONUS. They found that LEP events within CONUS appear to be capable of removing a substantial fraction (up to 1%) of radiation belt electrons between 33 keV and 1 MeV per day.

More than 400 LEP events were found by Linzmayer et al. [55] using wave- and charged-particle burst-mode data from the DEMETER satellite at $2.0 < L < 3.7$. As shown in Figure 5, most events were detected above the east coast of the USA, possibly because of the significant lightning activity there and the location being geomagnetically conjugate to the west of the South Atlantic Geomagnetic Anomaly, the longitude where electrons preferentially precipitate. The total precipitating energetic electron fluxes (up to about 200 keV) and wave intensities based on the average LEP properties and ducted lightning occurrence rate were estimated. Some two thirds of the events studied occurred at night, when the average 3 s LEP electron flux at 100 keV was ~20 cm^{-2} s^{-1} sr^{-1} keV^{-1}. At 100 keV, this corresponds to an electron flux of ~2 10^3 cm^{-2} s^{-1} sr^{-1}, in fair agreement with the observation of Rycroft [8].

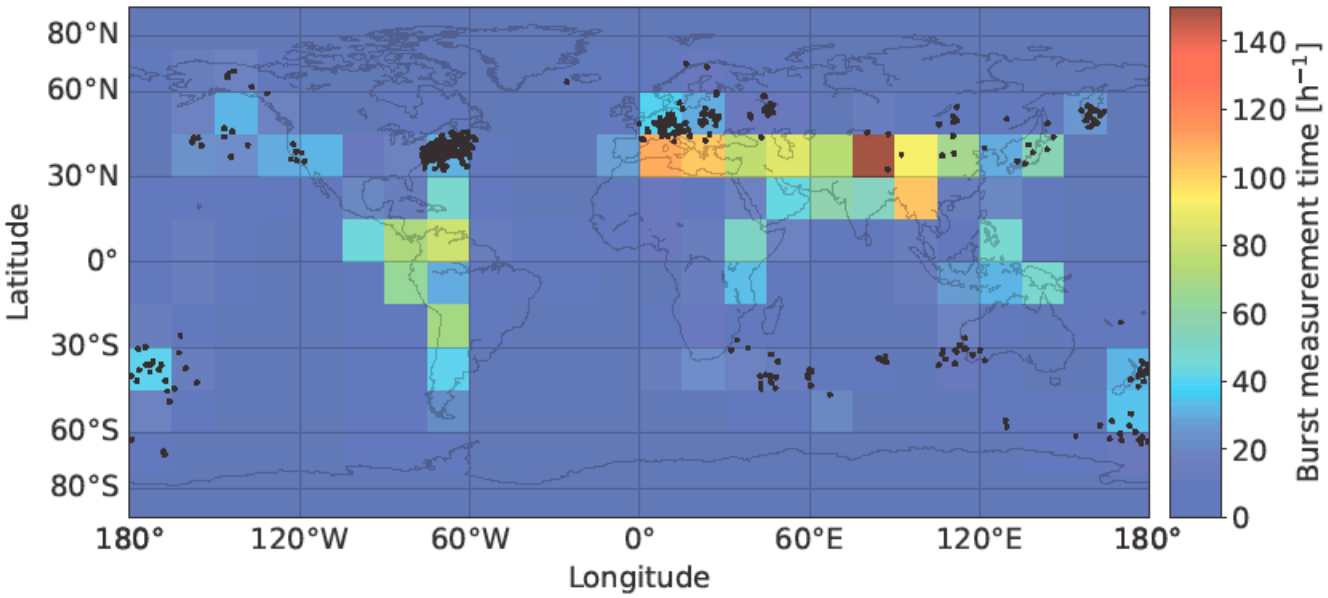


Figure 5. Map showing the geographic distribution of the detected LEP (>100 keV) events; individual LEP events are shown by small black circles. Most events occur at $2 < L < 3$ (in and around

the slot region) over the east coast of the USA, central Europe and the Kamchatka peninsula, where most northern middle-to-high-latitude thunderstorms occur, and in the regions that are geomagnetically conjugate to Europe and Russia. The total DEMETER burst-mode measurement time per hour in individual bins is plotted and colour-coded as shown on the right. From Linzmayer et al. [55].

Feinland et al. [56] discussed microbursts, which are rapid (sub-second) bursts of energetic electrons entering the atmosphere from the outer radiation belt, driven by interactions with chorus waves, but they can also occur in the inner belt and slot region, driven by lightning-generated whistlers. This lightning-induced electron precipitation is typically observed for electrons of some tens to hundreds of keV, even up to MeV energies. It indicates a coupling between near-Earth processes, such as lightning, and radiation belt processes, such as relativistic electron microbursts. In the SAMPEX/HILT (Solar Anomalous and Magnetospheric Particle EXplorer/Heavy Ion Large Telescope) ≥ 1 MeV electron dataset, from a low-altitude, high-inclination orbit, they observed 45 bouncing relativistic microburst packets in the inner radiation belt at L = 2 in the southern hemisphere, during or after geomagnetic storms, which are inconsistent with the chorus generation mechanism but are associated with strong northern hemisphere lightning discharges. As shown in Figure 6, the magnetic field strength at a given L-shell and altitude is weaker in the southern hemisphere than in the north, enabling electrons of a given pitch angle and energy to more easily reach lower altitudes before mirroring in locations within and around the South Atlantic Anomaly. These same bouncing electron packets may be mirroring above the altitude of SAMPEX in the northern hemisphere. Their Figures 1, 4 and 5 show a very strong periodicity, with a period of 0.2 s. They consider that this could be the bounce period of 1.4 MeV electrons with α_{eq} ~ 15° at L ~ 2 [56].

Rather than arising from the n = 1 gyro resonance, it is my opinion that these observations [56] could be indicative of the n = −1 gyro resonance at the equator, where, from Equation (1)

$$\omega + \omega_{B,e\,eq}/\gamma = \mathbf{k}.\mathbf{v} \quad (6)$$

Because, at L ~ 2, $\omega_{B,e\,eq}$ ~ 6.8 10^5 rad/s >> ω, with ω ~ 1.5 10^4 rad/s (f ~ 2.4 kHz), which approximates to

$$\mathbf{k}.\mathbf{v} = \omega_{B,e\,eq}/\gamma \quad (7)$$

Thus, **k** and **v** are in the same direction, and the waves (from the northern hemisphere lightning) interact near the equatorial plane with southward-travelling energetic (relativistic) electrons which can precipitate in the southern hemisphere. For 1.4 MeV electrons (γ ~ 3.7), and inserting k = $\mu\omega$/c, the refractive index of the plasma at the equator at L ~ 2 is μ_{eq} ~ ($\omega_{B,e\,eq}/\omega$)/γ ~ (68/1.5)/γ ~ 12, which is a realistic value for either ducted or non-ducted waves.

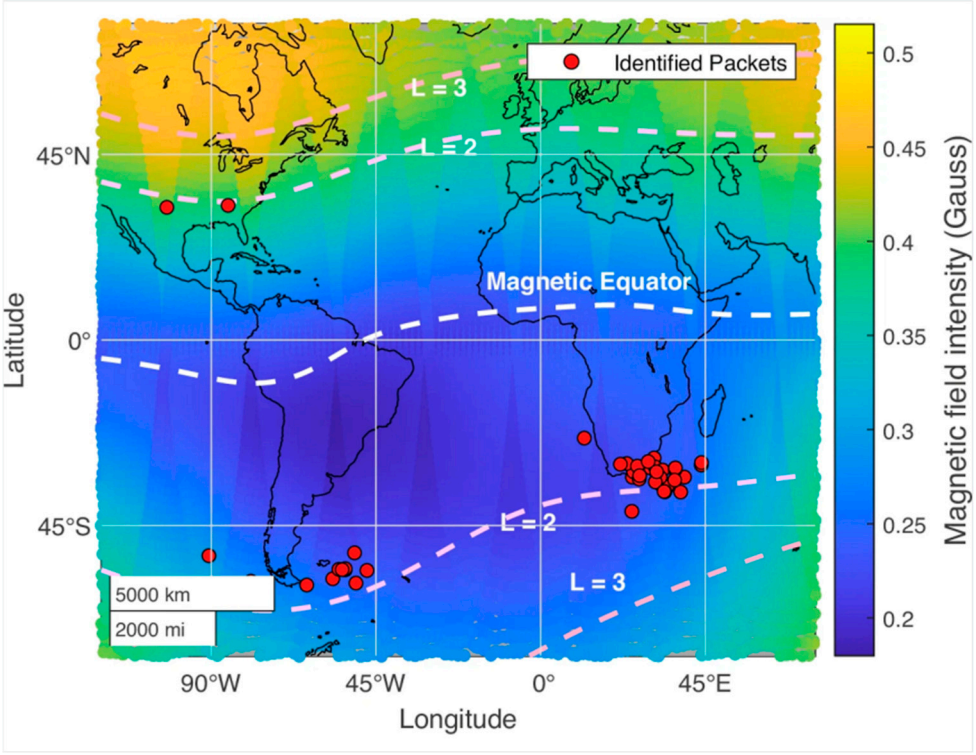


Figure 6. Map showing the geographic locations of each identified packet of bouncing ≥ 1 MeV electrons (red circles); L-shell contours are shown as white dashed lines, calculated using the IGRF-13 model. The geomagnetic field strength is given in Gauss, where 1 Gauss = 10^5 nT. From Feinland et al. [56].

Feinland and Blum [57] considered that understanding the dynamics of ultra relativistic (>1 MeV) electrons presents an ongoing challenge in the quest to accurately model space weather conditions. They presented a long-term study of MeV electron burst events detected in the inner radiation belt and slot region ($L < 2.5$). They searched 16 years of Solar Anomalous and Magnetospheric Particle Explorer (SAMPEX)/Heavy Ion Large Telescope data for microbursts and identified bouncing packets of electrons, which also exhibit a preference for occurring in the southern hemisphere [57]. They found that the number of events was associated with increases in geomagnetic activity that decayed on time scales of the order of tens of days.

Wang et al. [58] presented the first results from the mid-energy electron detector (MEED) aboard the Macao Science Satellite 1 (MSS-1), including 47 short bursts of lightning-induced electron precipitation (LEP) at $1.5 < L < 3.0$ detected in three months in 2023. The causative lightning discharges were definitively geo-located using ground-based VLF recordings made at Great Wall Station, Antarctica, with the LEP events occurring within < 1 s of the causative lightning and consisting of increased fluxes of 40 to 300 keV electrons. An example of these observations, interpreted as arising from the $n = 1$ cyclotron resonance, is presented in Figure 7.

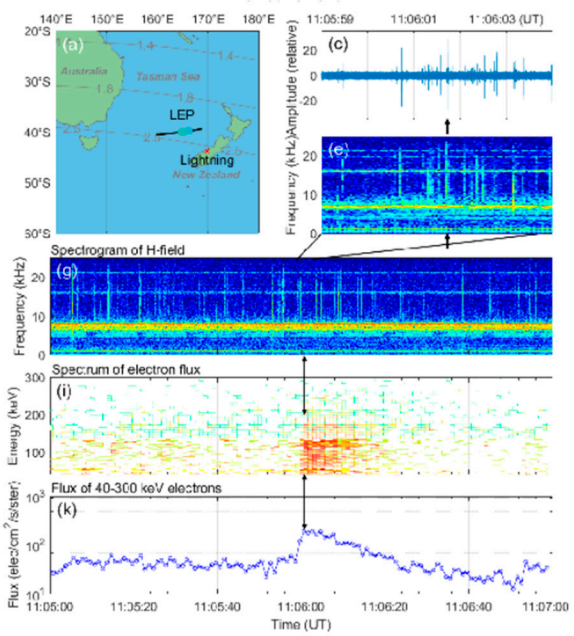


Figure 7. Lightning-induced electron precipitation (LEP) event recorded by the Macao Science Satellite-1 (MSS-1) on 1 June 2023 near New Zealand. (**a**) The location of the lightning at L ~ 2.6 and of the LEP, slightly equatorward, at L ~ 2.3, and a small portion of the orbit of the MSS-1 satellite. (**c**) The waveform of broadband VLF data from Great Wall Station, on the Antarctic Peninsula, for 5 s, showing sferics arising from lightning discharges; (**e**) and (**g**) dynamic spectrograms of the broadband VLF data for 5 s and 2 min, respectively. (**i**) Electron spectra from the medium-energy electron detectors on MSS-1, showing bursts of precipitated electrons from ~50 to 180 keV lasting for ~ 15 s. (**k**) The time-varying integral flux of 40 to 300 keV electrons which, during the LEP, exceeds 3.10^2 cm^{-2} s^{-1} sr^{-1} for a few s. From Wang et al. [58].

Using 7.5 years of data from the medium-energy X-ray telescope (ME) and high-energy X-ray telescope (HE) onboard the Insight-HXMT satellite, in an orbit (~550 km altitude) with 43° inclination, Zhao et al. [59] detected over 90 lightning-induced electron precipitation (LEP) events. These events mainly occurred near the southeastern coast of South Africa and over North America, distributed broadly within the L-shell range of 1.5 < L < 3, as shown in Figure 8. They exhibited seasonal variations, with most occurring in the local summer or autumn; they were observed exclusively at night, with a pulse period range of 0.2 to 0.45 s (peaking at 0.35 s), whereas Feinland et al. [56] found the pulse period to be ~0.2 s. Their pitch angle distribution maximised at ~90° to the geomagnetic field, and their occurrence correlated with solar activity but not with the geomagnetic storm (Dst) index [54]. The energy of the precipitating electrons was estimated to be 100 to 400 keV using the ME data, consistent with the range of tens to hundreds of keV observed by the HE. If 0.35 s is indeed the bounce period of the energetic electrons at L ~ 2, their energy is ~150 keV, which lies within the estimated range derived from the observations.

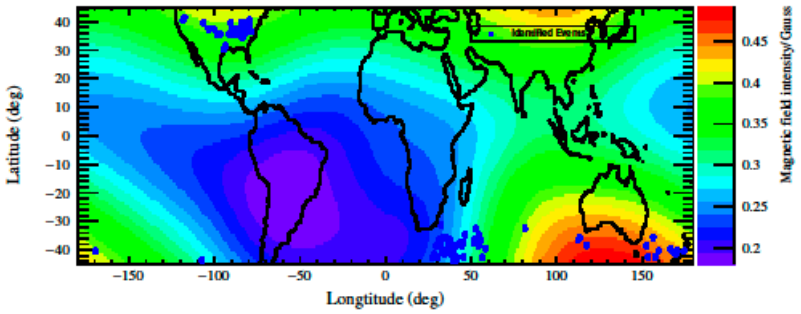


Figure 8. Map showing the geographic distribution of LEP events, with latitudes <43°, resulting in Europe and northern Russia not being covered, as reported by Zhao et al. [54]. These LEPs occur mostly over the USA, to the southeast of South Africa and between Australia and New Zealand, at 1.5 < L < 3. The geomagnetic field intensity is for IGRF-13. From Zhao et al. [59].

Abel and Thorne [60] discussed electron pitch angle diffusion rates due to Coulomb collisions and resonant interactions with plasmaspheric hiss, lightning-induced whistlers and signals from ground-based VLF radio transmitters. The bounce-averaged quasi-linear pitch angle diffusion coefficients were put into a pure pitch angle diffusion equation to obtain L-shell and energy-dependent equilibrium distribution functions and precipitation lifetimes. The relative effects of each scattering mechanism were considered as a function of electron energy and L-shell. Model calculations accurately described the enhanced loss rates in the slot region, as well as the reduced scattering in the heavily populated inner radiation belt [60]. They plotted the gyro resonant electron energy and a model plasmaspheric electron density N_{eq} profile against L-value, similarly to [10]. "The sensitivity of the rate of energetic electron pitch angle scattering and precipitation loss due to Coulomb interactions with thermal plasma and resonant wave-particle interactions with plasmaspheric hiss, lightning-generated whistlers and VLF transmitter signals was computed for a realistic range of plasma and wave parameters [61]. The computed scattering rates were found to be most sensitive to the choice of mean wave frequency and the wave normal angle; the frequency bandwidth and angular spread in propagation direction were relatively unimportant". Abel and Thorne [61] showed that "all three classes of waves must be included together with Coulomb collisions in any realistic analysis of inner magnetospheric electron scattering. They found that the long-term energetic electron population beyond the inner belt is largely controlled by plasmaspheric hiss and, to a lesser extent, by lightning-generated whistlers, while VLF transmitter signals constitute the principal loss mechanism over the range $1.3 \leq L \leq 2.4$. The region below L = 1.3 is dominated by Coulomb collisions" [61]. These are important conclusions.

Lauben et al. [62] presented a combined ray-tracing and test particle formulation that calculated the spatiotemporal electron precipitation flux signatures at ionospheric altitudes of obliquely propagating lightning-generated whistler waves. The detailed gyro resonance scattering of trapped energetic electrons into the atmospheric loss cone over a broad range of L-shells determined the precipitation fluxes over several tens of degrees of latitude and longitude up to 20° poleward of the lightning discharge. For oblique whistler intensities matching satellite observations (10 to 30 pT), precipitating fluxes of 10^{-3} erg cm^{-2} s^{-1} were found. "Lightning-generated oblique whistler-induced electron precipitation deposits appreciable energy into the upper atmosphere at midlatitudes and contributes significantly to the loss of ~ 100 keV radiation belt electrons, particularly over 2.2 < L < 3.5 where the slot region exists" [62].

Trakhtengerts and Rycroft [63] focused attention on the quasilinear and nonlinear physics of cyclotron interactions between magnetospheric whistler-mode waves and

energetic electrons on dipolar geomagnetic flux tubes. These interactions can lead to the generation of noise-like emissions or phase-coherent discrete signals in the frequency–time domain. In the magnetosphere, hiss is accompanied by a smooth electron precipitation pattern. Discrete emissions, such as chorus or emissions triggered by whistlers or by ground-based VLF radio transmitters, exhibit rapid temporal variations associated with the fine structure of the distribution function of the radiation belt electrons. This could be a transient step-like deformation or a well-organised beam, prepared by initial noise-like emissions or by a quasi-monochromatic whistler–wave packet, respectively [63]. These cause the properties of the electrons to evolve rapidly in time and on relatively short spatial scales. Bursts of precipitating electrons are created, and these can contribute significantly to the depletion of the radiation belts.

After briefly reviewing the theory of the gyro resonant interactions between a quasi-monochromatic whistler-mode wave and energetic electrons trapped in the magnetosphere, Trakhtengerts et al. [64] extended this theory to consider such interactions for a natural whistler arising from a lightning discharge. Near the equatorial plane of the magnetosphere, whistler components above the nose frequency can accelerate energetic electrons. This acceleration takes place when the gyro resonant electrons are trapped by the wave field. The acceleration rate in this regime is much greater than the stochastic acceleration in the un-trapped regime. It is not accompanied by pitch angle scattering, which characterises the un-trapped regime. For example, at L = 3, a gyro resonant electron with an energy of 6 keV and a pitch angle of 45° could have its energy increased by 24% to 7.4 keV and its pitch angle changed to 70° after a single interaction with a whistler whose frequency changes from a third to half of the equatorial gyro frequency. Highly anisotropic distributions of Van Allen radiation belt electrons with ''pancake'' pitch angle distributions can result from such an acceleration.

The acceleration of relativistic electrons in an inhomogeneous geomagnetic field during their resonant interaction with longitudinally propagating whistler-mode waves of varying frequency was considered by Demekov et al. [65]. Earlier studies of the efficiency of this acceleration were generalised to include relativistic effects, and an expression for the energy gain for a wide range of initial energies was obtained.

Cotts et al. [66] modelled "LEP events at any longitude and midlatitude L-shell by accounting for the effects of precipitating electrons which are backscattered from the atmosphere. The model of atmospheric backscatter, which included an asymmetric (non-ideal dipole) geomagnetic field model in calculations of the pitch angle of backscattered electrons entering the conjugate hemisphere, accounted for all the observable characteristics of LEP events. By combining the effects of atmospheric backscattering with radiation belt electron loss rates due to lightning at a single longitude, it was possible to develop a global estimate of the radiation belt electron loss due to lightning".

To conclude this section, I take the results of observations of individual LEP events, in terms of their electron number flux, to estimate their energy input into the upper atmosphere. For >40 keV electrons in a single whistler-induced precipitation event, the number flux is ~2.5 10^3 electrons cm^{-2} s^{-1} sr^{-1} for 2 s at L = 3.3 according to [8], ~10^{-3} erg s^{-1} cm^{-2} at 2 < L < 3 [27] and at L = 2.3 [32], ~2 10^3 cm^{-2} s^{-1} sr^{-1} for 3 s at 2 < L < 3 [55], 3 10^2 cm^{-2} s^{-1} sr^{-1} for ~4 s at L = 2.3 [58], and ~10^2 $cm^{-2}s^{-1}$ sr^{-1} at L ~ 2 (for 100 < W < 300 keV electrons) [37]. Taking an average value of 2 10^3 cm^{-2} s^{-1} sr^{-1} for 3 s at 2 < L < 3, for a downward flux over 2π sr, the flux is ~ 1.2 10^4 cm^{-2} s^{-1}. Thus, in 3 s, the flux is ~ 4 10^4 cm^{-2}. For an electron of ~ 100 keV, its velocity is ~1.6 10^8 m s^{-1} (0.55c) and its kinetic energy W is given by

$$W = (\gamma - 1)\, m_o c^2 \quad (8)$$

Thus, W = 0.55 9 10^{-31} 9 10^{16} = 4.4 10^{-14} J = 4.4 10^{-7} erg. The energy flux for a single LEP event is 1.2 10^4 4.4 10^{-7} erg cm^{-2} s^{-1} = 5.3 10^{-3} erg cm^{-2} s^{-1}, which is in remarkable agreement

with the value of ~10^{-3} to 10^{-2} erg cm^{-2} s^{-1} derived in [23,28]. For a 2 s long event, the energy flux is therefore ~ 10^{-2} erg cm^{-2}.

In SI units, the energy flux of a single LEP event is 1.2 10^{4} 4.4 10^{-10} J m^{-2} s^{-1} = 5.3 10^{-6} J m^{-2} s^{-1}. For a 2 s long event, the energy flux is ~10^{-5} J m^{-2}.

I now estimate the area in the ionosphere over which precipitation happens. To do this, I consider the dimensions of the whistler duct within which the whistler–energetic electron interaction occurs. In his ray-tracing studies, Strangeways [67] modelled the duct as a Gaussian enhancement in the electron density, with a scale length (standard deviation) of 215 km in the equatorial plane at L ~ 3. Using the conservation of magnetic flux law, this maps down to the ionosphere at 100 km altitude as 25 km. Below a whistler duct of ~ 25 km radius, the energy input is therefore 20 10^{-5+8} = 2 10^{4} J, which can be compared with the energy input of ~10^{9} J in an average lightning flash, of which ~3 10^{4} J lies within the spectral range of 1 to 100 kHz [68].

5. Plasmaspheric Hiss and Energetic Electron Precipitation

Following on from Rodger et al. [30], Hardman et al. [69] found that during a large geomagnetic storm in October 2011, the trapped fluxes of >30, >100, and >300 keV outer radiation belt electrons were enhanced at 3 < L < 4 during the storm's main phase. A gradual decay of the trapped fluxes was observed over the following week, even though no significant precipitating electron fluxes could be observed aboard the Polar Orbiting Environmental Satellite (POES). "Using the Antarctic-Arctic Radiation-belt (Dynamic) Deposition–VLF Atmospheric Research Konsortium receiver network to investigate the characteristics of the electron precipitation, weak electron precipitation was observed on the dayside for 5 to 7 days, consistent with being driven by plasmaspheric hiss, which they concluded can be a significant influence on the evolution of the outer radiation belt trapped flux that lies inside the plasmapause" [69].

Energetic electron precipitation at higher L-shells driven by three types of whistler-mode waves were evaluated by Li et al. [70]; these were plume whistler-mode waves, plasmaspheric hiss, and hiss observed outside the plasmapause. A plasmaspheric plume is a long, tail-like stream of cold, dense plasma that extends outward from the plasmasphere at L ~ 4.5 into the magnetosphere at up to L ~ 6, and it can become detached from the main plasmasphere; such plumes generally occur between dusk and midnight. By quantitatively analysing three conjunction events between Van Allen Probes and POES/MetOp satellites, together with quasi-linear calculations, they found that plume whistler-mode waves (50 < f < 500 Hz) were most effective in pitch angle scattering loss, particularly for the electrons from tens to hundreds of keV [69]. This was the first direct evidence of effective pitch angle scattering driven by plume-ducted whistler-mode waves ~100 pT, which is critical for understanding energetic electron loss processes in the magnetosphere.

Ma et al. [71] presented a global survey of energetic electron precipitation from the equatorial magnetosphere due to hiss waves in the plasmasphere and plasmaspheric plumes. During disturbed times, hiss inside the plasmasphere primarily caused electron precipitation at $L > 4$ over 8 h < MLT (magnetic local time) < 18 h, and hiss waves in plumes caused the precipitation at $L > 5$ over 8 h < MLT < 14 h and $L > 4$ over 14 h < MLT < 20 h. The characteristic energy of precipitating electrons increased from ~20 keV at $L = 6$ to ~100 keV at $L = 3$.

Sugo et al. [72] used high angular resolution data of ~10–100 keV electron flux obtained by the medium-energy particle experiments–electron analyser onboard the Exploration of energization and Radiation in Geospace (ERG) satellite for two events of strong electron precipitation due to strong plasmaspheric hiss at ~1 kHz at 5 < L < 6. Strong

scattering occurred, leading to a substantial filling of the loss cone within ~15° magnetic latitude away from the geomagnetic equator.

6. Chorus and Energetic Electron Precipitation

This is a large subject, which I shall introduce here, because it is very important in relation to outer radiation belt dynamics. Oliven and Gurnett [73] showed, using observations made with the Injun 3 satellite, that bursts of precipitating ≥ 40 keV electrons and VLF chorus emissions occurred simultaneously. They discovered that these observed "microbursts" were always accompanied by a group of VLF chorus emissions; chorus was not necessarily accompanied by microbursts [56]. The maximum region of microburst occurrence was from 04 h ≤ MLT ≤ 13 h at ~5.6 < L < 8.5.

Lorentzen et al. [74] reported on SAMPEX-observed relativistic (>1 MeV) electron precipitation from the radiation belts at 4 < L < 6 with bursty temporal structures lasting <1 s. They found that this phenomenon can occur at all local times but was most often seen between 02 and 10 MLT. VLF chorus was also observed to occur preferentially at these times. Using data from the Polar satellite plasma wave instrument, they demonstrated that relativistic electron microbursts and VLF chorus with frequencies <2 kHz were correlated. Wave–particle interactions strongly scatter electrons into the loss cone. Electron microbursts from tens to hundreds of keV were associated with chorus waves, since they resonate at the equator with whistler-mode waves at chorus frequencies.

Horne and Thorne [75] noted that resonant interactions with whistler-mode chorus waves provide an important process for electron loss and acceleration during storm times. They showed that storm time chorus waves outside the plasmapause (L ~ 4) can scatter electrons <60 keV at the equator into the loss cone and accelerate trapped electrons up to ~1 MeV at large pitch angles. They suggested that off-equatorial pitch angle scattering by chorus waves is responsible for relativistic microburst precipitation.

Horne et al. [76] reported that, for the outer radiation belt, electron precipitation at >300 keV peaks during the main phase of magnetic storms, whereas at >1 MeV precipitation peaks during the recovery phase. Precipitation at >300 keV can occur at all geographic longitudes in both hemispheres, whereas that at >1 MeV occurs mainly poleward of the South Atlantic Geomagnetic Anomaly. The data suggested that wave–particle interactions were strong enough to precipitate >300 keV electrons into the bounce loss cone (the bounce loss cone angle at the equator, α_{eq}, where the geomagnetic field is B_{eq}, is given by $\sin^2 \alpha_{eq} = B_{eq}/B_{100km}$), but that they precipitated >1 MeV electrons into the drift loss cone (where they drift in longitude eastwards into the weak field region of the South Atlantic Geomagnetic Anomaly and precipitate into the atmosphere at ~100 km altitude there).

Glauert et al. [77] presented results from a "radiation belt model which solves a 3-D Fokker-Planck equation incorporating the effects of radial diffusion, wave-particle interactions, and collisions. Chorus, plasmaspheric hiss, and lightning-generated whistlers were modelled using calculated diffusion coefficients and wave models based on satellite data parameterised by both the auroral (*AE*) and geomagnetic activity (*Kp*) indices. The model for plasmaspheric hiss and whistlers included the variation of wave normal angle distribution of the waves with latitude" [77]. They found that 1 to 2 kHz waves made a significant contribution to energetic electron losses for $L^* < 3$ and that whistlers with 2 < f < 5 kHz had a limited effect on the loss of MeV electrons for $2.0 < L^* < 5.5$ (L^* is defined in the Appendix).

Short-lived (<1 s) but intense electron precipitation, known as microbursts, may contribute significantly to electron losses in the outer radiation belt [78]. Their origin has been suggested to correlate with resonant scattering by whistler-mode chorus waves. Chen et al. [78] presented a "numerical model that reproduces a series of electron bounce

packets in response to individual chorus elements. Their results indicated that the precipitation only occurs in the leading electron packet whereas subsequent packets form because of the following bounce motions. An analysis based on wave propagation and the gyro resonance condition yields an approximate time-energy regime of electron microbursts which is valuable for interpreting and modelling low Earth orbit satellite observations of electron flux variations in response to their interaction with magnetospheric chorus waves".

The dynamics of the radiation belts are largely affected by the resonant interactions of energetic electrons with whistler-mode chorus waves, which play a direct and crucial role in the acceleration and loss of radiation belt electrons. One of the most conspicuous properties of chorus waves is the size of the wave packets. Aryan et al. [79] used the comprehensive wave data from the Van Allen Probes mission to draw a global map of the sizes of chorus wave packets along the geomagnetic field beyond the plasmasphere; they found that these varied between ~1000 and 2000 km. The largest chorus wave packets were observed at 02 h < MLT < 10 h, when chorus wave activity was also highest at magnetically active times [79].

Chen et al. [80] investigated radiation belt electrons produced during geomagnetic storms and then removed by collisions with the lower atmosphere. An efficient loss process is microbursts, i.e., the strong, transient precipitation of electrons over a wide energy range, from tens of keV to sub-relativistic and relativistic energies. They showed that these energetic electron microbursts may be caused by ducted whistler-mode chorus waves.

The ionospheric electron density profile from 60 to 150 km altitude under the influence of energetic electron precipitation (EEP) was studied by Chen et al. [81]. They noted that the derived electron profile was roughly consistent with the observed one. They found that EEP has a significant impact on the electron density in the altitude range from 60 to 90 km at 4.5 < L < 8 and 09 h < MLT < 14 h, particularly during strong geomagnetic activity.

Ozeke et al. [82] used data from the Polar Orbiting Environmental Satellites (POES)/Space Environment Monitor in low Earth orbit to assess the relationship between the trapped and precipitating electron fluxes in integral energy channels > 30, > 100, and > 300 keV. They highlighted a strong non-linear relationship between the fluxes of trapped and precipitating electrons, with the ratio of precipitating to trapped fluxes only becoming significantly enhanced once the trapped flux reached a critical level. Intense chorus waves at 1.0 < f < 1.5 kHz predominantly occur in the dawn sector (22 h < MLT < 06 h) during geomagnetically active time intervals, matching the locations where intense, trapped flux events occur, at 4 < L < 5. These results suggest that the intense chorus waves are generated by the high flux of trapped electrons which pass through the dawn sector along open drift paths before exiting the magnetosphere, and that this is associated with strong energetic electron precipitation into the atmosphere. The transition from low to high levels of precipitation is consistent with the theory of Kennel and Petschek [7], whereby intense chorus waves are excited that trigger pitch angle diffusion, resulting in energetic electron precipitation and limiting the flux of trapped electrons. Using electron flux data from POES and chorus wave data from the Van Allen Probes, they further tested their observations against theoretical predictions [7]. Their inescapable conclusion was that flux capping processes [7], which were not included in current state-of-the-art radiation belt simulation models, control intense atmospheric precipitation of energetic electrons at energies from ~10 to 100 keV.

Chakraborty et al. [83] used multi-spacecraft data to demonstrate that intense chorus waves (0.7 < f < 3 kHz) are excited during electron injection events that drive rapid radiation belt electron loss across a limited energy range from ~100 to 300 keV through

strong pitch angle diffusion. They suggested that such electron injection events should be associated with intense losses in a limited energy range, with the resulting atmospheric impacts having strong local time dependence, and with preferential energy deposition in the dawn sector during auroral substorm injection events.

Chorus sometimes falls into two distinct frequency bands, with a lower band (0.1 to 0.5 $f_{B,e\ eq}$) and an upper band (0.5 to 0.8 $f_{B,e\ eq}$) and a significant gap at about 0.5 $f_{B,e\ eq}$, as shown in [84]. Gao et al. [85] proposed a novel generation mechanism for chorus, which they called lower-band cascade, whereby a density mode with a frequency equal to that of lower-band chorus is generated by the ponderomotive effect (inhomogeneity of the electric field amplitude) along the wave vector, and the upper-band chorus, with a frequency twice that of lower-band chorus, is generated through wave–wave couplings between lower-band chorus and the density mode. This idea does not seem to have been accepted by the chorus research community.

Nunn et al. [84] used a one-dimensional Vlasov Hybrid Simulation (VHS) computer code to simulate the dynamical spectra (i.e., frequency versus time spectrograms) of ELF/VLF chorus signals (< 1 kHz < f < 10 kHz). Using measurements of the amplitude of chorus (up to 300 pT) made in the source region close to the geomagnetic equator aboard the four-spacecraft Cluster mission (see their Figures 2 and 3), and knowing the local gyro frequency, cold plasma density, and L-shell, the chorus signals were reproduced with remarkable fidelity. Frequency sweep rates of up to 10 kHz s^{-1} were simulated, as observed. They found that the sweep rate is a falling function of increasing cold plasma density, again in accord with observations [84]. They concluded that nonlinear electron cyclotron resonance, whereby electrons become trapped by the whistler-mode wave ("phase trapping") and a hole is formed in their distribution function, is the mechanism responsible for the generation of chorus signals just outside the plasmasphere; electrons are accelerated by the chorus waves. As the interaction region moves away from the geomagnetic equator, and with propagation away from the equator, rising frequency tones (chirps) are generated [84].

Demekov et al. [65] found that the energy gain during a single interaction between an electron and a whistler-mode wave packet can be only <0.1 keV just inside the plasmasphere, whereas it can reach > 10 keV at 5 < L < 6, just outside the plasmapause where the plasma density, N_{eq}, is only 2 cm^{-3} (see their Figure 1). In the case of chorus emissions generated there, this mechanism can be effective for electrons with perpendicular energies, $W_{\perp}$, several times higher than the energy of the electrons generating the chorus in the first place. They concluded that it is difficult to calculate the flux of these electrons [65].

Saito et al. [86] discussed relativistic electron microbursts; they showed that modulations of a few Hz embedded in the precipitating electron flux variations are associated with the repetition period of the whistler chorus elements. Their simulation results indicated that microbursts of relativistic electrons in the outer belt are caused by chorus wave–particle interactions on field lines at high latitudes (4 < L < 6) and that a series of rising tone elements in the chorus produce modulation of the microbursts at a few Hz.

Considering that the flux of energetic electrons in the Earth's outer radiation belt can vary by several orders of magnitude over time scales of less than a day, in response to changes in properties of the solar wind instigated by solar activity, Thorne [87] showed that "the variability in the radiation belts is due to an imbalance between the dominant source and loss processes, caused by a violation of one or more of the adiabatic invariants. For radiation belt electrons, such a non-adiabatic behaviour is primarily associated with energy and momentum transfer during interactions with various magnetospheric waves". Thorne [87] presented a "review of advances in both our understanding and global modelling of such wave-particle interactions, which have led to a paradigm shift in our

understanding of electron acceleration in the radiation belts. It appears that internal local acceleration, rather than radial diffusion, is the dominant acceleration process during the recovery phase of magnetic storms".

Watt et al. [88] noted that the "pitch angle scattering of electrons can limit the stably trapped particle flux in the magnetosphere and precipitate energetic electrons into the ionosphere. Whistler-mode waves generated by a temperature anisotropy [7] can mediate this pitch angle scattering over a wide range of radial distances and latitudes but, to correctly predict the phase space diffusion, it is important to characterise the whistler-mode wave distributions that result from that instability". They investigated the global propagation and growth of whistler-mode waves by studying millions of growing ray paths. They demonstrated that the wave distribution at any one location is a superposition of many waves at different points along their trajectories and with different histories. They showed that, for observed electron plasma properties, very few ray paths undergo magnetospheric reflection; most rays grow and decay within 30° of the magnetic equator.

Hseih and Omura [89] investigated the properties of whistler-mode wave–particle interactions at oblique wave normal angles to the background magnetic field, finding that the flow of electromagnetic energy of waves with frequencies < 0.5 $f_{B,e}$ can be nearly parallel to the ambient magnetic field. They thereby confirmed that the gyro averaging method, which averages the cyclotron motion to the gyro centre and reduces the simulation from two dimensions to one, is valid for oblique wave–particle interactions. "Multiple resonances appear for oblique propagation but not for parallel (ducted) propagation. They calculated the possible range of resonances with the first order resonance condition as a function of electron kinetic energy and equatorial pitch angle, showing that multiple resonances contribute to the acceleration and pitch angle scattering of energetic electrons. They noted that electrons with energies of a few hundred keV can be accelerated efficiently to a few MeV through the $n = 0$ Landau resonance".

Chorus waves propagating in the Earth's magnetosphere are often observed with oblique wave normal angles (WNAs) [90]. Studying chorus wave fields at $L = 4.5$, Hseih and Omura [90] used test-particle simulations to trace electrons with energies between 10 keV and 6 MeV interacting with these waves. Very strong (~2 nT) and very oblique chorus waves cause the precipitation of electrons, especially at energies of 50 to 100 keV, with $\alpha >$ 45°, for the $n = -1$ cyclotron resonance [90]. The regions where the nonlinear growth of whistler-mode chorus waves is largest were studied by Ebihara et al. [91]. They found that whistler waves can first grow due to a linear mechanism (pitch angle anisotropy) in the dawn sector outside the plasmapause, followed by a rapid, nonlinear mechanism accompanied by rising tone chorus elements.

Tao et al. [92] considered whistler-mode chorus waves that are quasi-coherent electromagnetic emissions with frequency chirping. Various models have been proposed to understand the chirping mechanism, a long-standing problem in space plasmas. Based on an analysis of the effective wave growth rate and electron phase space dynamics in a self-consistent particle simulation, they proposed a phenomenological model called the "Trap–Release–Amplify" (TaRA) model for chorus [92]. In this model, space structures of correlated electrons are formed by nonlinear wave–particle interactions, which mainly occur downstream of the equator. When released from the wave packet in the upstream, these electrons lead to the selective amplification of new emissions which satisfy the phase-locking condition to maximise wave power transfer, and result in frequency chirping.

Teng and Tao [93] discussed whistler-mode chorus in the Earth's magnetosphere, which plays a crucial role in magnetospheric electron dynamics by accelerating and scattering electrons over a wide energy range. There are two proposed mechanisms to explain the frequency chirping of chorus waves. In the first model, this is proportional to

the inhomogeneity of the geomagnetic field [84,94]. In the second model, the frequency chirping rate is proportional to the wave amplitude [95,96]; this can be verified by self-consistent particle-in-cell simulations. Wu et al. [94] showed that the former mechanism agreed better with Van Allen Probes observations. The Trap–Release–Amplify model [92] was also discussed in [93]. Studies of the similarities and differences between the TaRA model and other models deepen our understanding of the nonlinear processes involved in wave–particle interactions [95].

In a substantial review paper, Hanzelka and Santolik [97] studied the significant role of nonlinear wave–particle interactions in microbursts and pulsating aurorae, associated with the rapid scattering of energetic electrons by whistler-mode chorus, which can reach amplitudes of about 1% of the ambient geomagnetic field (~300 nT). A discussion of the conflicting interpretations of the roles of resonant electron current and magnetic field inhomogeneity was included [97].

The spatiotemporal variability of whistler-mode waves outside the plasmasphere, referred to as chorus, was investigated by Watt et al. [98]. Their analysis showed that low-variability (on a time scale of ~5 min) waves are dayside hiss, whose typically high occurrence rate (~0.8) decreases with substorm activity, and that high-variability waves are sporadic post-midnight/dawn-sector substorm-driven chorus with a typical occurrence rate of 0.2. Kurita et al. [99] considered "chorus waves as a key driver of variations in energetic electron fluxes through wave-particle interactions, traditionally being understood as a diffusive process [7], to account for long-term electron flux variations (>several minutes). Chorus waves can also cause rapid (<1 s) electron acceleration and significant flux variations within less than a second through a nonlinear wave-particle interaction" [99]. Detecting these rapid accelerations is a great challenge due to the limited time resolution of conventional energetic electron instruments aboard satellites.

Zhou et al. [100] considered that low-frequency chorus waves (<0.1 $f_{B,e\,eq}$, where $f_{B,e\,eq}$ is the equatorial electron gyrofrequency) can induce the depletion of relativistic electrons in Earth's radiation belts by effective pitch angle scattering. These low-frequency waves demonstrate distinct effects on radiation belt dynamics compared to typical chorus waves (0.1–0.8 $f_{B,e\,eq}$). An analysis of Van Allen Probes data revealed that low-frequency chorus waves predominantly occur at 00 h < MLT < 07 h and at $L \sim 6$. These waves show a strong correlation with intense substorm activity and moderate geomagnetic storms. Their excitation mechanism is driven by the coexistence of isotropic low-energy electrons (<30 keV) and anisotropic high-energy electrons (>50 keV) during the storm's peak [100].

Chen et al. [101] noted that both theoretical and observational studies indicate that the feedback from energetic electrons significantly influences chorus wave excitation and evolution. In this study, they quantified electron precipitation driven by chorus waves using self-consistent simulations at $L = 6$ with typical magnetospheric plasma parameters. Electrons in the ~10–200 keV range are precipitated, reaching intensities of $\sim 10^8$–10^9 cm^{-2} s^{-1} sr^{-1} MeV^{-1}, consistent with typical observed values [95]. As a comparison, test particle simulations underestimate the precipitation intensity by nearly an order of magnitude.

The modulation of chorus waves on time scales of a few s plays a crucial role in modulating electron precipitation intensity, leading to the formation of pulsating aurorae. Chen et al. [102] performed self-consistent particle-in-cell simulations with typical magnetospheric plasma parameters at L = 6 to quantify chorus modulation driven by plasma density variations and compressional magnetic field fluctuations. They demonstrated that chorus modulation is determined by nonlinear wave–particle interactions, in which the condition for nonlinear wave growth is highly sensitive to the values of the background plasma parameters. The resulting electron precipitation in the

~10–200 keV energy range exhibits modulation on comparable time scales, consistent with observations of pulsating aurorae.

Němec et al. [103] considered that chorus waves are arguably the most important electromagnetic emissions in the Earth's magnetosphere, being responsible for both the energisation and loss of radiation belt electrons. Chorus generation, inherently related to nonlinear wave–particle interactions, as well as the frequency–time shapes of individual elements forming it, are not yet fully understood. They used multipoint high-resolution measurements performed by the Cluster spacecraft to address the north–south symmetry of the source with respect to the magnetic equator. A particular chorus event offered a unique situation in which the Cluster spacecraft moved along nearly the same field line, with one located north and another south of the magnetic equator. A detailed wave analysis employing lower-resolution data was used to demonstrate that the emissions propagate away from the equator, as expected. They then showed that the structure of the upper-band chorus (> ~ 5 kHz, i.e., >0.5 $f_{B,e\,eq}$) was generally different at the two spacecraft, while the lower-band chorus emissions (<0.5 $f_{B,e\,eq}$) detected by both spacecraft were very similar [103]. This indicates that the lower-band chorus source radiates nearly symmetrically toward both hemispheres, while the upper-band chorus does not.

"Energetic electron scattering and precipitation driven by electromagnetic whistler-mode waves are key processes controlling electron losses in the outer radiation belt and near-Earth plasma sheet. Intense whistler-mode waves can induce nonlinear resonant interactions, including phase trapping and phase bunching, which enable much faster precipitation than diffusive scattering by low-amplitude waves" [104]. These nonlinear processes are sensitive to wave coherence; the influence of wave packet variability (resulting in the loss of coherence) on precipitation efficiency still has to be explored.

Grach et al. [104] investigated a well-characterised event of energetic electron precipitation observed by ELFIN at low altitudes in combination with near-equator THEMIS observations of waves. Using test-particle simulations driven by THEMIS wave measurements, they reproduced the observed energy range of precipitating electrons and directly quantified how wave packet variability alters resonant dynamics and loss rates. They found that, although wave packet variability significantly perturbs nonlinear resonant dynamics, the net precipitation fluxes remain largely unchanged. The discussion of chorus in this section is by no means comprehensive; there are many more recent papers that could have been included.

Saitoh et al. [105] discussed whistler-mode chorus emissions, characterised by nonlinear growth and frequency chirping, that are regarded as the origin of relativistic acceleration of particles in the radiation belts and pulsating aurorae. They demonstrated the spontaneous excitation of chirping whistler waves in a hot-electron high-β plasma (where β is the ratio of the plasma pressure to the magnetic pressure) in an "artificial magnetosphere", a levitated dipole experiment in the laboratory. These experiments suggest that the generation and nonlinear growth of coherent chorus emissions are ubiquitous in a dipole magnetic field configuration.

7. VLF Radio Transmitter Signals and Energetic Electron Precipitation

Bell et al. [106] discussed early experiments on VLF wave injection into the magnetosphere. They reported on transmissions for the Siple station transmitter that were received by the high-altitude Japanese satellite, EXOS-B. Transmitter-triggered emissions inside whistler-mode ducts were also recorded during the six-day period after the large geomagnetic storm of 13 August 1979. They suggested that this involved a region of wave growth near the magnetic equator, with an amplitude threshold for emission triggering.

Two years later, Inan et al. [107] examined the temporal and spectral shape and the absolute flux level of electron pulses precipitated by a VLF transmitter from a theoretical

viewpoint. A test-particle model of the gyro resonant wave–particle interaction was applied to the parameters of the observed cases for calculating the precipitation characteristics. The temporal shapes of the precipitation pulses were found to be controlled by the pitch angle dependence of the electron distribution near the edge of the loss cone and by the multiple interaction of the electrons with the waves due to significant atmospheric backscatter.

Vampola [108] used high-resolution pitch angle measurements made on the S3-3 satellite to find the angular distributions of 235 keV electrons precipitated in the slot region of the magnetosphere ($2.3 < L < 2.5$) by signals from the ground-based VLF transmitter in Australia, NWC, operating at 22.3 kHz, at $L \sim 1.4$. He compared these with the pitch angle distributions that would be produced by various patterns of longitudinal interaction regions; the observed electrons were in the drift loss cone. The data fitted well both with theoretical calculations of the ionospheric field intensity patterns above a transmitter and with a similar pattern of received field intensities measured along a satellite traverse in the magnetic conjugate region. The agreement between the data and field patterns implied a linear or quasi-linear wave–particle interaction. The energy–frequency relationship between the electrons and the waves meant that the interaction region was lower on the geomagnetic field line than the equator.

A year later, Vampola and Adams [109] used similar measurements, made in the drift loss cone region of the magnetosphere, of fluxes of 108–654 keV electrons precipitated in the inner zone, in the slot region, and in the outer zone of the magnetosphere to show that they were consistent with the precipitation produced by the same ground-based VLF transmitter in Russia, UMS, operating at 17.1 kHz, at $L \sim 1.7$. The predicted gyro resonance energy response was then compared with the satellite observations; complete agreement was obtained. The study indicated that whistler-mode waves from ground-based VLF transmitters, which previously had been shown to produce precipitation in the inner zone and slot regions, were almost certainly also precipitating electrons in the outer zone.

Rosenberg et al. [110] examined energy–time features of bremsstrahlung X-ray microbursts and compared them with the predictions of a test-particle simulation model of wave-induced electron precipitation resulting from gyro resonant wave–particle interactions in the magnetosphere. The observations were obtained on a balloon flight at Siple station, Antarctica ($L \sim 4.2$), on 30 December 1980, at a time when the Siple VLF transmitter was operating. The energy and time evolution of the microbursts, which were generated by chorus, were studied for X-rays in the energy range of 25 to 175 keV. An algorithm designed to search the >25 keV counting rate data for single isolated microbursts identified 651 events in 3 h. The distribution of burst durations ranged from 0.2 to 1.2 s. Approximately two-thirds of the distribution were narrow bursts (0.2–0.6 s) and the rest wide (0.6–1.2 s), with the average burst durations being ~0.4 s and ~0.7 s, respectively, for the two classes. The precipitation was characterised by exponential electron spectra with e-folding energies of 25–50 keV. Individual and superposed microburst profiles showed that the X-ray energy spectrum was softest (equivalent to a reduction in the e-folding energy to ≤5 keV) near the peak of the energy influx. Computer simulations of the flux–time and energy–time profiles of direct and mirrored electron precipitation induced by a whistler-mode wave pulse of 0.2 s duration and a linear frequency increase from 2 to 4 kHz were performed for plasma, energetic electron and wave parameters appropriate for the location and geophysical conditions of the observations. The wave pulse was representative of the VLF chorus elements that were observed at Siple station and at the conjugate location of Roberval, Quebec, Canada, during the microburst activity on that day. For both direct and mirrored events, the combined effect of the latitude dependence of the energy of maximum gyro resonant scattering and energy dispersion led to energy spectrum variations that were qualitatively

consistent with the microburst observations [76]. The average burst durations in the two cases were ~0.3 s (direct) and ~0.7 s (mirrored). On this basis, they identified the narrow microbursts with electrons which were precipitated directly after undergoing pitch angle scattering interactions with the wave pulse; the wide microbursts were identified with electrons which, after interacting with the wave, mirrored in the conjugate ionosphere before precipitating into the southern ionosphere.

The powerful ground-based VLF transmitters NWC and UMS gyro resonantly scatter ~100 keV electrons from the inner radiation belt onto trajectories from which they precipitate into the atmosphere as they drift eastward. To obtain a better understanding of the underlying wave–particle mechanisms, Datlowe et al. [111] studied energetic electron data from the Burst and Transient Source Experiment (BATSE) on the Compton Gamma Ray Observatory satellite. Wave-particle interactions were detected when the satellite traversed a cloud of energetic electrons which had been scattered into quasi-trapped trajectories by the VLF waves. These data provided the first detailed measurements of the frequency of occurrence of the quasi-trapped electron fluxes as a function of local time at the transmitter; the precipitation was most often observed in the predawn hours. As with the seasonal changes, the local time variations were governed by the absorption of the transmitted VLF waves during their propagation through the ionosphere.

Numerical ray tracing with Landau damping was used by Kulkarni et al. [112] to calculate >100 keV electron precipitation signatures induced by hypothetical VLF transmitters distributed broadly in geomagnetic latitude and operating over a wide range of frequencies. A 0.5 s pulse from each source was simulated and the attenuation to the base of the magnetosphere for geomagnetic latitudes from 10 to 60° was calculated. It was found that the source's geographic location affected induced precipitation more strongly than the operating frequency or radiated power. Transmitters located at 35–45° magnetic latitude caused the most >100 keV precipitation for 10–40 kHz waves, while locations at magnetic latitudes <15° or >55° were least effective at precipitating energetic electrons. In all cases, induced precipitation increased as the operating frequency decreased, with 10 kHz waves from a source at 35° magnetic latitude being the most effective at precipitating > 100 keV electrons. The precipitation signatures produced by five existing ground-based VLF transmitters were also simulated; NWC (Australia, 22.3 kHz, L ~ 1.4) induced the strongest >100 keV electron precipitation, followed by NPM (Hawaii, 21.4 kHz, L ~ 1.17), NAU (Puerto Rico, 40.8 kHz, L ~ 1.35), NAA (Cutler Maine, 24.0 kHz, L ~ 2.6), and NLK (24.8 kHz, Washington State, L ~ 2.4). The modelled precipitated energy flux due to NWC peaked at 10^{-5} erg cm^{-2} s^{-1} at L ~ 2, and for the other four transmitters at ~ < 10^{-6} erg cm^{-2} s^{-1} at L ~2 (see their Figure 7(f)) [112].

Signals from VLF transmitters can leak into space and contribute to the dynamics of energetic electrons in the inner radiation belt and slot region. Meredith et al. [113] used about five years of plasma wave data from the Van Allen Probe A satellite to construct models of the observed wave power from VLF transmitters as a function of L* (Roederer's parameter, which is slightly different from McIlwain's parameter, L, see Appendix), magnetic local time and geographic location. The average power peaks primarily on the nightside of the Earth for VLF transmitters at low latitudes. At higher latitudes, the peak average power extends further in magnetic local time due to more extensive periods of nighttime in the winter months. The nighttime power is typically orders of magnitude more than that found near noon, implying that precipitated electron loss rates will also maximise in this MLT region. The observed power from any VLF transmitter is tightly confined in longitude, with the nightside peak power typically falling by a factor of 10 within 10° longitude of the location of the peak signal. Table 1 of Meredith et al. [113] is a valuable list of VLF transmitters, with the name, location, frequency, geographic

coordinates, power, L-value and UT time when it is midnight MLT shown for each one. Meredith et al. further showed that the total average wave power from all VLF transmitters was in the range of 3 to 9 pT^2 in the region of $1.3 < L^* < 3.0$, with approximately 50% of this power emanating from three VLF transmitters, NWC, NAA, and DHO38 (in Germany, 23.4 kHz, L ~ 2.1) [113]. They presented global maps of the expected powers of transmitter signals; Figure 9 provides an example at frequencies between 24.29 and 25.58 kHz, which includes the NLK (Seattle, Washington state, USA, 24.8 kHz) and NML (North Dakota, USA, 25.2 kHz) transmitters and the unid25 transmitter (South Korea, 25.0 kHz). Transmissions from the very powerful transmitter NAA (Cutler, Maine, USA, 24.0 kHz) are also evident.

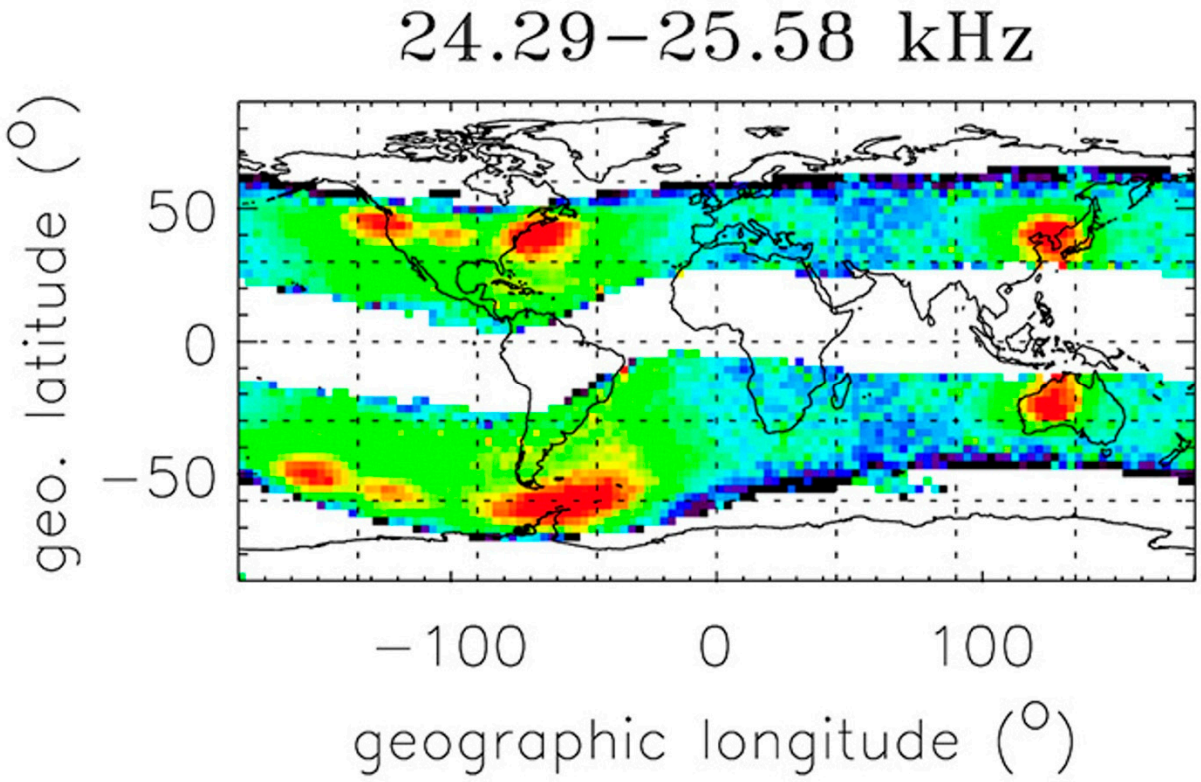


Figure 9. Global map of the average wave electric field power spectral densities, calculated for VLF transmitters operating between 24.29 and 25.58 kHz on the nightside, where the wave power maximises (shown in red), and mapped to their geomagnetically conjugate points [113].

Sauvaud et al. [114] examined the significance of the signal from the VLF transmitter NWC situated at L = 1.4 on the inner radiation belt using DEMETER satellite global observations. DEMETER is in a sun-synchronous polar orbit at ~700 km altitude; data were recorded at L-values < 5.6 [40]. Sauvaud et al. [114] found that enhancements in the 100–600 keV drift loss cone electron fluxes at L values between 1.4 and 1.7 were linked to NWC operation and to ionospheric absorption. They used the term ''wisp'' to describe the feature measured between L ~ 1.8 and 1.4, which shows a decrease in electron energy with increasing L, as expected from cyclotron resonance theory [8]. They found that about 300 times more 200 keV electrons were driven into the drift loss cone during NWC transmission periods than during non-transmission periods. The energetic electron flux east of the NWC transmitter at L = 1.7 was ~10 cm^{-2} sr^{-1} keV^{-1} (see their Figure 2) [114]. The correlation between the flux of resonant electrons and the Dst index showed that the electron source intensity was controlled by magnetic storm activity.

Gamble et al. [115] showed that such nighttime enhancements were initially observed within a few degrees of longitude west of NWC and were present in 95% of the data east of the transmitter for times when the transmitter was broadcasting. When contrasted with periods when NWC was non-operational, there were typically about 430 times more 100 to 260 keV resonant electrons present in the drift loss cone at 1.67 < L < 1.9 due to NWC transmissions. Zhang et al. [116] found that NWC-induced precipitation of 30–100 keV electrons occurred at 1.8 < L < 2.1 whereas that for 100–300 keV electrons was at 1.67 < L <1.9. Figure 8 of [115] shows ~200 keV electron fluxes at L ~ 2.5 east of the NPM transmitter at night ~10^2 cm^{-2} s^{-1} sr^{-1} keV^{-1}, which is comparable with the precipitating fluxes due to LEPs [55].

Graf et al. [117] investigated two years of DEMETER observations when the transmitter NPM at Lualualei, Hawaii (L ~ 1.17), was operating at 21.4 kHz. Only a few cases of individual pulses of transmitter-induced precipitation of inner radiation belt electrons were found. A comparison of the observed precipitating flux with predictions based on ray tracing the wave and test-particle modelling of the wave–particle interaction indicated that the precipitated flux of >100 keV electrons peaks at L ~ 1.9 and may be at higher energies than the ~100 keV peak predicted by the model.

Li et al. [118] analysed 2 s long constant frequency (3 kHz) tones generated by the Siple transmitter (L ~ 4.3) that were amplified during one-hop propagation to Lake Mistissini, Quebec, Canada. For the interval examined, only 11% of Siple transmissions were successfully received in the conjugate hemisphere, with quiet geomagnetic conditions being significantly more conducive to successful reception. The total wave growth for the events examined was estimated to be between 5 and 40 dB, and the nonlinear growth rates were in the range of 20 to 350 dB s^{-1}. The observations showed that, as the nonlinear growth rate increases, the duration of nonlinear growth decreases. Omura et al. [119] reviewed observational, theoretical and numerical studies of VLF radio emissions triggered by the transmitter at Siple Station. The emissions were narrow band, long enduring, with an amplitude which saturated at ~30 dB greater than the amplitude of the triggering pulse; they often swept in frequency at a rate of ~1 to 4 kHz s^{-1}.

Nunn [120] studied the non-linear interaction of cyclotron resonant electrons with a narrow-band whistler wave travelling along a magnetospheric duct. Using the non-linear equations of motion, it was found that resonant electrons became stably trapped in the wave; because of the magnetic field spatial inhomogeneity, these electrons changed their energy. Nunn et al. [121] used a one-dimensional Vlasov Hybrid Simulation (VHS) code to simulate the triggering of strong emissions. For this to occur, electron trapping by the wave must occur by the time the triggering pulse reaches the equator; both the initial pulse amplitude and pulse length must be above minimum values. At a moderate linear growth rate at the equator of 50 dB s^{-1}, these triggering thresholds were clearly apparent. They noted a tendency for risers to be preferentially triggered, particularly at intermediate growth rates; this result confirmed the Siple experimental studies. They found that it is the cold plasma density in the equatorial plane, N_{eq}, that mainly controls the sweep rate magnitude; at a cold plasma density of 400 cm^{-3} within the plasmasphere, the riser sweep rate is ~1 kHz s^{-1}. The sweep rate becomes much larger as the density decreases [121]. The controlled excitation of nonlinear whistler-mode wave particle interactions, via experiments, theory and computation, was excellently reviewed by Golkowski et al. [122]; they considered it to be a cornerstone of near-Earth space physics. Various active experiments, including the Siple Station transmitter and HAARP [123], were reviewed. "Theory and numerical simulations point to cyclotron resonance with counter streaming particles in the 10–100 keV range as the dominant process. A key feature of the non-linear interaction is the phase-trapping of resonant particles by the wave that is believed to drive non-linear wave amplification and the triggering of free-running emissions" [122].

Whistler-mode waves from powerful ground-based VLF transmitters can resonantly scatter plasmaspheric energetic electrons and precipitate them into the atmosphere [124]. An analysis of Van Allen Probes measurements up to L = 3 of the wave electric field power and the inferred wave magnetic amplitude as a function of L, MLT, season, and Kp revealed the localisation of VLF wave intensity and its variation with geomagnetic activity [124]. Using this VLF wave model with existing hiss and lightning-generated wave models in radiation belt simulation codes, Ma et al. [124] performed numerical calculations of the corresponding quasi-linear pitch angle diffusion rates to demonstrate the crucial role played by VLF waves from transmitters in energetic electron loss at L < 2.5. VLF waves from ground-based transmitters decreased electron lifetimes by one to two orders of magnitude for 0.4 to 1 MeV electrons at L = 1.5, for 30 to 300 keV electrons at L = 2.0, and for 2 to 50 keV electrons at L = 2.5. Their electron lifetime calculations showed that VLF transmitter waves have a minimal impact on >500 keV electrons compared to plasmaspheric hiss [124]. They also found that ducted whistler-mode waves were more effective than non-ducted waves at L > 1.7.

Ross et al. [125] reported that Van Allen Probes observations show that the radio waves from each specific VLF transmitter are highly localised, peaking on the nightside in the vicinity of the transmitter. They constructed global statistical models of the bounce-averaged electron pitch angle diffusion coefficients for each individual VLF transmitter as a function of L^* between 1.1 and 3.0, MLT and geographic longitude, and showed that VLF transmitter waves weakly scatter electrons into the drift loss cone. They found that, at energies ~40 keV, VLF transmitter waves reduce electron lifetimes by an order of magnitude or more, down to ~ 100 days, in the slot region. At ~500 keV, VLF transmitter waves reduce electron lifetimes by an order of magnitude or more, down to ~200 days near the outer edge of the inner radiation belt. VLF transmitter waves are ineffective at removing >2 MeV electrons from the inner belt and slot region. They found that, in general, non-ducted VLF transmitter waves are marginally less effective than ducted waves at reducing electron lifetimes by a factor of up to 4.

Harid et al. [126] discussed the interaction between coherent whistler-mode waves from VLF transmitters and energetic radiation belt electrons, which can result in the pitch angle scattering of electrons into the bounce loss cone and their subsequent precipitation. Whereas previous modelling efforts focused on the computation of diffusion coefficients for a Fokker–Planck model, the nonlinear effects of large-amplitude coherent waves causing electron precipitation were evaluated using a Vlasov–Liouville (VL) model which computed the phase space particle distribution function directly. They demonstrated the importance of phase trapping over a range of wave amplitudes (up to 200 pT) in contributing to the precipitation. They calculated the time evolution of the precipitated flux due to short-duration whistler-mode pulses. The physical parameters used were typical of those associated with the Siple Station wave injection experiment [119].

Using observations from the Energetic Particle Telescope on the PROBA-V satellite, Cunningham et al. [127] compared the measured energetic electron fluxes, as a function of local geomagnetic field strength, when the NWC transmitter was 'on' versus when it was 'off'; they found enhanced fluxes only when NWC was 'on' and at night. They showed that electrons of up to 800 keV had been scattered by gyro resonant interactions with signals from NWC, by ducted waves at L < 1.55 and by unducted waves at L > 1.65.

A new development in the subject was the DSX spacecraft, which carried a high-voltage VLF (~2.7 kHz) transmitter and a sensitive broadband receiver to medium Earth orbit in 2019 [128]. During many pulsed transmission experiments, DSX detected apparent "boomerang" echoes when its emitted waves of up to 1 mV/m from 7° south magnetic latitude at L ~ 2.1 were refracted in the magnetosphere (magnetospherically reflected) and returned to the spacecraft. Starks et al. [128] simulated a series of these detected pulses

using cold plasma ray tracing to characterise their likely wavelengths, indices of refraction, and initial wave normal angles. The waves going south were magnetospherically reflected, whereas those crossing the equator going north could go below 2000 km altitude into the ionosphere [128]. They were lightly damped, and their emitted wave normal angles were almost 90° from the geomagnetic field direction. Because of this, it is unlikely that they would cause energetic electron precipitation.

McCullough et al. [129] reported on VLF transmission experiments between the DSX spacecraft and the Arase (ERG) spacecraft. On 4 September 2019, these two satellites came within 410 km of each other and were in geomagnetic alignment. At this time, signals with frequencies ~10 kHz were successfully transmitted from DSX to Arase, marking the first successful reception of a space-to-space VLF radio signal. The Arase measurements were consistent with field-aligned wave propagation as expected from linear cold plasma theory. This capability to directly inject VLF waves into near-Earth space provides a new way to study the dynamics of the radiation belts.

The observed signatures of electron precipitation from the inner radiation belt were shown by Selesnick et al. [130] to be consistent with the theory of resonant scattering by whistler-mode waves, with the waves originating from the VLF radio transmitter, NWC. The conclusion was based on a stochastic model of electron transport that included pitch angle diffusion, radial diffusion, energy loss, and azimuthal drift. The wave scattering causes an increase in the quasi-trapped electron intensity, forming a "wisp" signature.

VLF transmitter waves play a critical role in energetic electron scattering and precipitation from the inner radiation belt, one type of which is called "wisp" precipitation [131]. Wisps exhibit dispersive energy versus L-shell spectra due to the evolution of electron cyclotron resonance conditions with almost monochromatic VLF transmitter waves. Shen et al. [131] reported on such observations of inner belt wisp precipitation events with full pitch angle resolution in the energy range of 50 to ~500 keV as measured by the Electron Loss and Fields Investigation (ELFIN) Cubesat at L < ~2. Statistical observations (82 events) revealed occasional (18 events) wisp precipitation events with local bounce loss cone electron flux enhancements, which provided new information compared with flux enhancements measured in previous studies only in the drift loss cone. Based on magnetic field and plasmaspheric density models, quasilinear theory, and detailed pitch angle distributions of wisps from ELFIN, Shen et al. [131] "estimated the wisp electron bounce-averaged pitch angle diffusion coefficients to be ~10^{-4} to 10^{-2} s^{-1}. These are several orders of magnitude larger than the diffusion rates calculated from models using global statistical averages of VLF transmitter wave power".

When these estimated diffusion coefficients are used to deduce the associated local transmitter wave amplitudes near the equator, based on quasi-linear calculations from a transmitter-induced electron diffusion model, the wave amplitudes are found to be > 1 mV/m [131]. Such inferred wave amplitudes exceed the theoretical threshold amplitude for non-linear interactions. This strongly suggests that it is necessary to include non-linear effects for an accurate evaluation of energetic electron scattering and precipitation by VLF transmitter waves. Shen et al. [132] quantitatively evaluated the roles of hiss, plume hiss and chorus in modulated precipitating energetic electrons observed at low altitudes by Electron Loss and Fields INvestigation (ELFIN) and measured near the equator by Time History of Events and Macroscale Interactions during Substorms THEMIS. Electron precipitation was observed from ~50 keV to <1 MeV with a spatial modulation.

The 19.8 kHz electromagnetic signals from the NWC transmitter in Australia produce a wisp-like energy distribution of precipitating energetic electrons from the Earth's inner radiation belt, observed by many Low Earth Orbiting (LEO) satellites [131]. Typically, satellites observe a single wisp with an energy that decreases with increasing L, which is produced by a first-order cyclotron resonance of transmitter signals with energetic

electrons. Xiang et al. [133] reported multiple wisps observed by the Relativistic Electron and Proton Telescope integrated little experiment-2 (REPTile-2) on board the Colorado Inner Radiation Belt Experiment (CIRBE) CubeSat. Based on simulation results, they demonstrated that cyclotron resonances with n = 1, −1 and 2 (Equation (1)) with highly oblique (large wave normal angle with respect to the geomagnetic field) NWC transmitter signals produce these multiple wisps.

Section 3.3 of the study of Ripoll et al. [134] provides an excellent overview—with a comprehensive bibliography—of the various wave processes whereby electrons are lost from the inner and outer radiation belts, as has been discussed here. Attention was focused on ground-based VLF transmitters, lightning-generated whistlers, whistler-mode hiss waves, plasmaspheric wave-induced precipitation, whistler-mode chorus waves, microbursts, electromagnetic ion cyclotron (EMIC) waves, and magnetosonic and electrostatic cyclotron harmonic waves. Section 3.4 of [134] is on determining loss processes, while Section 5 focuses on radiation belt modelling and Section 6.1 focuses on understanding nonlinear wave–particle interactions in the radiation belts [134].

The attenuation of VLF signals from lightning and ground-based VLF transmitters during trans-ionospheric propagation was considered by Marshall [135], as discrepancies had been found between satellite data and model calculations. Previous modelling efforts did not consider the self-absorption effect due to nonlinear heating and ionisation in the lower ionosphere. Here a self-consistent model of ionospheric heating was presented using a time-domain model of VLF wave propagation through the ionosphere up to ~ 100 km altitude. In this model, the ionospheric state was updated as the fields propagated, leading to changes in the electron-neutral collision frequency and the electron density, which in turn affected the wave propagation. He found that the inclusion of self-consistent heating causes a change in the trans-ionospherically propagating wave amplitude, which is ~1 to 2 dB for VLF transmitters, but >10 dB for large-amplitude lightning discharges [135].

The interaction of VLF transmitter signals with radiation belt electrons depends on their wave normal angles. In the equatorial interaction region, these can be either low (for ducted propagation) or comparatively large (non-ducted propagation). Experimentally distinguishing the two modes is complicated, as multicomponent spacecraft data typically do not extend to high-enough frequencies with a sufficient frequency resolution. An exception that Němec et al. [136] exploited was the observation of 11.9 kHz signals from Russian Alpha transmitters detected by the Van Allen Probes spacecraft. While ducted waves were detected less often, they tended to have larger Poynting fluxes, so the total power propagating in the two modes is thus comparable. Magnetic local time and the density fluctuations were found to be the main parameters controlling the relative fraction of ducted waves.

The effectiveness of signals from VLF transmitters on the ground for precipitating energetic electrons from the Earth's radiation belts depends on whether the signals are ducted along columns of enhanced plasma density. Gu et al. [137] showed that non-ducted propagation dominates over ducted propagation in both the occurrence and intensity of waves from the Russian transmitter at 11.9 kHz, as observed in Van Allen Probes data. Their ray tracing confirmed that the latitudinal distribution of wave vectors corresponded to non-ducted rather than ducted propagation—see Figure 10 from [137]. Further, Gu et al. [137] noted that "ducted waves are more efficient at scattering <800 keV electrons, primarily through first-order cyclotron resonance, while non-ducted waves allow Landau resonance and cyclotron resonances at higher equatorial pitch angles".

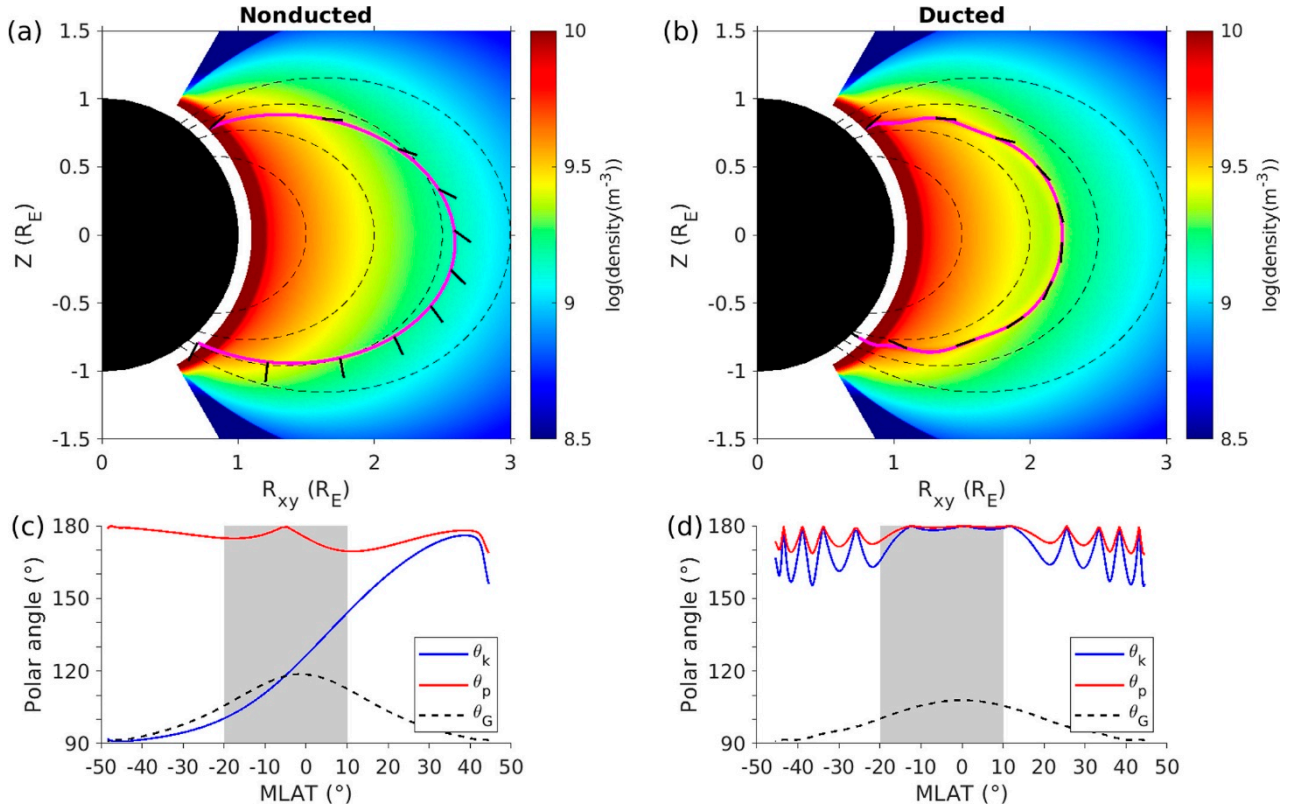


Figure 10. Short black bars show the wave normal directions of whistler-mode waves from the 11.9 kHz Alpha transmitter in Novosibirsk, Russia, launched at 700 km altitude at L = 2.2; the dashed lines show dipole magnetic field lines at L = 1.5, 2.0, 2.5 and 3.0. (**a**) A non-ducted ray (shown in purple) and (**b**) a ducted ray (shown in red) propagating through a model plasmasphere, with the electron density values being colour-coded (right-hand scale). For the non-ducted (**c**) and ducted (**d**) rays, the polar angles of **k** and the Poynting (energy flux) vector are plotted in the blue and red lines, respectively. As a result of the field line curvature, the wave normal of the non-ducted (**c**) ray gradually refracts radially outwards during southward propagation The oscillations in (**d**) clearly show the variations due to ducted propagation. Both rays reach the geomagnetically conjugate region corresponding to the northern source. There are two wave normal angles where the Poynting vector is parallel to the geomagnetic field; these are 0° and the Gendrin angle $\theta_G = \arccos(2f/f_{B,e})$. The grey areas show the magnetic latitude range where the Van Allen Probes observations were made. From Gu et al. [137].

Denton et al. [138] presented a summary of experimental optical observations made at 4278 Å (arising from the excited ionised nitrogen molecule) some 40 km from the powerful (~150 kW) VLF transmitter (JXN) operating at 16.4 kHz. Approximately 2.5 s after the transmitter was turned on, a sudden increase in optical emissions at 4278 Å was detected using a dedicated camera/charge-coupled device (CCD) monitoring system recording at a frequency of 10 Hz, causing pitch angle scattering. The optical signal was interpreted as being caused by a burst of electron precipitation lasting ~0.5 s, due to gyro resonant wave–particle interactions between the transmitted wave and scattering of the magnetospheric energetic electron population. The precipitation was centred on the zenith and had no detectable spatial structure.

Marshall et al. [139] presented numerical simulations of optical emissions in the ionosphere due to electron precipitation caused by ground-based VLF transmitters. Their Table 2 usefully lists the locations and frequencies of such transmitters. Ray tracing and precipitation calculations were made to estimate the energetic electron flux precipitated from the inner magnetosphere. These precipitated fluxes were used to estimate ionisation

profiles through Monte Carlo simulations, and the ionisation profiles were converted to photon volume emission rates. Their results showed that NWC precipitated a maximum flux of electrons of >100 keV equal to 10^{-5} erg cm^{-2} s^{-1} at L ~2.1. NWC created the strongest optical signature because of its high power, latitude of ~35°, and relatively low frequency. The resulting optical signal was found to have a peak intensity of <0.1 R [139].

Chen et al. [140] have recently presented a model based on tracing millions of ray paths from the topside ionosphere, with source emissions specified by DEMETER observations. Their simulation results demonstrated that the non-ducted wave propagation results were consistent with the observed distribution of both wave intensity and wave normal angles. Pitch angle scattering rates derived using the modelled wave distribution showed that the NWC transmitter enables a range of electron loss time scales from as short as 1 day to as long as 100 days, depending on the electron energy [140]. Signals from the powerful NWC transmitter cause energetic electron precipitation [108].

Xia et al. [141] have shed some light on the propagation of signals from the NWC transmitter in Australia which escape from the Earth–ionosphere waveguide and propagate into the magnetosphere. Observations made by the DEMETER satellite at ~700 km altitude have revealed a distinct pattern of concentric rings of the wave power distribution of the transmitter signal on the transverse (longitude versus L-shell) plane. Using data from other satellites, they found that the concentric ring pattern was still visible but had become less distinct. The pattern became more elliptical as the wave propagated from the southern ionosphere into the northern hemisphere and to higher L-shells. They performed ray tracing simulations under three conditions: ducted propagation, non-ducted propagation with vertical initial wave normal angles, and non-ducted propagation with a spread of initial wave normal angles [141]. The results showed that non-ducted propagation with spread wave normal angles best explained the observed evolution of wave power distribution pattern during the propagation. The mean wave power observed by the Van Allen Probes, at altitudes ranging from ~ 500 km to ~ 31,000 km, was about one to two orders of magnitude lower than that observed by the DEMETER satellite at ~700 km altitude.

8. Electrical Grid 50/60 Hz Waves and Power Line Harmonic Radiation (PLHR)

Power line harmonic radiation (PLHR), originating from the Finnish power system and from heavy industrial plants, penetrates the magnetosphere. Nunn et al. [142] considered numerous occurrences of PLHR-triggered VLF radio emissions observed on the ground in northern Finland; risers predominated, but fallers and hooks (in the frequency–time domain) were also observed. A well-established 1D Vlasov simulation code was used to simulate these emissions, using plausible magnetospheric data for $4 < L < 5.5$. The code reproduced risers, fallers and hooks, in close agreement with observations.

Parrot et al. [143], using DEMETER, observed emissions triggered by PLHR, man-made waves emitted at harmonics of 50 or 60 Hz; they were rising frequency tones or hooks with a starting frequency associated with a parent line at a frequency equal to a multiple of 50 or 60 Hz. They occurred preferentially during daytime, at $1 < f < 4$ kHz. It was shown that these emissions were rather frequent at high latitudes ($3 < L < 6$) above industrialised areas during periods of moderate magnetic activity; their average intensity was ~10 μV^2 m^{-2} Hz^{-1}. PLHR propagates in the magnetosphere and triggers emissions due to wave–particle interactions in the equatorial region [143].

To investigate the evolution of the wave properties of emissions from electrical grid systems on the Earth's surface (i.e., the fundamental frequency 50/60 Hz or power line harmonic radiation (PLHR) at low harmonics) reaching satellite altitudes in a dipole magnetic field, Xu et al. [144] created a numerical model to perform full-wave simulations.

They found that at middle and high magnetic latitudes (>40°, corresponding to L > 1.7), energy can propagate to high L-shells as whistler-mode waves. They showed that the wave properties of these power line emissions, including Poynting vector direction, wave normal angle and wave polarisation, obtained from their simulation results, were consistent with observations from the Van Allen Probes [144]. It is not known whether these waves might trigger the precipitation of trapped energetic electrons.

Nemec et al. [145] performed an analysis of PLHR events based on high-resolution multicomponent wave data from the two Van Allen Probes spacecraft during the entire duration of the mission (2012 to 2019). They showed that the wave intensities at 50/60 Hz were typically larger at the times when the spacecraft were above an industrialised region. This was the case for the North America region, providing evidence for the wave propagation to radial distances as large as about 4 Earth radii. The PLHR events were generally more intense during the night, presumably due to their lower attenuation in the ionosphere. They found that the events were typically right-handed elliptically or nearly circularly polarised, propagating at oblique wave normal angles from low-latitude sources but with more field-aligned wave vectors from high-latitude sources, indicating that ducting may play a role. Some of the events observed above the USA propagated northward toward the ground, which may be explained by the wave reflection in the southern hemisphere. Because the lowest PLHR frequencies are an order of magnitude lower than whistler frequencies, it is evident, from Equation (8), that if they did, the gyro resonant electron energies would be an order of magnitude greater than the hundreds of keV for n = 1 gyro resonances with whistlers, i.e., several MeV, which would be highly relativistic. Furthermore, because these signals are essentially continuous in time, it would be difficult to identify in observations a precipitation event that they could have caused.

The satellite DEMETER detected 133 PLHR events in six years above China that were associated with the development of China's electrical power network [146]. These PLHR events were usually at odd harmonics of 50 Hz; for nearly a half of them the central frequency was at 4 kHz < f < 4.5 kHz, whilst for the others it was between 1 kHz and 2 kHz or between 2 kHz and 2.5 kHz. More events were observed in winter than in summer [146].

9. Ionospheric Heating Experiments

Through the emission of high-frequency (>MHz) radio waves, ground-based ionospheric heating facilities can generate ELF (<3 kHz) and VLF (3 < f < 30 kHz) radio waves in the ionosphere, a portion of which can propagate into the Earth's radiation belts and influence the electron population there. Xu et al. [147] quantified these effects using measurements of plasma waves and high-energy electrons during the joint experiment conducted between the China Seismo-Electromagnetic Satellite (CSES) and the Russian ionospheric heater SURA at L ~2.6. They showed that SURA-generated ELF/VLF waves were mostly in the frequency range of 1 to 5 kHz as measured by CSES, with an amplitude of ~50 pT at 0.8 to 2 kHz. The overall structure was found to resemble previous measurements of ELF/VLF waves generated by the High-Frequency Active Auroral Research Program (HAARP) [123]. These waves can, in principle, influence electrons in the 100 to 250 keV energy range, mostly via pitch angle diffusion and scattering into the loss cone. By simulating the evolution of the energetic electron phase space density under the impact of SURA-generated ELF/VLF waves, their modelling supported a causal relationship between the SURA heating experiment and the CSES-observed dynamics of ELF/VLF waves and energetic electrons [147].

Based on the results of the experiments within the framework of the SURA-DEMETER program, Frolov et al. [148] analysed some features of the precipitation of energetic electrons from the radiation belt. The ionospheric F2 region was modified by

means of high-power continuous HF ordinary-mode radio waves. The region of electron precipitation stretched along the geomagnetic meridian to a maximum distance of 1300 km; the size of the region in the transverse direction was about 400 km. Ionosonde measurements showed that such precipitation led to the increased absorption of radio waves in the lower ionosphere. The precipitation of the energetic electrons (~100 keV), with fluxes of up to 100 cm^{-2} s^{-1} sr^{-1} keV^{-1}, was believed to be caused by their interaction with VLF radio waves generated by the interaction of the amplitude-unmodulated O-mode pump wave with the ionospheric plasma near the wave reflection height [148]. Very recently, Chernyshov et al. [149] reported further such experiments, in which electrostatic waves were transformed into whistler-mode waves that propagated up to satellite altitudes.

10. Jupiter's Magnetosphere

In recent years, it has been suggested that the same wave–particle interactions that are considered here could be operating in the magnetospheres of giant planets that have dipolar magnetic fields. To whet the reader's appetite, I mention three recent papers. Li et al. [150] state that, unlike Earth, where whistler-mode chorus is generally observed outside the plasmasphere and hiss is predominantly confined within it, Jupiter's magnetosphere frequently hosts both wave modes simultaneously. Using Juno observations, they presented a global survey of whistler-mode waves at Jupiter, demonstrating that both chorus and hiss are prevalent over $6 < M < 13$ (with M specifying the magnetic field line in Jupiter's magnetosphere as L does for the Earth); the chorus is confined to lower latitudes, with hiss extending to higher latitudes. Based on the observed wave and plasma characteristics, they applied physics-based global diffusion modelling to assess the separate and combined effects of chorus and hiss waves on energetic electron dynamics. The simulations showed that, "near regions of peak wave activity, chorus waves lead to net electron losses below ~1 MeV while producing acceleration at higher energies. Hiss waves primarily drive electron losses but, in combination with chorus waves, they can also enable electron acceleration above ~1 MeV at specific pitch angles" [150]. Wong et al. [151] investigated strong radio signals from lightning on Jupiter (at ~600 MHz, observed on the Juno mission) and compared them with signals from powerful lightning discharges on Earth. It would be interesting to find out if lightning on Jupiter causes the precipitation of energetic electrons from its magnetosphere.

Long et al. [152] identified large-scale depletions of energetic electrons along Europa's orbit, which are too deep to result from direct absorption by the moon alone. They showed that rapid electron losses, occurring within a timescale shorter than Jupiter's rotation, are driven by pitch angle scattering via whistler-mode waves co-located with Europa's orbit. This suggests that Europa maintains a plasma environment capable of sustaining a slot-like region, like that in Earth's Van Allen belts.

11. Chirping Signals

Chorus signals spontaneously generated in the magnetosphere by nonlinear wave–particle interactions resemble the sounds of birds chirping. Their frequency (~1 to 5 kHz) rises appreciably in a fraction of 1 s.

The mathematics of the chirp function has been reviewed by Blackledge [153]. The significance of the chirp function in the solution of a range of fundamental problems in physics was discussed in this paper, as were the contexts in which chirp functions play a central role. Attention was focused on the uniqueness of the chirp function regarding its use for convolutional coding and decoding in cryptography.

The linear frequency modulated chirp is defined by a function of time t given by $\exp(i\alpha t^2)$, where $i = -1^{1/2}$, and α is a constant known as the chirp rate; the instantaneous frequency is $2\alpha t$. A chirplet is any part of a chirp function that has been windowed in time [153]. This theory has yet to be applied to magnetospheric chorus, where α varies from 1 to 10 kHz s^{-1} or even more.

12. How Energetic Electron Precipitation Can Change the Earth's Upper Atmosphere

The book Physics and Chemistry of the Upper Atmosphere, by Rees [154], serves as a comprehensive textbook on aeronomy. It provides a rigorous physical and mathematical description of the Earth's upper atmosphere, principally the thermosphere and ionosphere. The text outlines the many processes operating in this region, including solar radiation, charged particle precipitation and the height profile of the ionisation rate that it causes, auroral phenomena, chemistry and fluid dynamics. In this section I ask, what is the impact of a single LEP event lasting 2 s, with its energy input of ~10^{-2} erg cm^{-2}, on the physics and chemistry of the upper atmosphere? From the results provided at the end of Section 4, it is reasonable to assume that the area in the ionosphere below a whistler duct is a circle of ~25 km radius, so the extra energy input to this region due to a LEP event is ~2 10^4 J.

Sinnhuber et al. [155] have considered that the precipitation of energetic charged particles into the atmosphere greatly disturbs its chemical composition from the upper stratosphere (~50 km altitude) to the lower thermosphere (~130 km). The most important effects are changes to the budget of atmospheric nitric oxides (NO_x = N, NO, NO_2) and to atmospheric reactive hydrogen oxides (HO_x = H, OH, HO_2), both of which contribute to ozone loss in the stratosphere and mesosphere.

Mironova et al. [156] discussed energetic electron precipitation (EEP) and the ion production rates in the upper atmosphere, which have already been mentioned here [51]. The correct estimation of EEP ion production and spectra for the computation of ionisation rates is an important issue. The parameterisation of atmospheric ionisation in the Earth's atmosphere included a new yield function of isotropically precipitating monoenergetic electrons and ionisation via bremsstrahlung (braking) radiation. Look-up tables with ion production/yield function for isotropically precipitating monoenergetic electrons (30 keV to 5 MeV) can be used for the computation of ionisation rates and for accurate quantification of atmospheric parameters during energetic electron precipitation in atmospheric and chemistry–climate models.

Xu et al. [157] simulated, from first principles, the interaction of monoenergetic beams of precipitating electrons with the atmosphere, with particular emphasis on the process of bremsstrahlung radiation and its resultant production of ionisation. The pitch angle dependence of the ionisation rate profile was quantified: the altitude of peak ionisation rate depends on the pitch angle, but only by a few km, as is evident from Figure 11. They demonstrated that the bremsstrahlung photons lead to ionisation (at altitudes significantly lower than is produced by direct impact ionisation) in the stratosphere and down to ~ 20 km for 1 MeV precipitating electrons. Chemical modelling suggests that the long-term chemical effects in the atmosphere due to such bremsstrahlung-induced ionisation are likely to be insignificant.

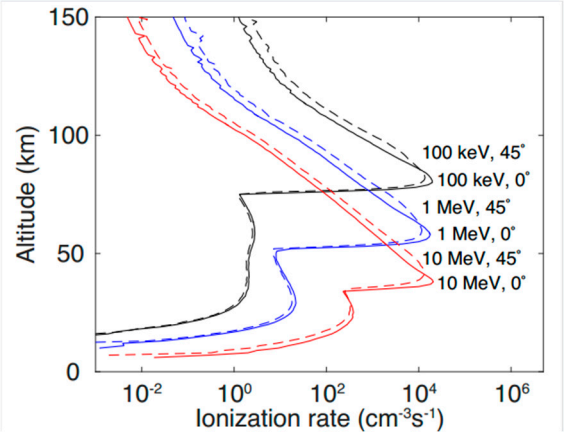


Figure 11. Modelled ionisation profiles due to precipitating electrons with energies of 100 keV, 1 MeV and 10 MeV, with pitch angles of 45° (dashed lines) and 0°, exactly down geomagnetic field lines (solid lines). From Xu et al. [157].

Xu et al. [158] noted that the accurate specification of ionisation production by energetic electron precipitation is critical for atmospheric chemistry models. Recent model-observation comparison studies have highlighted the importance of considering precipitation fluxes for the full range of electron energies and pitch angles. They characterised and tabulated the atmospheric ionisation response to beams of monoenergetic electrons with different pitch angles and energies between ~3 keV and ~33 MeV. For exponential energy distributions, and isotropic and sine pitch angle distributions, the error in peak ionisation altitude was found to be ~1 km, with a mean error of 2.7% in peak ionisation rate and 1.9% in total ionisation.

With reference to Figure 1 of [51], presented here as Figure 3, Xu et al. [51] have considered Relativistic Electron Precipitation (REP, between 100 keV and 10 MeV) from the Van Allen radiation belts, which can induce radiation down to the lower stratosphere and even the troposphere. They estimated the radiation dose for a precipitation flux, in agreement with values presented in Section 4, of 10^4 electrons cm^{-2} s^{-1}, considering their spectrum and pitch angle distribution. They found that the LEP events—some thousands of lightning flashes in an hour—in intense magnetic storms could drive concentration changes of NO_x (by ~156%), HO_x (by ~ 66%) and O_x (by −5%) at 75–85 km altitude lasting for hours. Sanchez et al. [159] compared calculated D-region electron densities produced by Van Allen Probes chorus-associated energetic electron precipitation with profiles derived from incoherent scatter radar observations at L ~ 5.2. Sometimes they found very good agreement, and at other times not such good agreement; this indicates that the precipitation is either rather localised or rather intermittent, or both.

Pettit et al. [160] considered that energetic electron precipitation is a frequent, yet often ignored, middle- to high-latitude forcing that can have dramatic effects on the middle and upper atmosphere. Although several electron precipitation datasets have been developed recently, their validation has been difficult due to the lack of independent observations of energetic electron fluxes. Additionally, the limited number of satellites making measurements of global magnetospheric wave activity along with the resulting electron precipitation restricts the ability to capture the drivers of energetic electron precipitation simultaneously with the precipitation. Pettit et al. [160] concluded that, to improve current modelling efforts, new observations of atmospheric composition are required.

Salminen et al. [161] studied the Earth's atmosphere influenced by energetic electron precipitation (EEP) into the high-latitude mesosphere and lower thermosphere (MLT region). EEP forms odd nitrogen (NO_x) and hydrogen oxides (HO_x) which destroy ozone.

During winter EEP, NO_x descends to the stratosphere, establishing the indirect EEP effect. Several studies have found that EEP is related to changes in temperature and winds in the northern winter stratosphere. One of the most prominent effects of EEP is the influence on the northern polar vortex, a westerly wind system surrounding the winter pole in the middle atmosphere. They studied EEP effects on chemical and dynamical properties of the stratosphere and mesosphere in the northern hemisphere by using EOS Aura satellite measurements of atmospheric properties and POES satellite measurements of precipitating electrons [161]. They confirmed earlier results showing that EEP decreases ozone concentrations, affects the temperature in the polar middle atmosphere and strengthens the stratospheric polar vortex. They also showed that EEP weakens the mesospheric polar vortex in late winter, partly due to changes in the propagation and convergence of planetary waves.

Frolov and Troitsky [162] reported on experiments at the SURA mid-latitude heating facility that modified the ionospheric F_2 layer by powerful HF ordinary-mode (O-mode) radio waves and gave rise to the artificial injection of energetic electrons from the Earth's radiation belt into the atmosphere. The spectral, energy, and spatial characteristics of such an injection were presented. Energetic electrons excite the atoms and molecules of the atmosphere, followed by the transition of the excited atoms and molecules to lower energy states, accompanied by the radiation of microwave electromagnetic emissions. The injection of energetic electrons generates secondary turbulence, the effect of which manifests itself at ionospheric and mesospheric heights both near the heating facility and to distances >1000 km. Disturbances to the topside ionospheric plasma were recorded by the Chinese satellite CSES (ZH-1) both above the SURA facility and in the geomagnetically conjugate region [163]. The conditions for generating VLF radio waves due to the nonlinear demodulation of a powerful radio wave were reported by Frolov et al. [163].

Following on from [148], Dong et al. [164] discussed energetic electron precipitation (EEP) from the Earth's radiation belts that can ionise neutral molecules in the D-region ionosphere (60 to 90 km altitude), significantly influencing the electrical conductivity and chemical species therein. However, due to the limited resolution of space-borne instruments, the energy and fluxes of electrons that precipitate into the atmosphere are hard to measure. They used the wave and charged particle data measured by the Electric Field Detector (EFD) and High-Energy Particle Detector (HEPP) on board the China Seismo-Electromagnetic Satellite (CSES-01) during nighttime conditions between 2019 and 2021 [164]. Using measurements of extremely-low-frequency (ELF) waves (see [165]), they derived the reflection height of the D-region ionosphere, which were consistent with the electron and X-ray measurements of the CSES. Their results showed that the influence of EEP on the two hemispheres at $4 < L < 7$ is asymmetric: the ionospheric reflection height of ELF radio waves in the northern hemisphere is in general lowered by 2.5 km, while that in the southern hemisphere is lowered by 1.5 km, both of which are consistent with first-principles chemical simulations. They also found that the decrease in reflection height exhibits a strong seasonal variation, which appears to be stronger during winter and weaker during summer; this is probably related to the variation in the background ionospheric electron density [165]. Katoh et al. [166] also made a detailed study of the ionisation profiles produced by precipitating energetic electrons.

Analysing the Trimpi signatures at four Antarctic sites of subionospheric VLF signals received from four transmitters (NAA, NSS, NLK, and NPM), Clilverd et al. [167] found that the precipitation patches were large (~1500 km east–west and ~600 km north–south). Some 38% of the Trimpi events were associated with strong lightning flashes in the eastern USA. They suggested that non-ducted whistlers were the cause of the large precipitation regions at ~84 km altitude [166]. Kolarski et al. [168] recently discussed such precipitation patches, calling them localised ionisation enhancements (LIEs). Their case study focused

on Lightning-induced Electron Precipitation (LEP), analysing amplitude and phase variations in VLF signals recorded in Belgrade, Serbia, from worldwide transmitters, and modelling the reflection heights and sharpness of the ionosphere. They showed that LIEs are typically < 500 km by 1000 km in size [168]. Clilverd et al. [169] concluded that VLF communication transmitter signals ($18 < f < 25$ kHz) drive electron precipitation primarily from the inner radiation belt ($1.3 < L < 2.5$) through a combination of non-ducted propagation at $1.3 < L < 1.5$, but predominantly through ducted wave propagation at $1.5 < L < 2.5$, until the half-electron gyro frequency limit for ducted waves is reached.

Finally, in the context of climate change, it is important to consider whether such patches of increased ionisation at ~85 km altitude due to LEP could change the pattern of the electric fields down to thunderstorm altitudes. One way of doing that was presented by Hale [170] in a contribution to Scientific Correspondence in Nature; he suggested that the capacitive coupling of "several Coulombs" due to energetic electron precipitation from ionosphere to thundercloud could create a larger cloud-to-ground electric field, which might then cause an increase in the rate of lightning discharges locally. Is it likely that several Coulombs could be created in the ionosphere in this way? Using the numerical values presented in Section 4, that in 2 s the energetic electron flux is $2.4\ 10^4$ cm^{-2}, the electric charge thus created in the D-region would be $1.6\ 10^{-19}\ 2.4\ 10^4$ C $cm^{-2} \sim 4\ 10^{-15}$ C cm^{-2}. Over a radius of 25 km in the ionosphere, the electric charge would be $4\ 10^{-15}\ \pi\ (2.5\ 10^{1+3+2})^2 \sim 80\ 10^{-15+12}$ C ~ 0.1 C. This is rather less than is required by Hale [170]; Hale and Baginski [171] also considered this issue.

13. Conclusions

The conclusions of this review are as follows:

1. Whistlers physically couple the troposphere, the Van Allen radiation belts and the lower ionosphere via the phenomenon of Lightning-induced Electron Precipitation (LEP). Lightning-generated whistlers propagating along geomagnetic field-aligned ducts of enhanced plasma density, N_{eq}, interact in the equatorial plane with n = 1 cyclotron resonant radiation belt electrons travelling in the opposite direction, leading to their pitch angle scattering (a linear mechanism) into the bounce loss cone and precipitation into the upper atmosphere. This is the major loss mechanism for trapped energetic electrons (with energy W ~ 30–300 keV) at middle latitudes, $1.8 < L < 3.7$. In the equatorial plane, the whistler field strength is typically a few pT; being stronger at night, it can reach ~100 pT. A LEP event causes increased ionisation at ~80–85 km altitude, which lasts for a short time.
2. The variation of $W_{\|}N_{eq}$ with L-shell for the n = 1 resonance at different frequencies f for two modelled plasmaspheric profiles $N_{eq}(L)$ is discussed.
3. The energy flux into the upper atmosphere due to a single LEP event, of 2 s duration, is ~10^{-2} erg cm^{-2}, or 10^{-5} J m^{-2}. Over an area of $2\ 10^9$ m^2, the energy input is $2\ 10^4$ J. This is a significant result.
4. The fluxes of energetic electrons arising from the LEP (ducted) process that are required to produce extra ionisation at ~80 km altitude and above to modify VLF propagation in the Earth–ionosphere waveguide are estimated to be ~10^{-3} to 10^{-2} erg cm^{-2} s^{-1}. Non-ducted magnetospherically reflecting whistlers also contribute to energetic electron precipitation at $1.5 < L < 5$.
5. Eastward-drifting LEP energetic electrons at $L < 3$ are in the drift loss cone; they precipitate in the South Atlantic Magnetic Anomaly, causing significant losses from the radiation belts.
6. LEP losses are more significant than all other inner radiation belt loss processes for electrons with energies between 50 and 150 keV, at $2.0 < L < 2.4$. The upper energy

limit of the LEP process decreases from ~225 keV at L = 2 with increasing L-shell. This is an important process for non-relativistic electrons.

7. The variability in LEP occurrence is due to geomagnetic storm-associated increases in the energetic electron population in the slot region between the inner and outer radiation belts (L ~ 2.5).
8. The region with the highest LEP rate is at 2.0 < L < 3.7 over the east coast of the USA; LEPs also occur over Central Europe and Russia, and their geomagnetic conjugate regions. LEPs are more prevalent at night because the ionospheric absorption of upgoing whistlers is lower than during the day. The average precipitating electron flux at 100 keV due to ducted lightning is ~20 cm^{-2} s^{-1} sr^{-1} keV^{-1}. For a LEP event lasting 2 s, the downward flux of electrons of all energies is ~ 4 10^4 cm^{-2}, with the energy flux into the ionosphere being ~10^{-5} J m^{-2}. Considering an area of 25 km radius below the whistler duct, the charge input to the ionosphere due to one LEP event is ~0.1 C. These three numerical values derived from satellite observations are important new estimates of these quantities.
9. The mainly daytime phenomenon of broadband hiss is more important than LEP in causing losses from the radiation belts at L > 2.5. During magnetically active periods, losses due to plasmaspheric hiss can occur on a time scale of a day or less for electrons of 200 keV < W < 1 MeV, at 3.5 < L < 4.0. In the equatorial plane, hiss signals are typically 10 pT. Strong plasmaspheric hiss at ~1 kHz at 5 < L < 6 causes strong scattering of electrons of tens of keV, leading to a substantial filling of the loss cone.
10. Hiss waves (0.1 < f < 0.5 kHz) in plasmaspheric plumes cause daytime energetic electron precipitation at L > 4. The characteristic energy decreases from ~ 100 keV at L = 3 to ~20 keV at L = 6. In the equatorial plane, the typical field strength of plume hiss is 40 pT.
11. Chorus (rapidly rising tones with frequencies of 0.5 < f < 2.5 kHz) and microbursts of energetic electron precipitation are associated phenomena with time scales <1 s which occur, mainly during the morning hours, at 4 < L < 7; in the equatorial plane, the observed field strength of chorus is ~50 pT.
12. The gyro resonant interactions of energetic electrons with whistler-mode chorus waves play a direct and crucial role in the acceleration and loss of radiation belt electrons from some tens of keV to ~1 MeV. That this is a non-linear cyclotron resonance mechanism is an important conclusion.
13. Spacecraft observations show that there is sometimes a gap in the dynamic spectrum of chorus, at 0.5 $f_{B,e\ eq}$, half the equatorial electron gyro frequency. This leads to the nomenclature of lower-band chorus (<0.5 $f_{B,e\ eq}$) and upper-band chorus (>0.5 $f_{B,e\ eq}$). In the equatorial plane, the field strength of computer-simulated lower-band chorus is typically ~100 pT.
14. Particularly at night, when ionospheric absorption is lower than during the day, the ducted signals from ground-based VLF (15–30 kHz) radio transmitters interact gyro resonantly (n = 1) with energetic electrons near the equatorial plane of the magnetosphere to modify their pitch angles and precipitate them into the upper atmosphere. In the equatorial plane, the typical field strength of a VLF radio transmitter is a few pT.
15. The powerful VLF (19.8 kHz) transmitter NWC in Australia causes enhancements of ~100 to 600 keV drift loss cone electron fluxes at 1.4 < L < 1.7 and is a significant loss mechanism for inner belt electrons. In the equatorial plane at L ~ 1.7, its field strength can reach ~10 pT or even more. The maximum energy flux of precipitating electrons of > 100 keV caused by NWC was computed to be 10^{-5} erg cm^{-2} s^{-1} at L ~ 2.1.
16. The fluxes of ~200 keV electrons at L ~ 2.5 east of the NPM transmitter operating at night are ~10^2 cm^{-2} s^{-1} sr^{-1} keV^{-1}; they are comparable with the precipitating fluxes

due to LEPs. The typical field strength of this transmitter signal at L ~ 1.2 is up to 2 pT.

17. Theoretical studies indicate that VLF transmitters decrease trapped electron lifetimes by one to two orders of magnitude for 0.4 to 1 MeV electrons at L = 1.5, for 30 to 300 keV electrons at L = 2.0, and for 2 to 50 keV electrons at L = 2.
18. The global maps of LEP occurrence (Figures 4–6 and 8) agree rather well with each other, with dominant LEP regions over the USA, Central Europe, near New Zealand and near their geomagnetically conjugate regions. Coincidentally, there is some similarity between them and a global map showing regions where strong VLF transmitter signals are expected (Figure 9); this shows where geomagnetically conjugate transmitter-induced n = −1 gyro resonance precipitation may also occur. This similarity means that it will be difficult to distinguish between these two different precipitation mechanisms when interpreting satellite observations of energetic electrons.
19. LEP is a major mechanism responsible for the formation of the slot in the Earth's radiation belts, with energetic electron precipitation due to ducted VLF radio transmitter signals also playing an important role. This is a most important conclusion.
20. VLF transmitter waves play a critical role in energetic electron scattering and precipitation from the inner radiation belt; they constitute an example of man-made modification of the upper atmosphere environment. "Wisp" precipitation events exhibit dispersive energy versus L-shell spectra due to the evolution of electron cyclotron resonance conditions with almost monochromatic VLF transmitter waves.
21. Optical observations were made at 4278 Å (arising from the excited ionised nitrogen molecule) near a powerful (~150 kW) VLF transmitter in Norway, operating at 16.4 kHz. Approximately 2.5 s after the transmitter was turned on, a sudden increase in the intensity of the optical emissions was detected and interpreted as being caused by a burst of electron precipitation lasting ~0.5 s, due to gyro resonant wave–particle interactions between the transmitted wave causing scattering of the magnetospheric energetic electron population.
22. It is not yet known whether the VLF radio emissions triggered by PLHR cause energetic electron precipitation.
23. The effects of energetic electron precipitation on the upper atmosphere are to increase the ionisation in the D-region and E-region of the ionosphere (i.e., above 80 km) by collision with atmospheric atoms and molecules.
24. Precipitating energetic electrons cause increased ionisation in the atmosphere at altitudes below 80 km via bremsstrahlung radiation. This changes the chemistry of the upper stratosphere (~50 km), mesosphere and lower thermosphere (up to ~ 130 km) by altering the nitrogen and hydrogen oxide concentrations.

Tables 1 and 2 provide a summary of the main numerical results obtained in this paper.

Table 1. Summary of the main wave–particle interaction mechanisms of energetic electron loss from the Earth's magnetosphere by precipitation into the upper atmosphere at different latitudes and for different L-shell ranges.

L-Shell Range	Main Mechanism Causing Loss of Radiation Belt Electrons, >40 keV Up to ~1 MeV	Frequency Range	Approximate Percentage of Earth's Surface Area
1.0 < L < 1.7	Coulomb collisions	-	61%
	VLF transmitters	15–30 kHz	

1.8 < L < 2.5	VLF transmitters	15–30 kHz	
1.8 < L < 3.7	Lightning-induced electron precipitation	0.2–10 kHz	19%
2.5 < L < 3.7	Plasmaspheric hiss	0.1–2 kHz	
3.8 < L < 7	Plume hiss	0.1–0.5 kHz	13%
	Chorus with microbursts	0.5–4 kHz	
L > 7	Auroral and polar cap processes	-	7%

Note that the slot between the inner and outer radiation belts is at L ~ 2.5; the plasmapause, on average, is at L ~ 4.5. Note also that the area of the Earth's surface from the equator to 30° latitude is 50% and from there to the pole is also 50%; from the equator to 45° latitude it is ~71% and from there to the pole ~29%.

Table 2. Summary of the VLF signal types, their frequency ranges, and the predominant range of L-shells for cyclotron resonance interactions with electrons of different energies, which are precipitated into the upper atmosphere, causing maximum ionisation rates at different heights. The first number in each column gives the corresponding values, and so do the second numbers.

Type of Signal	Frequency Range, kHz	L-Shell Range	Energy of Precipitated Electrons, keV	Height of Maximum Ionisation Rate, km
Whistler (n = 1)	1–8	1.8–2.5	300–30	80–100
Whistler (n = −1)	2–4	2	1400	50 (25, bremsstrahlung)
Plasmaspheric hiss	0.1–2	3–4.5	1000–200	60–85
Plume hiss	0.1–0.5	4–6	100–30	90–100
Lower band chorus	0.5–4	4.5–7	1000–30	60–100
VLF transmitters	15–30	1.3–2.5	1000–30	60–100
Siple transmitter	2–7	4.2	7–0.1	110–160

Funding: The author received no funds for this study.

Institutional Review Board Statement: Not applicable.

Informed Consent Statement: Not applicable.

Data Availability Statement: No new data were created or analyzed in this study. Data sharing is not applicable to this article.

Acknowledgments: I am very grateful to Martin Füllekrug, of the University of Bath, and to Google and Google Scholar for assistance with finding references. I thank David Nunn, of Southampton University, and Yoshiharu Omura, of Kyoto University, for valuable discussions. I am grateful to all the authors who granted me permission to reproduce figures already published in their papers, and for their kind messages. I also thank William Brown, of the British Geological Survey (BGS) Geomagnetism Unit in Edinburgh, for producing the maps shown as Figures A1 and A2. The map of the total intensity of the field is for the 14th IGRF [172], and I thank Ciarán Beggan, Head of Geomagnetism, for allowing me to use this. The L-shell plotted is $(R_E + h_{apex})/R_E$, where the radius of the Earth $R_E = 6371.2$ km, and h_{apex} is the greatest height above R_E reached by a given field line, using the IGRF. The apex coordinate system is explained by Emmert et al. [173]. The software used to generate Figure A2 was apexpy v2.1.0 https://doi.org/10.5281/zenodo.14610316, accessed on 1 June 2026. Finally, I thank the three reviewers whose comments and suggestions have helped me to clarify the messages of this paper.

Conflicts of Interest: The author declares no conflicts of interest. CAESAR Consultancy had no role in the design of the study; in the collection, analyses, or interpretation of data; in the writing of the manuscript; or in the decision to publish the results.

Appendix A

Parameters Specifying the Geomagnetic Field

The discussion in Section 4 is concerned with energetic electrons trapped in the geomagnetic field **B (**Defined in Section 1**)**, which, in the magnetosphere, resembles that of a dipole field. In a dipolar field, the magnitude of the magnetic field in the equatorial plane decreases as r^{-3}, where r is the radial distance from the centre of the Earth. However, at the Earth's surface and in the ionosphere above it, the geomagnetic field differs quite considerably from a dipole field, with the South Atlantic Geomagnetic Anomaly being the most obvious departure. So that the reader can readily appreciate this fact, Figure A1 presents a model of the total intensity of the geomagnetic field at 100 km altitude, where precipitating energetic electrons cause extra ionisation [51], for 1 January 2025, the 14th generation of the International Geomagnetic Reference Field (IGRF), obtained from [172].

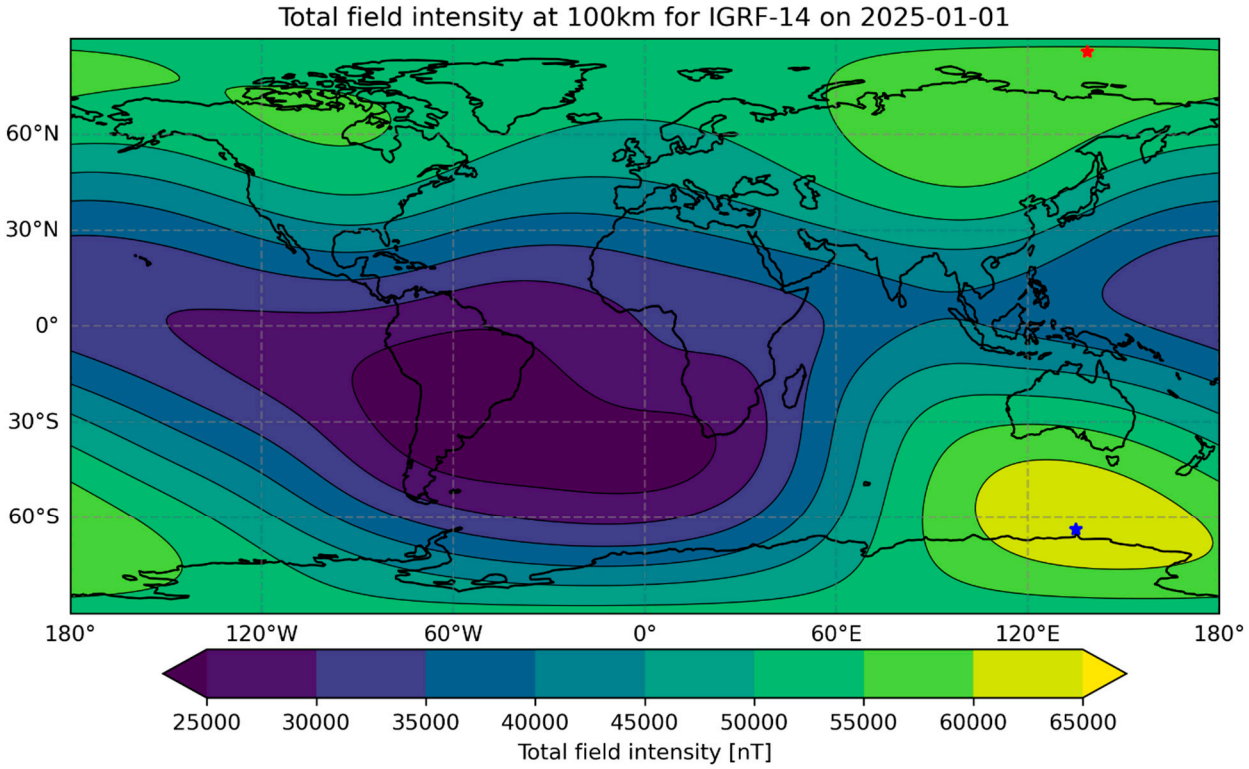


Figure A1. Map of the total magnetic field **B** at 100 km altitude for epoch 1 January 2025 [172]. Values <25,000 nT shown in dark purple correspond to the region of the South Atlantic Geomagnetic Anomaly; the north magnetic dip pole is shown by a red star and the south magnetic dip pole by a blue star.

The L-values, computed using Emmert et al. [173], specify a geomagnetic field line; they were introduced by McIlwain [174]. They are based upon the three adiabatic constants of motion of a charged particle in a magnetic field, here the geomagnetic field. This is explained in a paper which specifies the AE9/AP9/SPM model of the fluxes of energetic particles trapped in the Earth's magnetosphere [175]. The L-value is approximately the distance at which a geomagnetic field line crosses the equatorial plane, measured in Earth radii. Figure A2 is a global map showing the L-values, or L-shells [176], at an altitude of 100 km for the 14th IGRF [172].

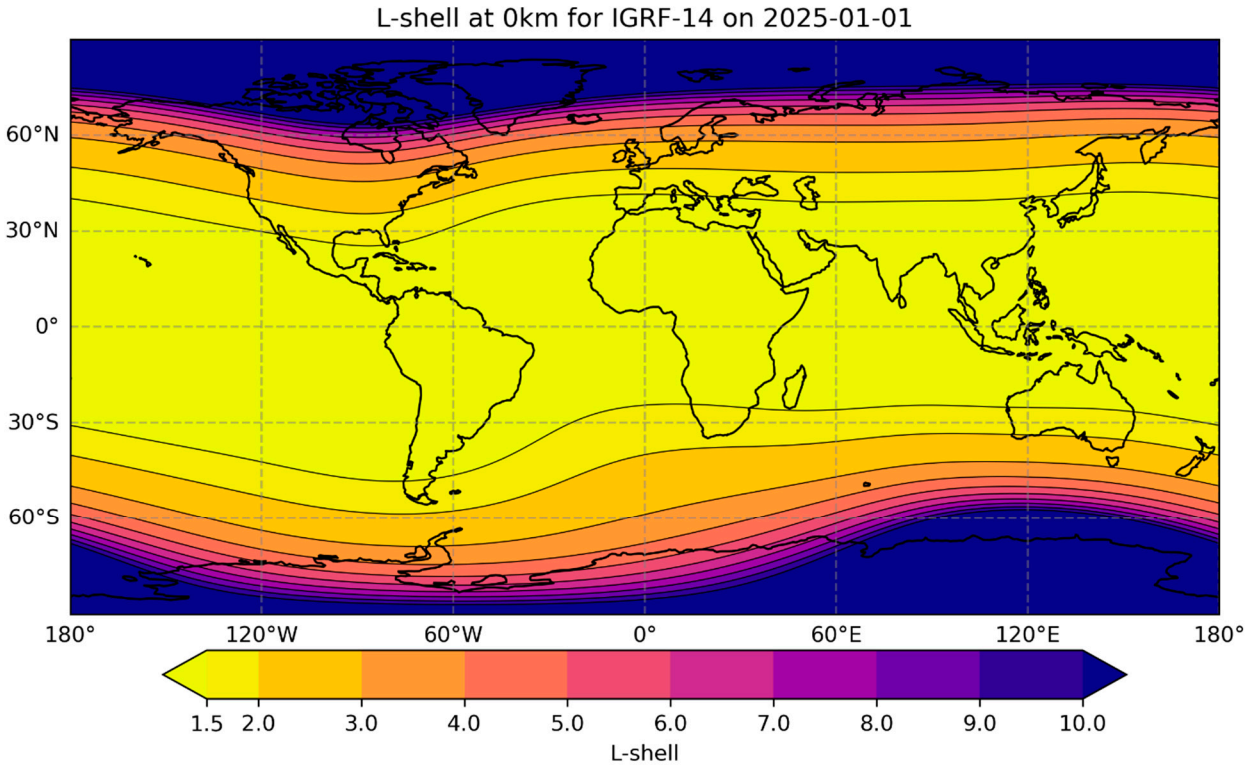


Figure A2. Map showing L-values at the Earth's surface for geomagnetic field lines of the 14th IGRF [172], at L = 1.5, 2, 3, 4, 5, 6, 7, 8, 9 and 10 [176]. The electron slot between the inner and outer Van Allen belts is at L ~ 2.5, the plasmapause is typically at L ~ 4.5, and the auroral oval, or the auroral zone, is generally at L ~ 6 to 7. All these field lines are "closed", dipolar-like field lines linking the northern and southern hemispheres. At L > 8 and at ~20 h < MLT < 04 h, geomagnetic field lines are "open" down the Earth's magnetotail; at other times, these large L-value field lines are connected to the magnetopause. As geomagnetic activity increases from quiet to active, each of these L-value numbers decreases somewhat.

The difference between the true McIlwain L-value [174] and the radial distance to where the magnetic field line of interest crosses the equator is typically 0.02 R_E at L = 2 and 0.08 R_E at L = 4. This difference does not cause a significant problem when locating satellite observations in relation to magnetospheric features.

The difference between the true McIlwain L-value and the Roederer parameter R* at L = 2 is zero at magnetically quiet times and ~ 0.1 R_E at active times [177]. This is not a serious error. However, at L = 4, the difference is ~0.2 R_E at quiet times, which may be considered acceptable. At active times at L = 4, the typical error is ~0.5 R_E; it is largest at ~18 h MLT [177]. This error complicates the interpretations of observations made aboard satellites in the magnetosphere.

Emmert et al. [173] consider that, for the invariant latitude, λ, of a particular geomagnetic field line, given by $\cos^2 \lambda = 1/L$, the typical error is ~0.1°. For L = 2, the L-shell error is therefore 0.007, and for L = 4 it is 0.024. These values are negligible compared with other typical errors.

References

1. Dungey, J.W. Loss of Van Allen electrons due to whistlers. *Planet. Space Sci.* **1963**, *11*, 591–595. https://doi.org/10.1016/0032-0633(63)90166-1.
2. Cornwall, J.M. Scattering of energetic trapped electrons by very-low-frequency waves. *J. Geophys. Res.* **1964**, *69*, 1251–1258. https://doi.org/10.1029/JZ069i007p01251.

3. Brice, N. Fundamentals of very low frequency emission generation mechanisms. *J. Geophys. Res.* **1964**, *69*, 4515–4522. https://doi.org/10.1029/JZ069i021p04515.
4. Liemohn, H.B. Cyclotron-resonance amplification of VLF and ULF whistlers. *J. Geophys. Res.* **1967**, *72*, 39–55. https://doi.org/10.1029/jz072i001p00039.
5. Tsurutani, B.T.; Lakhina, G.S. Some basic concepts of wave-particle interactions in collisionless plasmas. *Rev. Geophys.* **1997**, *35*, 491–501. https://doi.org/10.1029/97RG02200.
6. Tsurutani, B.T.; Zank, G.P.; Sterken, V.J.; Shibata, K.; Nagai, T.; Mannucci, A.J.; Malaspina, D.M.; Lakhina, G.S.; Kanekal, S.G.; Hosokawa, K.; et al. Space Plasma Physics: A Review. *IEEE Trans. Plasma Sci.* **2023**, *51*, 1595–1655. https://doi.org/10.1109/TPS.2022.3208906.
7. Kennel, C.F.; Petschek, H.E. Limit on stably trapped particle fluxes. *J. Geophys. Res.* **1966**, *71*, 1–28. https://doi.org/10.1029/JZ071i001p00001.
8. Rycroft, M.J. Enhanced energetic electron intensities at 100 km altitude and a whistler propagating through the plasmasphere. *Planet. Space Sci.* **1973**, *21*, 239–251. https://doi.org/10.1016/0032-0633(73)90009-3.
9. Rycroft, M.J. VLF Emissions in the Magnetosphere. *Radio Sci.* **1972**, *7*, 811–830. https://doi.org/10.1029/RS007i008p00811.
10. Rycroft, M.J. Gyroresonance interactions in the outer plasmasphere. *J. Atmos. Terr. Phys.* **1976**, *38*, 1211–1214. https://doi.org/10.1016/0021-9169(76)90053-2.
11. Helliwell, R.A.; Katsufrakis, J.P.; Trimpi, M.L. Whistler-induced amplitude perturbation in VLF propagation. *J. Geophys. Res.* **1973**, *78*, 4678–4688. https://doi.org/10.1029/JA078i022p04679.
12. Carpenter, D.L.; LaBelle, J.W. A study of whistlers correlated with bursts of electron precipitation near L = 2. *J. Geophys. Res.* **1982**, *87*, 4427–4434.
13. Doolittle, J.H.; Carpenter, D.L. Photometric evidence of electron precipitation induced by first hop whistlers. *Geophys. Res. Lett.* **1983**, *10*, 611–614. https://doi.org/10.1029/GL010i008p00611.
14. Vampola, A.L. Observations of VLF transmitter-induced depletions of inner zone electrons. *Geophys. Res. Lett.* **1983**, *10*, 619–622. https://doi.org/10.1029/GL010i008p00619.
15. Imhof, W.L.; Reagan, J.B.; Voss, H.D.; Gaines, E.E.; Datlowe, D.W.; Mobilia, J.; Helliwell, R.A.; Inan, U.S.; Katsufrakis, J.; Joiner, R.G. Direct observation of radiation belt electrons precipitated by the controlled injection of VLF signals from a ground-based transmitter. *Geophys. Res. Lett.* **1983**, *10*, 361–364. https://doi.org/10.1029/GL010i004p00361.
16. Voss, H.D.; Imhof, W.L.; Walt, M.; Mobilia, J.; Gaines, E.E.; Reagan, J.B.; Inan, U.S.; Helliwell, R.A.; Carpenter, D.L.; Katsufrakis, J.P.; et al. Lightning-induced electron precipitation. *Nature* **1984**, *312*, 740–742.
17. Rycroft, M.J. Interaction between whistlers and radiation belt electrons. *Nature* **1984**, *312*, 698.
18. Carpenter, D.L.; Inan, U.S.; Trimpi, M.L.; Helliwell, R.A.; Katsufrakis, J.P. Perturbations of subionospheric LF and MF signals due to whistler-induced electron precipitation bursts. *J. Geophys. Res.* **1984**, *89*, 9857–9862. https://doi.org/10.1029/JA089iA11p09857.
19. Inan, U.S.; Carpenter, D.L.; Helliwell, R.A.; Katsufrakis, J.P. Subionospheric VLF/LF phase perturbations produced by lightning-whistler induced particle precipitation. *J. Geophys. Res.* **1985**, *90*, 7457–7469. https://doi.org/10.1029/JA090iA08p07457.
20. Chang, H.C.; Inan, U.S. Lightning-induced electron precipitation from the magnetosphere. *J. Geophys. Res.* **1985**, *90*, 1531–1541. https://doi.org/10.1029/JA090iA02p01531.
21. Imhof, W.L.; Voss, H.D.; Walt, M.; Gaines, E.E.; Mobilia, J.; Datlowe, D.W.; Reagan, J.B. Slot region electron precipitation by lightning, VLF chorus, and plasmaspheric hiss. *J. Geophys. Res.* **1986**, *91*, 8883–8894. https://doi.org/10.1029/JA091iA08p08883.
22. Goldberg, R.A.; Barcus, J.R.; Hale, L.C.; Curtis, S.A. Direct observation of magnetospheric electron precipitation stimulated by lightning. *J. Atmos. Terr. Phys.* **1986**, *48*, 293–299. https://doi.org/10.1016/0021-9169(86)90105-4.
23. Inan, U.S.; Wolf, T.G.; Carpenter, D.L. Geographic distribution of lightning-induced electron precipitation observed as VLF/LF perturbation events. *J. Geophys. Res.* **1988**, *93*, 9841–9853. https://doi.org/10.1029/JA093iA09p09841.
24. Rycroft, M.J. Interactions between whistler-mode waves and energetic electrons in the coupled system formed by the magnetosphere, ionosphere and atmosphere. *J. Atmos. Terr. Phys.* **1991**, *53*, 849–858.
25. Dowden, R.L.; Adams, C.D.D.; Cotton, P.D. Use of VLF transmissions in the location and mapping of lightning-induced ionisation enhancements (LIEs). *J. Atmos. Terr. Phys.* **1992**, *54*, 1355–1373. https://doi.org/10.1016/0021-9169(92)90045-M.
26. Smith, A.J. Aspects of wave-particle interactions at mid-latitudes. *Adv. Space Res.* **1996**, *17*, 213–222.
27. Voss, H.D.; Walt, M.; Imhof, W.L.; Mobilia, J.; Inan, U.S. Satellite observations of lightning-induced electron precipitation. *J. Geophys. Res.* **1998**, *103*, 11725–11744.

28. Blake, J.B.; Inan, U.S.; Walt, M.; Bell, T.F.; Bortnik, J.; Chenette, D.L.; Christian, H.J. Lightning-induced energetic electron flux enhancements in the drift loss cone. *J. Geophys. Res.* **2001**, *106*, 29733–29744. https://doi.org/10.1029/2001JA000067.
29. Rodger, C.J.; Clilverd, M.A. Inner radiation belt electron lifetimes due to whistler-induced electron precipitation (WEP) driven losses. *Geophys. Res. Lett.* **2002**, *29*, 1924. https://doi.org/10.1029/2002GL015795.
30. Rodger, C.J.; Clilverd, M.A.; McCormick, R.J. Significance of lightning-generated whistlers to inner radiation belt electron lifetimes. *J. Geophys. Res.* **2003**, *108*, 1462. https://doi.org/10.1029/2003JA009906.
31. Clilverd, M.A.; Rodger, C.J.; Nunn, D. Radiation belt electron precipitation fluxes associated with lightning. *J. Geophys. Res.* **2004**, *109*, A12208. https://doi.org/10.1029/2004JA010644.
32. Rodger, C.J.; Clilverd, M.A.; Thomson, N.R.; Nunn, D.; Lichtenberger, J. Lightning driven inner radiation belt energy deposition into the atmosphere: Regional and global estimates. *Ann. Geophys.* **2005**, *23*, 3419–3430.
33. Rodger, C.J.; Clilverd, M.A.; Kavanagh, A.J.; Watt, C.E.J.; Verronen, P.T.; Raita, T. Contrasting the responses of three different ground-based instruments to energetic electron precipitation. *Radio Sci.* **2012**, *47*, RS2021. https://doi.org/10.1029/2011RS004971.
34. Peter, W.B.; Chevalier, M.; Inan, U.S. Subionospheric VLF Measurements of the Effects of Geomagnetic Storms on the Mid-Latitude D-Region. Stanford VLF Group Website. 2003. Available online: https://vlfstanford.ku.edu.tr/ (accessed on 9 July 2026).
35. Peter, W.B.; Chevalier, M.W.; Inan, U.S. Perturbations of midlatitude subionospheric VLF signals associated with lower ionospheric disturbances during major geomagnetic storms. *J. Geophys. Res.* **2006**, *111*, A03301. https://doi.org/10.1029/2005JA011346.
36. Bortnik, J.; Inan, U.S.; Bell, T.F. L dependence of energetic electron precipitation driven by magnetospherically reflecting whistler waves. *J. Geophys. Res.* **2002**, *107*, SMP 1-1–SMP 1-13. https://doi.org/10.1029/2001JA000303.
37. Bortnik, J.; Inan, U.S.; Bell, T.F. Temporal signatures of radiation belt electron precipitation induced by lightning-generated MR whistler waves: 2. Global signatures. *J. Geophys. Res.* **2006**, *111*, A02205. https://doi.org/10.1029/2005JA011398.
38. Inan, U.S.; Piddyachiy, D.; Peter, W.B.; Sauvaud, J.A.; Parrot, M. DEMETER satellite observations of lightning-induced electron precipitation. *Geophys. Res. Lett.* **2007**, *34*, L07103. https://doi.org/10.1029/2006GL029238.
39. Meredith, N.P.; Horne, R.B.; Glauert, S.A.; Anderson, R.R. Slot region electron loss timescales due to plasmaspheric hiss and lightning-generated whistlers. *J. Geophys. Res.* **2007**, *112*, A08214. https://doi.org/10.1029/2007JA012413.
40. Parrot, M.; Sauvaud, J.A.; Soula, S.; Pinc¸on, J.L.; van der Velde, O. Ionospheric density perturbations recorded by DEMETER above intense thunderstorms. *J. Geophys. Res. Space Phys.* **2013**, *118*, 5169–5176. https://doi.org/10.1002/jgra.50460.
41. Füllekrug, M.; Mareev, E.A.; Rycroft, M.J. *Sprites, Elves and Intense Lightning Discharges*; NATO Science Series II; Springer: Dordrecht, The Netherlands, 2006; p. 398, ISBN 9781402046292.
42. Pasko, V.P.; Inan, U.S.; Bell, T.F.; Taranenko, Y.N. Sprites produced by quasi-electrostatic heating and ionization in the lower ionosphere. *J. Geophys. Res.* **1997**, *102*, 4529–4561. https://doi.org/10.1029/96JA03528.
43. Gemelos, E.S.; Inan, U.S.; Walt, M.; Parrot, M.; Sauvaud, J.A. Seasonal dependence of energetic electron precipitation: Evidence for a global role of lightning. *Geophys. Res. Lett.* **2009**, *36*, L21107. https://doi.org/10.1029/2009GL040396.
44. Christian, H.J.; Blakeslee, R.J.; Boccippio, D.J.; Boeck, W.L.; Buechler, D.E.; Driscoll, K.T.; Goodman, S.J.; Hall, J.M.; Koshak, W.J.; Mach, D.M.; et al. Global frequency and distribution of lightning as observed from space by the Optical Transient Detector. *J. Geophys. Res.* **2003**, *108*, 4005. https://doi.org/10.1029/2002JD002347.
45. Rycroft, M.J. Interactions between whistler-mode signals and magnetospheric energetic electrons: An overview of some experimental observations and theoretical interpretations. *Indian J. Radio Space Phys.* **2011**, *40*, 241–252.
46. Trakhtengerts, V.Y.; Rycroft, M.J. *Whistler and Alfven Mode Cyclotron Masers in Space*; Cambridge University Press: Cambridge, UK, 2008.
47. Colman, J.J.; Starks, M.J. VLF wave intensity in the plasmasphere due to tropospheric lightning. *J. Geophys. Res. Space Phys.* **2013**, *118*, 4471–4482. https://doi.org/10.1002/jgra.50217.
48. Agapitov, O.V.; Artemyev, A.V.; Mourenas, D.; Kasahara, Y.; Krasnoselskikh, V. Inner belt and slot region electron lifetimes and energization rates based on AKEBONO statistics of whistler waves. *J. Geophys. Res. Space Phys.* **2014**, *119*, 2876–2893. https://doi.org/10.1002/2014JA019886.
49. Zheng, H.; Holzworth, R.H.; Brundell, J.B.; Jacobson, A.R.; Wygant, J.R.; Hospodarsky, G.B.; Mozer, F.S.; Bonnell, J. A statistical study of whistler waves observed by Van Allen Probes (RBSP) and lightning detected by WWLLN. *J. Geophys. Res. Space Phys.* **2016**, *121*, 2067–2079. https://doi.org/10.1002/2015JA022010.
50. Green, A.; Li, W.; Ma, Q.; Shen, X.C.; Bortnik, J.; Hospodarsky, G.B. Properties of lightning generated whistlers based on Van Allen Probes observations and their global effects on radiation belt electron loss. *Geophys. Res. Lett.* **2020**, *47*, e2020GL089584. https://doi.org/10.1029/2020GL089584.

51. Xu, W.; Marshall, R.A.; Kero, A.; Sousa, A. Chemical response of the upper atmosphere due to lightning induced electron precipitation. *J. Geophys. Res. Atmos.* **2021**, *126*, e2021JD034914. https://doi.org/10.1029/2021JD034914.
52. Rodger, C.J.; Enell, C.-F.; Turunen, E.; Clilverd, M.A.; Thomson, N.R.; Verronen, P.T. Lightning-driven inner radiation belt energy deposition into the atmosphere: Implications for ionisation-levels and neutral chemistry. *Ann. Geophys.* **2007**, *25*, 1745–1757. https://doi.org/10.5194/angeo-25-1745-2007.
53. Artemyev, A.V.; Demekhov, A.G.; Zhang, X.-J.; Angelopoulos, V.; Mourenas, D.; Fedorenko, Y.V.; Maninnen, J.; Tsai, E.; Wilkins, C.; Kasahara, S.; et al. Role of ducting in relativistic electron loss by whistler-mode wave scattering. *J. Geophys. Res. Space Phys.* **2021**, *126*, e2021JA029851. https://doi.org/10.1029/2021JA029851.
54. Pailoor, N.; Cohen, M.; Richardson, D.; Harid, V.; Gołkowski, M. Quantification of lightning-induced electron precipitation events on electron fluxes in the radiation belts. *J. Geophys. Res. Space Phys.* **2023**, *128*, e2022JA031153. https://doi.org/10.1029/2022JA031153.
55. Linzmayer, V.; Němec, F.; Santolik, O.; Kolmašova, I. Lightning-induced electron precipitation events observed at low altitudes. *J. Geophys. Res. Space Phys.* **2025**, *130*, e2024JA033639. https://doi.org/10.1029/2024JA033639.
56. Feinland, M.; Blum, L.W.; Marshall, R.A.; Gan, L.; Shumko, M.; Looper, M. Lightning-induced relativistic electron precipitation from the inner radiation belt. *Nat. Commun.* **2024**, *15*, 8721. https://doi.org/10.1038/s41467-024-53036-4.
57. Feinland, M.A.; Blum, L.W. Variable shapes observed in electron bouncing microburst packets. *Geophys. Res. Lett.* **2025**, *52*, e2024GL112587. https://doi.org/10.1029/2024GL112587.
58. Wang, Y.; Sun, Y.; Zong, Q.; Lu, G.; Gu, X.; Hu, Z.-J.; Li, B. First observation results of Macao Science Satellite 1 on lightning-induced electron precipitation. *Sci. China Earth Sci.* **2025**, *68*, 1–10. https://doi.org/10.1007/s11430-024-1411-x.
59. Zhao, H.-S.; Tan, Y.; Guo, H.-X.; Li, X.-B.; Liu, C.-Z.; Xu, W.; Zhang, S.-N.; Feng, H.; Xiong, S.-L.; Meng, B.; et al. Observations of lightning-induced electron precipitation by the Insight-HXMT satellite. *J. High Energy Astrophys.* **2026**, *53*, 100582. https://doi.org/10.1016/j.jheap.2026.100582.
60. Abel, B.; Thorne, R.M. Electron scattering loss in Earth's inner magnetosphere: 1. Dominant physical processes. *J. Geophys. Res.* **1998**, *103*, 2385–2396. https://doi.org/10.1029/97JA02919.
61. Abel, B.; Thorne, R.M. Electron scattering loss in Earth's inner magnetosphere: 2. Sensitivity to model parameters. *J. Geophys. Res.* **1998**, *103*, 2397–2407. https://doi.org/10.1029/97JA02920.
62. Lauben, D.S.; Inan, U.S.; Bell, T.F. Precipitation of radiation belt electrons induced by obliquely propagating lightning-generated whistlers. *J. Geophys. Res. Space Phys.* **2001**, *106*, 29745–29770. https://doi.org/10.1029/1999ja000155.
63. Trakhtengerts, V.Y.; Rycroft, M.J. Whistler–electron interactions in the magnetosphere: New results and novel approaches. *J. Atmos. Sol.-Terr. Phys.* **2000**, *62*, 1719–1733. https://doi.org/10.1016/S1364-6826(00)00122-X.
64. Trakhtengerts, V.Y.; Rycroft, M.J.; Nunn, D.; Demekhov, A.G. Cyclotron acceleration of radiation belt electrons by whistlers. *J. Geophys. Res.* **2003**, *108*, 1138. https://doi.org/10.1029/2002JA009559.
65. Demekov, A.G.; Trakhtengerts, V.Y.; Rycroft, M.J.; Nunn, D. Electron Acceleration in the Magnetosphere by Whistler-Mode Waves of Varying Frequency. *Geomagn. Aeron.* **2006**, *46*, 711–716.
66. Cotts, B.R.T.; Inan, U.S.; Lehtinen, N.G. Longitudinal dependence of lightning-induced electron precipitation. *J. Geophys. Res.* **2011**, *116*, A10206. https://doi.org/10.1029/2011JA016581.
67. Strangeways, H.J. Whistler leakage from narrow ducts. *J. Atmos. Terr. Phys.* **1986**, *48*, 455–462. https://doi.org/10.1016/0021-9169(86)90122-4.
68. Taylor, W.L.; Jean, A.G. Very-Low-Frequency Radiation Spectra of Lightning Discharges. *J. Res. Natl. Bur. Stand.-D. Radio Propag.* **1959**, *63D*, 199–204.
69. Hardman, R.; Clilverd, M.A.; Rodger, C.J.; Brundell, J.B.; Duthie, R.; Holzworth, R.H.; Mann, I.R.; Milling, D.K.; Macusova, E. A case study of electron precipitation fluxes due to plasmaspheric hiss. *J. Geophys. Res. Space Phys.* **2015**, *120*, 6736–6748. https://doi.org/10.1002/2015JA021429.
70. Li, W.; Shen, X.-C.; Ma, Q.; Capannolo, L.; Shi, R.; Redmon, R.J.; Rodriguez, J.V.; Reeves, G.D.; Kletzing, C.A.; Kurth, W.S.; et al. Quantification of energetic electron precipitation driven by plume whistler mode waves, Plasmaspheric hiss, and exohiss. *Geophys. Res. Lett.* **2019**, *46*, 3615–3624. https://doi.org/10.1029/2019GL082095.
71. Ma, Q.; Li, W.; Zhang, X.-J.; Bortnik, J.; Shen, X.-C.; Connor, H.K.; Boyd, A.J.; Kurth, W.S.; Hospodarsky, G.B.; Claudepierre, S.G.; et al. Global survey of electron precipitation due to hiss waves in the Earth's plasmasphere and plumes. *J. Geophys. Res. Space Phys.* **2021**, *126*, e2021JA029644. https://doi.org/10.1029/2021JA029644.

72. Sugo, S.; Kasahara, S.; Miyoshi, Y.; Katoh, Y.; Keika, K.; Yokota, S.; Hori, T.; Kasahara, Y.; Matsuda, S.; Matsuoka, A.; et al. Direct observations of energetic electron scattering and precipitation due to whistler-mode waves in the dayside high-density regions. *J. Geophys. Res. Space Phys.* **2023**, *128*, e2022JA030992. https://doi.org/10.1029/2022JA030992.
73. Oliven, M.N.; Gurnett, D.A. Microburst phenomena: 3. An association between microbursts and VLF chorus. *J. Geophys. Res.* **1968**, *73*, 2355–2362. https://doi.org/10.1029/JA073i007p02355.
74. Lorentzen, K.R.; Blake, J.B.; Inan, U.S.; Bortnik, J. Observations of relativistic electron microbursts in association with VLF chorus. *J. Geophys. Res.* **2001**, *106*, 6017–6027. https://doi.org/10.1029/2000JA003018.
75. Horne, R.B.; Thorne, R.M. Relativistic electron acceleration and precipitation during resonant interactions with whistler-mode chorus. *Geophys. Res. Lett.* **2003**, *30*, 1527. https://doi.org/10.1029/2003GL016973.
76. Horne, R.B.; Lam, M.M.; Green, J.C. Energetic electron precipitation from the outer radiation belt during geomagnetic storms. *Geophys. Res. Lett.* **2009**, *36*, L19104. https://doi.org/10.1029/2009GL040236.
77. Glauert, S.A.; Horne, R.B.; Meredith, N.P. Three-dimensional electron radiation belt simulations using the BAS Radiation Belt Model with new diffusion models for chorus, plasmaspheric hiss, and lightning-generated whistlers. *J. Geophys. Res. Space Phys.* **2014**, *119*, 268–289. https://doi.org/10.1002/2013JA019281.
78. Chen, L.; Breneman, A.W.; Xia, Z.; Zhang, X.-J. Modeling of bouncing electron microbursts induced by ducted chorus waves. *Geophys. Res. Lett.* **2020**, *47*, e2020GL089400. https://doi.org/10.1029/2020GL089400.
79. Aryan, H.; Bortnik, J.; Sibeck, D.G.; Hospodarsky, G. Global map of chorus wave sizes in the inner magnetosphere. *J. Geophys. Res. Space Phys.* **2022**, *127*, e2021JA029768. https://doi.org/10.1029/2021JA029768.
80. Chen, L.; Zhang, X.-J.; Artemyev, A.; Angelopoulos, V.; Tsai, E.; Wilkins, C.; Horne, R.B. Ducted chorus waves cause sub-relativistic and relativistic electron microbursts. *Geophys. Res. Lett.* **2022**, *49*, e2021GL097559. https://doi.org/10.1029/2021GL097559.
81. Chen, Z.; Xie, T.; Li, H.; Ouyang, Z.; Deng, X. The global variation of low ionosphere under action of energetic electron precipitation. *J. Geophys. Res. Space Phys.* **2023**, *128*, e2023JA031930. https://doi.org/10.1029/2023JA031930.
82. Ozeke, L.G.; Mann, I.R.; Olifer, L.; Chakraborty, S.; Pettit, J.M. The relationship between electron precipitation and the population of trapped electrons in LEO: New evidence supporting a natural limit to the flux of energetic electrons. *J. Geophys. Res. Space Phys.* **2024**, *129*, e2023JA031964. https://doi.org/10.1029/2023JA031964.
83. Chakraborty, S.; Mann, I.R.; Olifer, L.; Black, R.; Allanson, O.; Rae, I.J.; Ozeke, L.G.; Watt, C.E.J. Diagnosing the rapid loss of outer radiation belt electrons due to strong chorus-driven wave-particle interactions along an electron injection path. *J. Geophys. Res. Space Phys.* **2025**, *130*, e2025JA034045. https://doi.org/10.1029/2025JA034045.
84. Nunn, D.; Santolik, O.; Rycroft, M.; Trakhtengerts, V. On the numerical modelling of VLF chorus dynamical spectra. *Ann. Geophys.* **2009**, *27*, 2341–2359. https://doi.org/10.5194/angeo-27-2341-2009.
85. Gao, X.; Lu, Q.; Bortnik, J.; Li, W.; Chen, L.; Wang, S. Generation of multiband chorus by lower band cascade in the Earth's magnetosphere. *Geophys. Res. Lett.* **2016**, *43*, 2343–2350. https://doi.org/10.1002/2016GL068313.
86. Saito, S.; Miyoshi, Y.; Seki, K. Relativistic electron microbursts associated with whistler chorus rising tone elements: GEMSIS-RBW simulations. *J. Geophys. Res.* **2012**, *117*, A10206. https://doi.org/10.1029/2012JA018020.
87. Thorne, R.M. Radiation belt dynamics: The importance of wave-particle interactions. *Geophys. Res. Lett.* **2010**, *37*, L22107. https://doi.org/10.1029/2010GL044990.
88. Watt, C.E.J.; Rankin, R.; Degeling, A.W. Whistler mode wave growth and propagation in the prenoon magnetosphere. *J. Geophys. Res.* **2012**, *117*, A06205. https://doi.org/10.1029/2012JA017765.
89. Hsieh, Y.-K.; Omura, Y. Study of wave-particle interactions for whistler mode waves at oblique angles by utilizing the gyroaveraging method. *Radio Sci.* **2017**, *52*, 1268–1281. https://doi.org/10.1002/2017RS006245.
90. Hsieh, Y.-K.; Omura, Y. Precipitation rates of electrons interacting with lower-band chorus emissions in the inner magnetosphere. *J. Geophys. Res. Space Phys.* **2023**, *128*, e2023JA031307. https://doi.org/10.1029/2023JA031307.
91. Ebihara, Y.; Ikeda, T.; Omura, Y.; Tanaka, T.; Fok, M.-C. Nonlinear wave growth analysis of whistler-mode chorus generation regions based on coupled MHD and advection simulation of the inner magnetosphere. *J. Geophys. Res. Space Phys.* **2020**, *125*, e2019JA026951. https://doi.org/10.1029/2019JA026951.
92. Tao, X.; Zonca, F.; Chen, L. A "Trap-Release-Amplify" model of chorus waves. *J. Geophys. Res. Space Phys.* **2021**, *126*, e2021JA029585. https://doi.org/10.1029/2021JA029585.
93. Teng, S.C.; Tao, X. A review of frequency chirping mechanism of chorus waves in the Earth's magnetosphere. *Rev. Geophys. Planet. Phys.* **2022**, *53*, 567–579. (In Chinese) https://doi.org/10.19975/j.dqyxx.2022-032

94. Wu, Z.; Huang, H.; Wu, Y.; Tao, X.; Katoh, Y.; Wang, X. Connection between chorus wave amplitude and background magnetic field inhomogeneity: A parametric study. *Geophys. Res. Lett.* **2023**, *50*, e2023GL106397. https://doi.org/10.1029/2023GL106397.
95. Omura, Y. Nonlinear wave growth theory of whistler-mode chorus and hiss emissions in the magnetosphere. *Earth Planets Space* **2021**, *73*, 95. https://doi.org/10.1186/s40623-021-01380-w. Correction in *Earth Planets Space* **2021**, *73*, 121.
96. Wu, Z.; Teng, S.; Wu, Y.; Tao, X. Uncertainties in theoretical chorus chirping rates: A comparative analysis. *Geophys. Res. Lett.* **2025**, *52*, e2025GL115777. https://doi.org/10.1029/2025GL115777.
97. Hanzelka, M.; Santolík, O. Theories of Growth and Propagation of Parallel Whistler-Mode Chorus Emissions: A Review. *Surv. Geophys.* **2024**, *45*, 1–54. https://doi.org/10.1007/s10712-023-09792-x.
98. Watt, C.E.J.; Meredith, N.P.; Wong, J.; Murphy, K.R.; Rae, I.J.; Chakraborty, S.; Bentley, S.N.; Allanson, O.; Rodger, C.J. Occurrence rates and variability of whistler-mode waves in the plasma trough. *J. Geophys. Res. Space Phys.* **2025**, *130*, e2025JA034061. https://doi.org/10.1029/2025JA034061.
99. Kurita, S.; Miyoshi, Y.; Saito, S.; Kasahara, S.; Katoh, Y.; Matsuda, S.; Yokota, S.; Kasahara, Y.; Matsuoka, A.; Hori, T.; et al. Detection of ultrafast electron energization by whistler-mode chorus waves in the magnetosphere of Earth. *Sci. Rep.* **2025**, *15*, 992. https://doi.org/10.1038/s41598-024-80693-8.
100. Zhou, X.; Gao, X.; Wang, D.; Ma, J.; Lu, Q. Uncovering the generation mechanism of low-frequency chorus waves (<0.1 f_{ce_eq}) during active geomagnetic environments. *Geophys. Res. Lett.* **2026**, *53*, e2025GL119944. https://doi.org/10.1029/2025GL119944.
101. Chen, H.; Wang, X.; Li, X.; Chen, R.; Chen, L.; Omura, Y.; Hsieh, Y.; Lin, Y.; Adrian, M.L. Quantifying electron precipitation driven by chorus waves using self-consistent particle-in-cell simulations. *Geophys. Res. Lett.* **2025**, *52*, e2025GL116478. https://doi.org/10.1029/2025GL116478.
102. Chen, H.; Wang, X.; Chen, R.; Chen, L.; Omura, Y.; Miyoshi, Y.; Li, X.; Hsieh, Y. Simulation study of chorus wave modulation and associated electron precipitation. *Geophys. Res. Lett.* **2025**, *52*, e2025GL118562. https://doi.org/10.1029/2025GL118562.
103. Němec, F.; Santolík, O.; Pickett, J.S. On the north-south symmetry of the chorus source region: Conjugate observations by the Cluster spacecraft. *J. Geophys. Res. Space Phys.* **2026**, *131*, e2026JA035180. https://doi.org/10.1029/2026JA035180.
104. Grach, V.S.; Artemyev, A.V.; Demekhov, A.G.; Zhang, X.-J.; Angelopoulos, V. Electron precipitation driven by whistler-mode waves: Effects of wave-packet variability. *J. Geophys. Res. Space Phys.* **2026**, *131*, e2025JA034958. https://doi.org/10.1029/2025JA034958.
105. Saitoh, H.; Nishiura, M.; Kenmochi, N.; Yoshida, Z. Experimental study on chorus emission in an artificial magnetosphere. *Nat. Commun.* **2024**, *15*, 861. https://doi.org/10.1038/s41467-024-44977-x.
106. Bell, T.F.; Inan, U.S.; Kimura, I.; Matsumoto, H.; Mukai, T.; Hashimoto, K. EXOS-B/Siple Station VLF Wave-Particle Interaction Experiments: 2. Transmitter signals and associated emissions. *J. Geophys. Res.* **1983**, *88*, 295–309. https://doi.org/10.1029/JA088iA01p00295.
107. Inan, U.S.; Chang, H.C.; Helliwell, R.A.; Imhof, W.L.; Reagan, J.B.; Walt, M. Precipitation of radiation belt electrons by man-made waves: A comparison between theory and measurement. *J. Geophys. Res.* **1985**, *90*, 359–369. https://doi.org/10.1029/JA090iA01p00359.
108. Vampola, A.L. Electron precipitation in the vicinity of a VLF transmitter. *J. Geophys. Res.* **1987**, *92*, 4525–4532. https://doi.org/10.1029/JA092iA05p04525.
109. Vampola, A.L.; Adams, C.D. Outer zone electron precipitation produced by a VLF transmitter. *J. Geophys. Res.* **1988**, *93*, 1849–1858. https://doi.org/10.1029/JA093iA03p01849.
110. Rosenberg, T.J.; Wei, R.; Detrick, D.L.; Inan, U.S. Observations and modeling of wave-induced microburst electron precipitation. *J. Geophys. Res.* **1990**, *95*, 6467–6475. https://doi.org/10.1029/JA095iA05p06467.
111. Datlowe, D.W.; Imhof, W.L.; Fishman, G.J.; Finger, M.H. Local time and seasonal variations in the precipitation of energetic electrons from the inner radiation belt by cyclotron resonance with waves from powerful VLF transmitters. *Radio Sci.* **1995**, *30*, 47–55. https://doi.org/10.1029/94RS02592.
112. Kulkarni, P.; Inan, U.S.; Bell, T.F.; Bortnik, J. Precipitation signatures of ground-based VLF transmitters. *J. Geophys. Res.* **2008**, *113*, A07214. https://doi.org/10.1029/2007JA012569.
113. Meredith, N.P.; Horne, R.B.; Clilverd, M.A.; Ross, J.P.J. An investigation of VLF transmitter wave power in the inner radiation belt and slot region. *J. Geophys. Res. Space Phys.* **2019**, *124*, 5246–5259. https://doi.org/10.1029/2019JA026715.
114. Sauvaud, J.-A.; Maggiolo, R.; Jacquey, C.; Parrot, M.; Berthelier, J.-J.; Gamble, R.J.; Rodger, C.J. Radiation belt electron precipitation due to VLF transmitters: Satellite observations. *Geophys. Res. Lett.* **2008**, *35*, L09101. https://doi.org/10.1029/2008GL033194.

115. Gamble, R.J.; Rodger, C.J.; Clilverd, M.A.; Sauvaud, J.-A.; Thomson, N.R.; Stewart, S.L.; McCormick, R.J.; Parrot, M.; Berthelier, J.-J. Radiation belt electron precipitation by man-made VLF transmissions. *J. Geophys. Res.* **2008**, *113*, A10211. https://doi.org/10.1029/2008JA013369. Correction in *J. Geophys. Res.* **2009**, *114*, A05205. https://doi.org/10.1029/2009JA014304.
116. Zhang, Z.-X.; Li, X.-Q.; Wang, C.-Y.; Chen, L.-J. North west cape-induced electron precipitation and theoretical simulation. *Chin. Phys. B* **2016**, *25*, 119401. https://doi.org/10.1088/1674-1056/25/11/119401.
117. Graf, K.L.; Inan, U.S.; Piddyachiy, D.; Kulkarni, P.; Parrot, M.; Sauvaud, J.A. DEMETER observations of transmitter-induced precipitation of inner radiation belt electrons. *J. Geophys. Res.* **2009**, *114*, A07205. https://doi.org/10.1029/2008JA013949.
118. Li, J.D.; Spasojevic, M.; Harid, V.; Cohen, M.B.; Gołkowski, M.; Inan, U. Analysis of magnetospheric ELF/VLF wave amplification from the Siple Transmitter experiment. *J. Geophys. Res. Space Phys.* **2014**, *119*, 1837–1850. https://doi.org/10.1002/2013JA019513.
119. Omura, Y.; Nunn, D.; Matsumoto, H.; Rycroft, M.J. A review of observational, theoretical and numerical studies of VLF triggered emissions. *J. Atmos. Terr. Phys.* **1991**, *53*, 351–368.
120. Nunn, D. A self consistent theory of triggered VLF emissions. *Planet. Space Sci.* **1974**, *22*, 349–378.
121. Nunn, D.; Rycroft, M.; Trakhtengerts, V. A parametric study of the numerical simulations of triggered VLF emissions. *Ann. Geophys.* **2005**, *23*, 3655–3666.
122. Gołkowski, M.; Harid, V.; Hosseini, P. Review of Controlled Excitation of Non-linear Wave-Particle Interactions in the Magnetosphere. *Front. Astron. Space Sci.* **2019**, *6*, 2. https://doi.org/10.3389/fspas.2019.00002.
123. Bernhardt, P.A.; Siefring, C.L.; Briczinski, S.J.; McCarrick, M.; Michell, R.G. Large ionospheric disturbances produced by the HAARP HF facility. *Radio Sci.* **2016**, *51*, 1081–1093. https://doi.org/10.1002/2015RS005883.
124. Ma, Q.; Mourenas, D.; Li, W.; Artemyev, A.; Thorne, R.M. VLF waves from ground-based transmitters observed by the Van Allen Probes: Statistical model and effects on plasmaspheric electrons. *Geophys. Res. Lett.* **2017**, *44*, 6483–6491. https://doi.org/10.1002/2017GL073885.
125. Ross, J.P.J.; Meredith, N.P.; Glauert, S.A.; Horne, R.B.; Clilverd, M.A. Effects of VLF transmitter waves on the inner belt and slot region. *J. Geophys. Res. Space Phys.* **2019**, *124*, 5260–5277. https://doi.org/10.1029/2019JA026716.
126. Harid, V.; Gołkowski, M.; Bell, T.; Inan, U.S. Theoretical and numerical analysis of radiation belt electron precipitation by coherent whistler mode waves. *J. Geophys. Res. Space Phys.* **2014**, *119*, 4370–4388. https://doi.org/10.1002/2014JA019809.
127. Cunningham, G.S.; Botek, E.; Pierrard, V.; Cully, C.; Ripoll, J.-F. Observation of high-energy electrons precipitated by NWC transmitter from PROBA - V low - Earth orbit satellite. *Geophys. Res. Lett.* **2020**, *47*, e2020GL089077. https://doi.org/10.1029/2020GL089077.
128. Starks, M.J.; Lauben, D.S.; Albert, J.M.; Farrell, W.M.; Galkin, I.A.; Ginet, G.P.; Inan, U.S.; Johnston, W.R.; Linscott, I.R.; Sanchez, J.C.; et al. Characteristics of boomerang whistler-mode waves emitted from the DSX spacecraft. *J. Geophys. Res. Space Phys.* **2023**, *128*, e2023JA031300. https://doi.org/10.1029/2023JA031300.
129. McCollough, J.P.; Miyoshi, Y.; Ginet, G.P.; Johnston, W.R.; Su, Y.-J.; Starks, M.J.; Kasahara, Y.; Kojima, H.; Matsuda, S.; Shinohara, I.; et al. Space-to-space very low frequency radio transmission in the magnetosphere using the DSX and Arase satellites. *Earth Planets Space* **2022**, *74*, 64. https://doi.org/10.1186/s40623-022-01605-6.
130. Selesnick, R.S.; Albert, J.M.; Starks, M.J. Influence of a ground-based VLF radio transmitter on the inner electron radiation belt. *J. Geophys. Res. Space Phys.* **2013**, *118*, 628–635. https://doi.org/10.1002/jgra.50095.
131. Shen, Y.; Artemyev, A.V.; Ma, Q.; Zhang, X.-J.; Mourenas, D.; Tsai, E.; Wilkins, C.; Wu, J.; Angelopoulos, V. Inner belt wisp precipitation measured by ELFIN: Regimes of energetic electron scattering by VLF transmitter waves. *J. Geophys. Res. Space Phys.* **2022**, *127*, e2022JA030968. https://doi.org/10.1029/2022JA030968.
132. Shen, X.-C.; Li, W.; Capannolo, L.; Ma, Q.; Qin, M.; Artemyev, A.V.; Angelopoulos, V.; Zhang, X.; Huang, S. Modulation of energetic electron precipitation driven by three types of whistler mode waves. *Geophys. Res. Lett.* **2023**, *50*, e2022GL101682. https://doi.org/10.1029/2022GL101682.
133. Xiang, Z.; Li, X.; Baker, D.N.; Mei, Y.; O'Brien, D.; Hogan, B.; Zhao, H.; Brennan, D.; Ni, B.; Sarris, T.; et al. Earth-based transmitters trigger precipitation of inner radiation belt electrons: Unveiling observations and modeling results. *AGU Adv.* **2024**, *5*, e2024AV001354. https://doi.org/10.1029/2024AV001354.
134. Ripoll, J.F.; Claudepierre, S.G.; Ukhorskiy, A.Y.; Colpitts, C.; Li, X.; Fennell, J.; Crabtree, C. Particle Dynamics in the Earth's Radiation Belts: Review of Current Research and Open Questions. *J. Geophys. Res. Space Phys.* **2020**, *125*, e2019JA026735. https://doi.org/10.1029/2019JA026735.
135. Marshall, R.A. Effect of self-absorption on attenuation of lightning and transmitter signals in the lower ionosphere. *J. Geophys. Res. Space Phys.* **2014**, *119*, 4062–4076. https://doi.org/10.1002/2014JA019921.

136. Němec, F.; Santolík, O.; Hospodarsky, G.B.; Kurth, W.S. Alpha transmitter signals observed by the Van Allen Probes: Ducted versus nonducted propagation. *Geophys. Res. Lett.* **2022**, *49*, e2022GL098328. https://doi.org/10.1029/2022GL098328.
137. Gu, W.; Chen, L.; Xia, Z.; Horne, R.B. Direct evidence reveals transmitter signal propagation in the magnetosphere. *Geophys. Res. Lett.* **2021**, *48*, e2021GL093987. https://doi.org/10.1029/2021GL093987.
138. Denton, M.H.; Kosch, M.J.; Borovsky, J.E.; Clilverd, M.A.; Friedel, R.H.W.; Ulich, T. First optical observations of energetic electron precipitation at 4278 Å caused by a powerful VLF transmitter. *Geophys. Res. Lett.* **2014**, *41*, 2237–2242. https://doi.org/10.1002/2014GL059553.
139. Marshall, R.A.; Newsome, R.T.; Lehtinen, N.G.; Lavassar, N.; Inan, U.S. Optical signatures of radiation belt electron precipitation induced by ground-based VLF transmitters. *J. Geophys. Res.* **2010**, *115*, A08206. https://doi.org/10.1029/2010JA015394.
140. Chen, L.; Xia, Z.; Gu, W.; Horne, R.B. Ground transmitter waves in the magnetosphere and their role in electron scattering. *J. Geophys. Res. Space Phys.* **2026**, *131*, e2026JA035186. https://doi.org/10.1029/2026JA035186.
141. Xia, Z.; Chen, L.; Horne, R.B.; Miyoshi, Y.; Kasahara, Y.; Matsuda, S.; Shinbori, A.; Hori, T.; Shinohara, I. Evolution of NWC transmitter wave power distribution from the topside ionosphere into the inner magnetosphere. *Geophys. Res. Lett.* **2026**, *53*, e2026GL123087. https://doi.org/10.1029/2026GL123087.
142. Nunn, D.; Manninen, J.; Turunen, T.; Trakhtengerts, V.; Erokhin, N. On the nonlinear triggering of VLF emissions by power line harmonic radiation. *Ann. Geophys.* **1999**, *17*, 79–94.
143. Parrot, M.; Němec, F.; Santolík, O. Statistical analysis of VLF radio emissions triggered by power line harmonic radiation and observed by the low-altitude satellite DEMETER. *J. Geophys. Res. Space Phys.* **2014**, *119*, 5744–5754. https://doi.org/10.1002/2014JA020139.
144. Xu, X.; Zhou, C.; Wang, Z.; Du, X. Modeling the propagation of extremely low frequency electromagnetic emissions from the power lines to the inner magnetosphere in a dipole field. *J. Geophys. Res. Space Phys.* **2024**, *129*, e2023JA032403. https://doi.org/10.1029/2023JA032403.
145. Němec, F.; Santolik, O.; Hospodarsky, G.B.; Kurth, W.S.; Kletzing, C. Power Line Harmonic Radiation observed by the Van Allen Probes spacecraft. *J. Geophys. Res. Space Phys.* **2022**, *127*, e2022JA030320. https://doi.org/10.1029/2022JA030320.
146. Wu, J.; Zhang, C.; Zeng, L.; Ma, Q. Systematic investigation of power line harmonic radiation in near-Earth space above China based on observed satellite data. *J. Geophys. Res. Space Phys.* **2017**, *122*, 3448–3458. https://doi.org/10.1002/2016JA023131.
147. Xu, H.; Xu, W.; Ni, B.; Xiang, Z.; Gu, X.; Hosseini, P.; Zeren, Z.; Huang, J.; Yang, Y.; Liu, Y.; et al. Measurements and modeling of electron precipitation induced by the ionospheric heating experiment. *Space Weather* **2025**, *23*, e2024SW004035. https://doi.org/10.1029/2024SW004035.
148. Frolov, V.L.; Akchurin, A.D.; Bolotin, I.A.; Ryabov, A.O.; Berthelier, J.-J.; Parrot, M. Precipitation of Energetic Electrons from the Earth's Radiation Belt Stimulated by High-Power HF Radio Waves for Modification of the Midlatitude Ionosphere. *Radiophys. Quantum Electron.* **2020**, *62*, 571–590. https://doi.org/10.1007/s11141-020-10004-4.
149. Chernyshov, A.A.; Padokhin, A.M.; Grach, S.M.; Kogogin, D.A.; Shindin, A.V.; Pulinets, S.A.; Nasyrov, I.A.; Beletsky, A.B.; Tkachev, I.D.; Legostaeva, J.K.; et al. HF heating effects as seen from below and above: First results of joint SURA– Ionosfera-M experiment. *Geophys. Res. Lett.* **2026**, *53*, e2026GL123503. https://doi.org/10.1029/2026GL123503.
150. Li, W.; Ma, Q.; Kurth, W.S.; Hospodarsky, G.B.; Bolton, S.J. Global effects of chorus and hiss waves on trapped energetic electrons at Jupiter. *Geophys. Res. Lett.* **2026**, *53*, e2026GL122294. https://doi.org/10.1029/2026gl122294.
151. Wong, M.H.; Kolmašová, I.; Oyafuso, F.A.; Imai, M.; Mizumoto, S.; Levin, S.M.; Sankar, R.G.; Simon, A.A.; Brueshaber, S.; Orton, G.S.; et al. Radio pulse power distribution of lightning in Jupiter's 2021–2022 stealth superstorms. *AGU Adv.* **2026**, *7*, e2025AV002083. https://doi.org/10.1029/2025AV002083.
152. Long, M.; Roussos, E.; Ni, B.; Ma, Q.; Kollmann, P.; Zhou, R.; Clark, G.; Krupp, N.; Cao, X.; Lu, P.; et al. A slot region in the magnetosphere of Jupiter. *Nat. Commun.* **2025**, *16*, 7916. https://doi.org/10.1038/s41467-025-63186-8.
153. Blackledge, J. On the Chirp Function, the Chirplet Transform and the Optimal Communication of Information. *IAENG Int. J. Appl. Math.* **2020**, *50*, 285–319.
154. Rees, M.H. *Physics and Chemistry of the Upper Atmosphere*; Cambridge University Press: Cambridge, UK, 1989.
155. Sinnhuber, M.; Nieder, H.; Wieters, N. Energetic Particle Precipitation and the Chemistry of the Mesosphere/Lower Thermosphere. *Surv. Geophys.* **2012**, *33*, 1281–1334. https://doi.org/10.1007/s10712-012-9201-3.
156. Mironova, I.; Kovaltsov, G.; Mishev, A.; Artamonov, A. Ionization in the Earth's Atmosphere Due to Isotropic Energetic Electron Precipitation: Ion Production and Primary Electron Spectra. *Remote Sens.* **2021**, *13*, 4161. https://doi.org/10.3390/rs13204161.

157. Xu, W.; Marshall, R.A.; Fang, X.; Turunen, E.; Kero, A. On the effects of bremsstrahlung radiation during energetic electron precipitation. *Geophys. Res. Lett.* **2018**, *45*, 1167–1176. https://doi.org/10.1002/2017GL076510.
158. Xu, W.; Marshall, R.A.; Tyssøy, H.N.; Fang, X. A generalized method for calculating atmospheric ionization by energetic electron precipitation. *J. Geophys. Res. Space Phys.* **2020**, *125*, e2020JA028482. https://doi.org/10.1029/2020JA028482.
159. Sanchez, E.R.; Ma, Q.; Xu, W.; Marshall, R.A.; Bortnik, J.; Reyes, P.; Varney, R.; Kaeppler, S. A test of energetic particle precipitation models using simultaneous incoherent scatter radar and Van Allen Probes observations. *J. Geophys. Res. Space Phys.* **2022**, *127*, e2021JA030179. https://doi.org/10.1029/2021JA030179.
160. Pettit, J.; Elliott, S.; Randall, C.; Halford, A.; Jaynes, A.; Garcia-Sage, K. Investigation of the drivers and atmospheric impacts of energetic electron precipitation. *Front. Astron. Space Sci.* **2023**, *10*, 1162564. https://doi.org/10.3389/fspas.2023.1162564.
161. Salminen, A.; Asikainen, T.; Mursula, K. Satellite observations of the influence of energetic electron precipitation on the mesosphere and stratosphere in the northern hemisphere. *J. Geophys. Res. Atmos.* **2024**, *129*, e2023JD039581. https://doi.org/10.1029/2023JD039581.
162. Frolov, V.L.; Troitsky, A.V. HF-Induced Artificial Injection of Energetic Electrons from the Earth's Radiation Belt as a Powerful Source for Modification of Ionized and Neutral Components of the Earth's Atmosphere. *Atmosphere* **2023**, *14*, 843. https://doi.org/10.3390/atmos14050843.
163. Frolov, V.L.; Pershin, A.V.; Akchurin, A.D.; Zhang, X.; Vasil'ev, R.V.; Ermakov, V.Y. Results of Experimental Studies Conducted within the Framework of the SURA-CSES Program in 2018–2023. *Cosm. Res.* **2025**, *63*, 411–433. https://doi.org/10.1134/S0010952525601069.
164. Dong, X.; Zhao, S.; Liao, L.; Xu, W.; Lin, R.; Sun, X.; Huang, S.; Cui, Y.; Li, J.; Lu, H.; et al. Quantitative analysis of nighttime effects of radiation belt energetic electron precipitation on the D-region ionosphere during lower solar activity periods. *Atmos. Chem. Phys.* **2025**, *25*, 9183–9198. https://doi.org/10.5194/acp-25-9183-2025.
165. Rycroft, M.J. A Review of What Can Be Learnt from Tweeks and Related Topics. *Atmosphere* **2026**, *17*, 152. https://doi.org/10.3390/atmos17020152.
166. Katoh, Y.; Rosendahl, P.S.; Ogawa, Y.; Hiraki, Y.; Tadokoro, H. Effect of the mirror force on the collision rate due to energetic electron precipitation: Monte Carlo simulations. *Earth Planets Space* **2023**, *75*, 117. https://doi.org/10.1186/s40623-023-01871-y.
167. Clilverd, M.A.; Nunn, D.; Lev-Tov, S.J.; Inan, U.S.; Dowden, R.L.; Rodger, C.J.; Smith, A.J. Determining the size of lightning-induced electron precipitation patches. *J. Geophys. Res.* **2002**, *107*, 1168. https://doi.org/10.1029/2001JA000301.
168. Kolarski, A.; Srećković, V.A.; Mijić, Z.R.; Arnaut, F. Investigating Mid-Latitude Lower Ionospheric Responses to Energetic Electron Precipitation: A Case Study. *Data* **2025**, *10*, 121. https://doi.org/10.3390/data10080121.
169. Clilverd, M.A.; Rodger, C.J.; Gamble, R.; Meredith, N.P.; Parrot, M.; Berthelier, J.-J.; Thomson, N.R. Groundbased transmitter signals observed from space: Ducted or nonducted? *J. Geophys. Res.* **2008**, *113*, A04211. https://doi.org/10.1029/2007JA012602.
170. Hale, L.C. Lightning triggering and synchronization. *Nature* **1987**, *329*, 769.
171. Hale, L.C.; Baginski, M.E. Current to the ionosphere following a lightning stroke. *Nature* **1987**, *329*, 214–216.
172. Beggan, C.D.; Kloss, C.; Amblard, P.; Amezza, T.; Amit, H.; Aubert, J.; Baerenzung, J.; Lauridsen, J.B.; Brown, W.; Califf, S.; et al. International geomagnetic reference field: The fourteenth generation. *Earth Planets Space* **2026**, *78*, 127. https://doi.org/10.1186/s40623-025-02360-0.
173. Emmert, J.T.; Richmond, A.D.; Drob, D.P. A computationally compact representation of Magnetic-Apex and Quasi-Dipole coordinates with smooth base vectors. *J. Geophys. Res.* **2010**, *115*, A08322. https://doi.org/10.1029/2010JA015326.
174. McIlwain, C.E. Coordinates for mapping the distribution of magnetically trapped particles. *J. Geophys. Res.* **1961**, *66*, 3681–3691. https://doi.org/10.1029/JZ066i011p03681.
175. Ginet, G.P.; O'Brien, T.P.; Huston, S.L.; Johnston, W.R.; Guild, T.B.; Friedel, R.; Lindstrom, C.D.; Roth, C.J.; Whelan, P.; Quinn, R.A.; et al. AE9, AP9 and SPM: New models for specifying the trapped energetic particle and space plasma environment. *Space Sci. Rev.* **2013**, *179*, 579–615. https://doi.org/10.1007/s11214-013-9964-y.
176. Brown, W. Private communication, from British Geological Survey. 2 July 2026.
177. Roederer, J.G.; Lejosne, S. Coordinates for representing radiation belt particle flux. *J. Geophys. Res. Space Phys.* **2018**, *123*, 1381–1387. https://doi.org/10.1002/2017JA025053.

Disclaimer/Publisher's Note: The statements, opinions and data contained in all publications are solely those of the individual author(s) and contributor(s) and not of MDPI and/or the editor(s). MDPI and/or the editor(s) disclaim responsibility for any injury to people or property resulting from any ideas, methods, instructions or products referred to in the content.